Transport Phenomena in Vacuum Bag Only Prepreg Processing of Honeycomb Sandwich Panels

James Kratz

Department of Mechanical Engineering

McGill University

A thesis submitted to McGill University
in partial fulfillment of the requirements of the degree of
Doctor of Philosophy

Abstract

Honeycomb sandwich panels offer an extremely lightweight solution for aerospace structures. As efficiency demands increase, low-cost non-autoclave manufacturing solutions are sought for honeycomb and other composite structures. Vacuum-bag-only (VBO) manufacturing is one possible solution that relies on vacuum to remove all entrapped volatiles prior to cure, and then the differential pressure between the inside and outside of the vacuum bag consolidates the layers during cure. This technique can be very effective for monolithic laminates made with out-of-autoclave (OOA) prepregs, but honeycomb structures introduce two additional manufacturing nuisances. First, the core entraps up to 98 % of its volume during lay-up, and second, non-metallic cores readily absorb ambient moisture. Entrapped air and moisture can increase the honeycomb core pressure during processing, reducing part quality. Given that the honeycomb core pressure is crucial to achieving success in VBO manufacturing of honeycomb panels, a threefold approach was used in this thesis to study the transport phenomena that influence this behaviour.

First, the transport phenomena of the constituent materials were characterized. Applying an impermeable boundary condition to the tool-side skin allowed for simple air permeability characterization of honeycomb skins by considering only the bag-side skin. An instrumented test fixture was used to measure the honeycomb core pressure during the pre-processing vacuum hold. The results revealed that a transverse interconnected pore space was required in OOA prepreg skins for gas evacuation to proceed in honeycomb panels. The same test fixture was used to characterize the honeycomb skin air permeability and honeycomb core moisture diffusivity during elevated temperature processing. The evolving skin air permeability and core diffusivity were observed to cause the honeycomb core pressure to increase during the temperature ramp and decrease during the temperature hold.

Second, a process model was developed to predict honeycomb core pressure throughout the manufacturing process. The process model identified that

the honeycomb core pressure can exceed the vacuum bag consolidation pressure due to the high core moisture adsorption and elevated temperature diffusivity. Choosing, or creating, a honeycomb skin with high air permeability was identified as a key process parameter to avoid exceeding the consolidation pressure.

Finally, the material characterization and process modelling were successfully scaled to reproduce the honeycomb core pressure behaviour in holistic honeycomb panels. The *in-situ* honeycomb core pressure was measured throughout the manufacturing process in dual-skin honeycomb panels using embedded pressure sensors. The embedded pressure sensor response validated the material characterization assumptions and model simplifications used to predict the honeycomb core pressure during the VBO manufacturing process.

Manufacturing honeycomb panels is a complex activity with many material and processing variables. A suitable skin material and bagging configuration was selected for VBO manufacturing of honeycomb panels by coupling transport phenomena modelling and tailored material characterization. This approach could be used to reduce manufacturing trial and error before scaling these materials to larger applications.

Sommaire

Les panneaux sandwich en nid d'abeille offrent une solution extrêmement légère pour les structures aérospatiales. Avec l'augmentation de la demande pour les structures en matériaux composites, les solutions de fabrication de ces structures hors de l'autoclave sont recherchées afin de réduire les coûts. La méthode de fabrication avec sac sous vide requiert une pompe à vide pour enlever tous les gaz piégés après le drapage des matériaux préimprégnés et créer le différentiel de pression entre l'intérieur et l'extérieur du sac à vide afin de consolider les couches de composite. Cette technique peut être très efficace pour les laminés monolithiques, mais les structures en nid d'abeille présentent deux difficultés supplémentaires lorsque des nids d'abeilles non métalliques sont utilisés. D'abord, le nid d'abeille contient 98% du volume d'air piégé pendant le drapage, et deuxièmement, les nids d'abeilles non métalliques absorbent l'humidité pendant leur manipulation. L'air emprisonné dans le nid d'abeilles et l'humidité va augmenter la pression pendant la mise en forme, et peuvent créer des défauts.

Cette thèse est divisée en trois thèmes pour étudier et pour optimiser le processus de fabrication des panneaux de composite sandwich avec nid d'abeilles. Tout d'abord, une condition imperméable a été appliquée sur le côté de l'outil, ce qui permet une caractérisation simple des matériaux utilisés pour la mise en forme combinés avec les matériaux préimprégnés de côté de sac à vide. La perméabilité à l'air pour les matériaux préimprégnés a été mesurée durant l'évacuation de l'air avant la cuisson, révélant un degré significatif de l'anisotropie de perméabilité à l'air. Pendant la cuisson à température élevée, la perméabilité à l'air a évolué avec le cycle de cuisson. En outre, le coefficient de diffusion de l'humidité du nid d'abeille non métallique a été caractérisé par une fonction de la concentration d'humidité et de la température. Deuxièmement, un modèle a été développé pour prédire la pression dans le nid d'abeille pendant le processus de fabrication. Des cartes de processus ont été créées afin d'identifier les combinaisons de conditions de traitement pouvant augmenter la pression dans le nid d'abeille au-dessus de la pression de consolidation. Finalement, des panneaux ont été fabriqués avec un

laminé sur le côté de l’outil ainsi que sur le côté du sac à vide. Des capteurs de pression ont été incorporés pour mesurer la pression dans le nid d'abeilles pendant le processus de fabrication.

La caractérisation des matériaux et la modélisation des processus développées à partir d'expériences simples à petite échelle ont permis de reproduire avec succès le comportement complexe de la pression dans le nid d'abeilles des pièces de grandes dimensions.

Table of Contents

List of Tables

List of Figures

Nomenclature

Latin symbols

A	Area [m^2]
$A_{Dry\ Tow}$	Visible dry tow area [m^2]
b	Klinkenberg factor [–]
c	Concentration [kg/m^3]
d	Diffusion length [m]
D	Diffusivity [m^2/s]
D_o	Arrhenius diffusion pre-exponential factor [m^2/s]
E	FLUENT energy [J]
E_d	Diffusion activation energy [kJ/kg]
H	Relative humidity
h	Thickness [m]
J	Diffusive flux [kg/(m$^2 \cdot$ s)]
K	Permeability [m^2]
K^*	Effective permeability [m^2]
L	Length [m]
M	Moisture content [%]
M_U	Moisture content at 100 % relative humidity [%]
m	Mass [kg]
$\dot{m}$ and dm/dt	Mass flow rate [kg/s]
P	Pressure [Pa]
P_{Bag}	Vacuum bag pressure [Pa]
P_{Core}	Honeycomb core pressure [Pa]

P_{op}	FLUENT operating pressure [Pa]
Q	Volumetric flow rate [m^3/s]
Re	Reynolds number [–]
R_u	Ideal gas law constant [m^2/(s^2 · K)]
T	Temperature [K]
t	Time [s]
V_{Core}	Honeycomb core volume [m^3]
x	Position [m]

Greek symbols

γ	Mass fraction of substances in honeycomb core
λ	Thermal conductivity [J/(s · m · K)]
μ	Viscosity [Pa·s]
v	Velocity [m/s]
ξ	Constant [–]
Ω	Flow aspect ratio [–]
ω	Molar mass [–]
ρ	Density [kg/m^3]

Acknowledgements

I am grateful to my research supervisor, Prof. Pascal Hubert, for all the years of support, guidance, and continually providing extraordinary opportunities for his students grow as young researchers.

This work was carried out as part of a Consortium de recherche et d'innovation en aérospatiale au Québec (CRIAQ) academic–industry collaborative research project (COMP–1). This work would not have been possible without the financial support from CRIAQ and the Natural Sciences and Engineering Research Council of Canada (NSERC). Our industry and research centre partners, Bell Helicopter Textron Canada, Bombardier Aerospace, Delastek, the National Research Council Canada Institute for Aerospace Research, and le Centre de développement des composites du Québec (CDCQ) provided financial support, materials, and access to equipment that helped further this work. I would like to thank all industry partners for the input that helped me consider the practical significance for this technology.

Many thanks go to Timotei Centea for the years of close collaboration, many long discussions about out-of-autoclave processing science, and for generously offering his micro-CT expertise to scan the samples in this thesis. I would like to thank Dominic Leblanc and Steven Payette for their help with the air permeability measurements, Dr. Arthur Levy and Dr. Meysam Rahmat for insightful modelling discussions, and Adam Smith for expertly soldering many tiny wires to the miniature pressure sensors. I would like to thank Convergent Manufacturing Technologies for granting special permission to use their patented miniature pressure sensor technology in this work. In particular, I would like to thank Malcolm Lane at Convergent for his support implementing this technology.

I appreciate all the friendships built with members of the Structures and Composite Materials Laboratory during my time at McGill. This is truly a wonderful research group, and it starts with the people.

And last but not least, I would like to thank my family for all their support through my graduate studies.

Chapter 1

Introduction

Thermoset prepregs offer a consistent, predictable manufacturing method for flight-critical composite structures. The optimal resin content is pre-impregnated into the fibre reinforcement, resulting in a cured composite part with a 60 % fibre volume fraction, a 40 % resin volume fraction, and ideally, no voids.

Prepreg processing is commonly carried-out by vacuum bag moulding, where the pressure difference inside a vacuum bag and the external pressure outside the bag consolidate the composite layers against a mould. Most airworthy composite structures are manufactured in an autoclave, where 500–700 kPa of external pressure is applied to a vented vacuum bag [1]. Even with these high pressures, voids can arise in autoclave cured composites if entrapped air is not removed prior to elevated temperature curing [2].

The conventional method to remove entrapped air is through debulking—applying vacuum for between 5 and 15 minutes after new plies are added to the layup [1]. Regrettably, debulking is expensive and time consuming, since it requires additional bagging materials and labour. To alleviate the need for debulking, partially impregnated prepregs were developed to allow air entrapped during the lay-up process to escape the prepreg through porous networks when vacuum is applied prior to cure [3]. Using partially impregnated materials, a void free 100-ply laminate was autoclave cured without debulking [3]. In this case, the porous network created by partial resin impregnation was responsible for evacuating entrapped gasses, and reducing the void content in the cured panel.

This breakthrough in impregnation technology motivated the development of out-of-autoclave prepregs that can be cured with only vacuum bag pressure.

1.1 Out-of-autoclave prepregs

Out-of-autoclave (OOA) prepregs are partially impregnated and are oven cured under vacuum bag only (VBO) pressure. The external pressure is provided by the pressure differential created between the pressure under a vacuum bag and atmospheric conditions. The vacuum bag can produce low void content composite laminates because of controlled resin impregnation techniques, and resins that have a high thermal stability—the resins do not release volatiles that can nucleate voids during cure. OOA prepregs feature dry tow regions, as shown in Figure 1.1, created by applying the resin to the outer surfaces of the prepreg [4-5]. As a result, the vacuum bag can accomplish two tasks: first, remove entrapped air within the uncured laminate stack, and second, provide enough consolidation pressure for the resin to flow into the dry regions during elevated temperature processing.

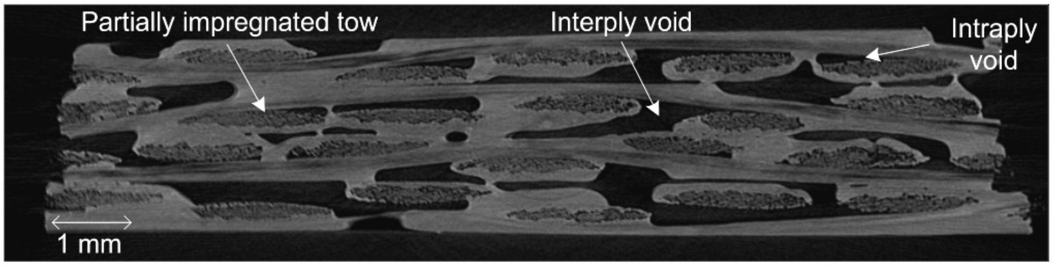

Figure 1.1. Micrograph of a 5 harness satin out-of-autoclave prepreg immediately after hand lay-up. The resin (light grey regions) surround the partially impregnated tows (dark grey regions), creating micro-porosity within the tows, but also macro-porosity through interply and intraply voids (black regions). Image from Ref. [43].

OOA prepregs are attractive for large, integrated structures because they offer the freedom to manufacture parts larger than pre-existing autoclaves. Furthermore, OOA prepregs offer familiar handling and lay-up techniques to those of traditional autoclave prepregs. Curing OOA prepregs with only vacuum bag pressure can achieve laminates with less than 1 % porosity [4-7]. Unfortunately, large structures are usually stiffened with honeycomb inserts, which are more difficult to process to the same quality. Studies on out-of-autoclave honeycomb panels have reported higher levels of porosity in the cured composite skins [8-12].

1.2 Honeycomb structures

Honeycomb sandwich panels offer an extremely high stiffness and strength-to-weight ratios [1]. As a result, honeycomb usage is very desirable for aerospace applications. Two composite skins are bonded to an embedded honeycomb core, as shown in Figure 1.2. An adhesive layer is needed to bond the core to OOA prepreg honeycomb skins if the prepreg does not have a sufficient resin content to bond the skin and impregnate the dry tows.

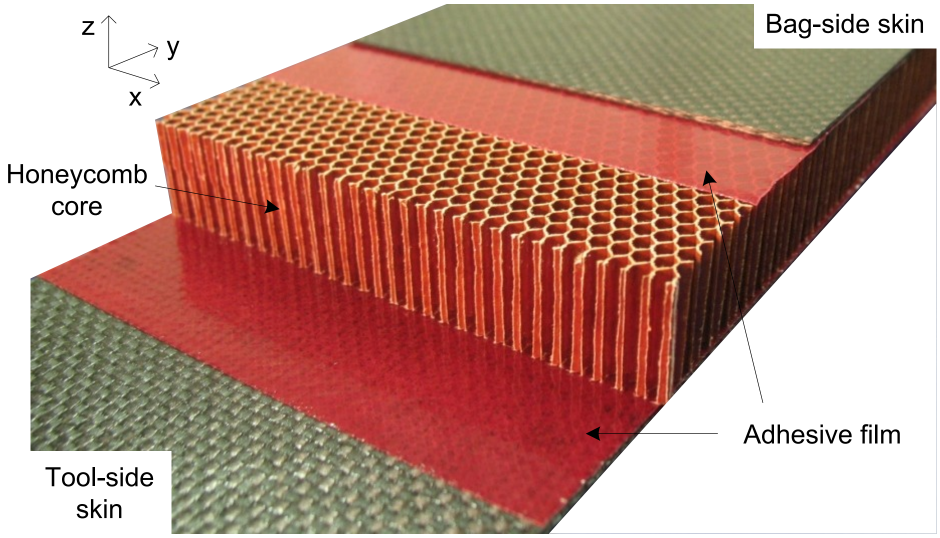

Figure 1.2. Honeycomb sandwich panel before cure. Thin prepreg skins are cured and bonded to the thick core using an adhesive film.

The honeycomb core introduces an additional pressure variable into the vacuum bag assembly. The honeycomb core pressure needs to be considered in addition to the vacuum bag pressure, and the ambient pressure. The differential pressure between the inside of the honeycomb core and the vacuum bag may lead to core crush or migration, blown cells, and skin pillowing or dimpling if the autoclave pressure is high [1]. These problems are usually overcome by reducing the autoclave pressure to between 280 and 350 kPa [1], but this can lead to inferior bonding between the skin and core, including disbonds, and high skin porosity levels.

The reduced consolidation pressure in VBO processing is beneficial to reducing high-pressure defects, primarily core crush [10]. However, the main manufacturing concern is the large volume of air entrapped within the honeycomb core during lay-up that could be a source for voids during cure. The difference in gas entrapment between laminates and honeycomb panels is shown in Figure 1.3. Monolithic laminates entrap minor volumes of air in-between layers (Figure 1.3b) when compared to the volume of air entrapped in-between honeycomb skins (Figure 1.3c). If the honeycomb core pressure approaches the ambient pressure during cure, higher skin porosity [12] and lower skin-to-core adhesion can occur in the cured panel [12,13].

If all entrapped gasses are removed from the core prior to cure, void sources during cure will be reduced, increasing the likelihood that honeycomb skin porosity will approach the levels observed in monolithic laminates. Additional void sources include volatiles or moisture, which could be introduced into the resin during the prepregging process, or during storage and handling. Fortunately, out-of-autoclave prepregs are manufactured using a hot melt impregnation process, where moisture is the most predominant volatile [1], and *Grunenfelder and Nutt* [7] have shown that the effects of ambient moisture can be eliminated as a major void source in monolithic laminates. Additionally, newer adhesive systems (including the one chosen in this study) have been formulated to resist absorbing ambient moisture [14].

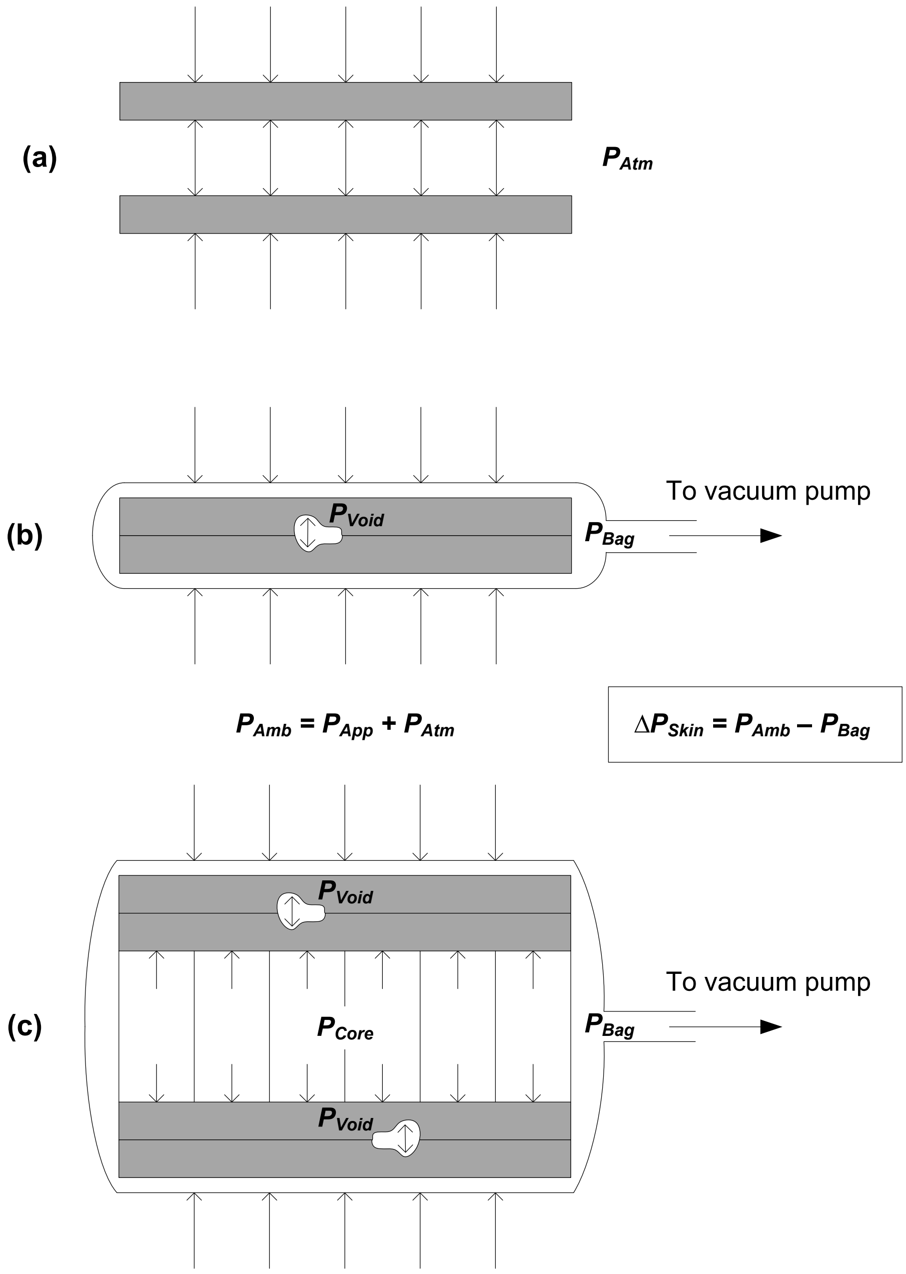

Figure 1.3. Pressure differential in monolithic laminates and honeycomb panels: (a) atmospheric pressure around two prepreg layers before application of vacuum, (b) pressure around two layers after a vacuum bag is applied, including possible void pressure, P_{Void}, between plies, and (c) pressure around two prepreg skins and an embedded honeycomb core that has retained pressure, P_{Core}, in the cells. The skin consolidation pressure, ΔP_{Skin}, could be supplied by an autoclave, press, or vacuum bag. Adapted from Ref. [11].

The first priority towards achieving low void content VBO honeycomb panels is evacuation of entrapped air from the core prior to cure. Air evacuation will depend on the prepreg pore space that is available for air evacuation, as defined by the skin materials (prepreg and adhesive film), lay-up, and bagging configuration. Two evacuation paths are possible to remove entrapped air from the core: transverse and in-plane, as shown in Figure 1.4. The transverse path requires a perforated release film placed above the sandwich assembly, followed by breather cloth and a vacuum bag. This bagging arrangement provides a direct path between the vacuum pump and the top prepreg layer—through the perforations in the release film. As a result, entrapped air can escape the core through the bag-side skin. For materials with low transverse air permeability, spiking could be considered to enhance the air permeability and decrease air evacuation times [15].

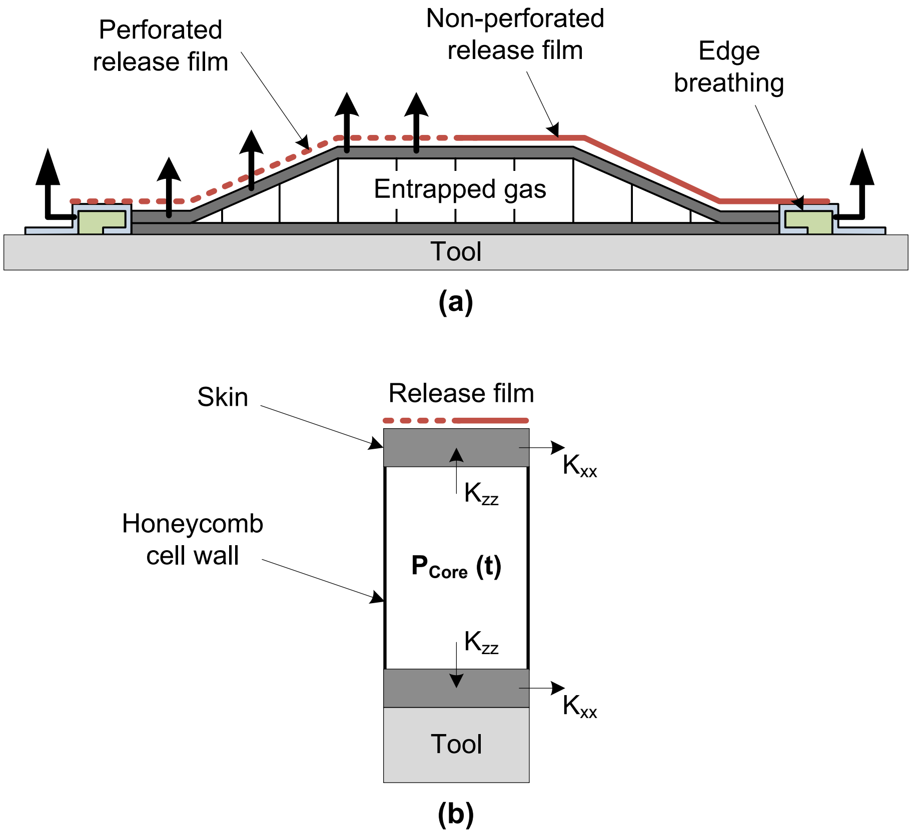

Figure 1.4. Schematic of the breathing strategies available to evacuate entrapped gas from out-of-autoclave honeycomb structures: (a) Transverse evacuation requires a perforated release film and in-plane evacuation requires edge breathing, and (b) a close-up of a honeycomb cell showing that gas must first flow in the transverse direction of the skin before in-plane or transverse evacuation can continue. The skin air permeability, K, will govern the rate of air evacuation from the core.

A drawback of transverse air flow is that resin can also flow in the transverse direction. Currently, prepregs have between 32 and 35 % resin content by weight, and require little or no bleeding [1]. Overbleeding net resin content prepregs can cause resin starved areas, and lead to void formation [1]. To prevent resin loss, a non-perforated release film should be placed above the skin, this however, will limit air evacuation to the in-plane direction. In-plane air evacuation can be used by placing edge breathing around the perimeter of the panel. Common edge breathing materials include glass tows [6] or fibreglass cloth wrapped around a dam, such as cork or sealant tape [5]. With edge breathing in place, entrapped air can escape the honeycomb core through both the bag-side and tool-side skins, and be extracted around the perimeter. An appropriate breathing strategy must be considered given the skin material's air evacuation capacity, panel size, and manufacturing conditions.

A 3-D flow problem can arise for air flow in honeycomb skins because of the anisotropy present in the prepreg air permeability tensor. If the air permeability of a skin is isotropic in-plane, $K_{xx} = K_{yy}$, the flow problem can be studied in 2-D, governed by the in-plane, K_{xx}, and transverse, K_{zz}, air permeabilities. A direct 1-D measurement of K_{zz} is possible for honeycomb skins, but K_{xx} is more challenging because entrapped air must first flow through the adhesive and into the prepreg dry fibre regions before the air can flow in-plane. To determine if a 1-D flow regime exists, a simulation of the pressure profile within the permeability test skin could be performed using a computational fluid dynamics (CFD) software program capable of solving porous media problems. *Loos et al.* [16] have used the FLUENT CFD code to model the filling time in resin infusion processes, and could be used to identify the ratio of effective 1-D flow area to the bulk area of orthotropic honeycomb skins.

1.2.1 Moisture desorbed from non-metallic cores

Even if all entrapped gasses are removed during the vacuum hold prior to cure, an increase in honeycomb core pressure is possible during cure because non-metallic cores release absorbed moisture at elevated temperatures. Aluminum cores absorb less moisture from the atmosphere, but due to in-service corrosion problems, non-metallic cores are preferred in aircraft [1].

Aramid based Nomex® paper quickly absorbs moisture within the first 24 to 48 hours of exposure to moist air, and after 1 week in very humid environments, it can absorb up to 10 % moisture content by weight [17]. The influence of temperature on the pressure of moist air in a void space, such as honeycomb cells, is illustrated in Figure 1.5. Each pressure curve in Figure 1.5 represents the pressure increase for a constant humidity level in the core. Given that OOA prepregs are typically cured between 93 and 121 °C [18], the pressure within the honeycomb cells can exceed the applied consolidation pressure for high levels of relative humidity within the cell space. Autoclave processing can easily suppress any moisture level at the upper 121 °C VBO process temperature—even if the core is fully saturated with moisture. As the relative humidity increases to the upper cure temperature of 177 °C for epoxy prepregs, humidity induced pressure may exceed the upper consolidation pressure provided during autoclave curing.

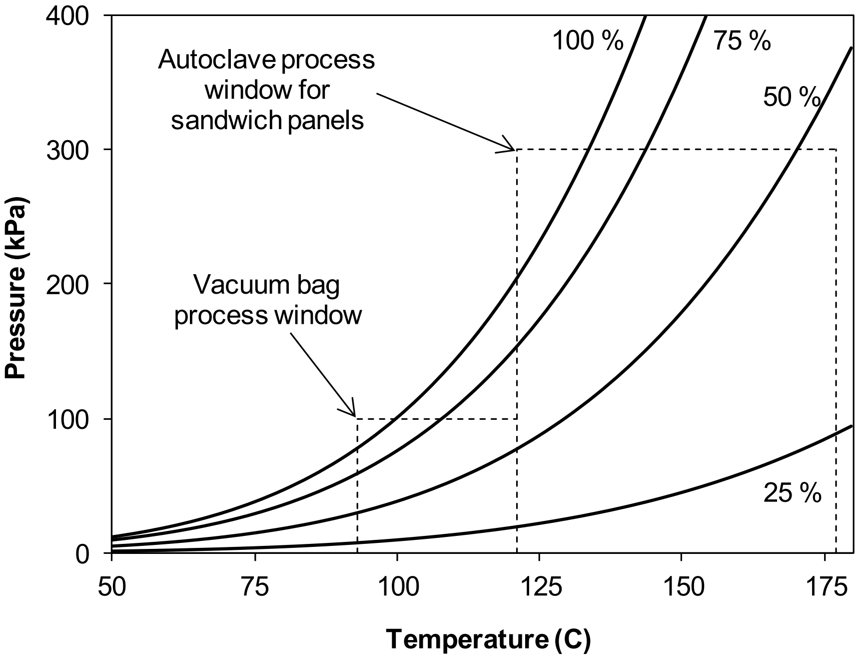

Figure 1.5. Isochoric pressure evolution of moist air at constant relative humidity levels.

The pressure curves shown in Figure 1.5 are for a closed system, which is not the case for VBO processing. The honeycomb core pressure will be influenced by moisture diffusion out of the core and gas leaking through the honeycomb skins. During cure, the resin viscosity decreases before gelation, simultaneously increasing resin mobility and reducing the pore space within the skin. As a result, the air permeability will change during cure [15,19]. The corresponding change in air permeability will affect the honeycomb core pressure evolution during cure, causing the pressure to fall below the pressure predictions in Figure 1.5.

Clearly, measuring the honeycomb core pressure in between two honeycomb skins presents some unique challenges. In light of this, most studies measuring honeycomb core pressure during cure have chosen to measure the honeycomb core pressure in a cavity [12,13,15,19– 21], where the honeycomb core resides, and co-curing a bag-side skin to the core. Measuring the honeycomb core pressure in a panel featuring both bag-side and tool-side skins will require embedding a pressure measurement device within the honeycomb core. Introducing sensors without altering the panel properties, disturbing the pressure behaviour, or creating leaks within the parent structure may present intricate challenges. However, a miniature, robust solution would be helpful to validate the process models as long as the sensors do not disturb the process phenomenon within the host structure.

1.3 Research objectives

Most major honeycomb sandwich panel process-induced defects are related to the honeycomb core pressure during cure. Inadequate core pressure is likely to produce panel defects, such as core crush, blown cells, skin dimpling, and skin pillowing. Excessive core pressure can lead to voids, and disbonds. An ideal core pressure range will likely exist for each specific material and manufacturing condition. As a result, most fabrication techniques are developed at great expense by trial and error because no process models for core pressure currently exist for honeycomb panel fabrication.

The main goal of this thesis is to demonstrate how tailored material characterization, focused process modelling, and representative experiments can be used to optimize VBO manufacturing of honeycomb structures. The specific research objectives are as follows:

1. Characterize the air permeability of different OOA prepreg materials during the vacuum hold prior to cure for different skin thickness and breathing direction,
2. Select a suitable OOA prepreg material and breathing configuration for honeycomb panels and characterize the air permeability during cure,
3. Develop a process model to predict honeycomb core pressure during cure for non-metallic core by including moisture diffusion, and
4. Validate the material characterization and process modelling approach by manufacturing instrumented honeycomb panels.

1.3.1 Thesis outline

The work presented in this thesis is organized as shown in Figure 1.6 as follows:

- Chapter 2 reviews the scientific literature, covering both experimental and modelling studies of honeycomb structures
- Chapter 3 presents the experimental set-up used to characterize the honeycomb skin air permeability coefficient and the honeycomb core moisture diffusion coefficient. The governing equation to calculate the air permeability is derived for the experimental set-up. The computational fluid dynamics software FLUENT was used to analyze the flow regime within the honeycomb skins to identify the flow regime in the air permeability experiments.
- Chapter 4 presents the pre-processing vacuum hold and elevated temperature processing air permeability characterization, and correlates the results to the micro-CT images of skin microstructure. The preferred skin material and breathing direction is selected for VBO manufacturing.
- Chapter 5 presents the model development for honeycomb core pressure during elevated temperature processing. A case study, using a bag-side

honeycomb skin configuration, was applied to compare the model with experiments.

- Chapter 6 scales the model to a representative honeycomb structure. Embedded pressure sensors were used to validate the process model for honeycomb structures.
- Chapter 7 draws conclusions from this work, identifies the original contributions, and discusses the future outlook for research in VBO honeycomb structures.

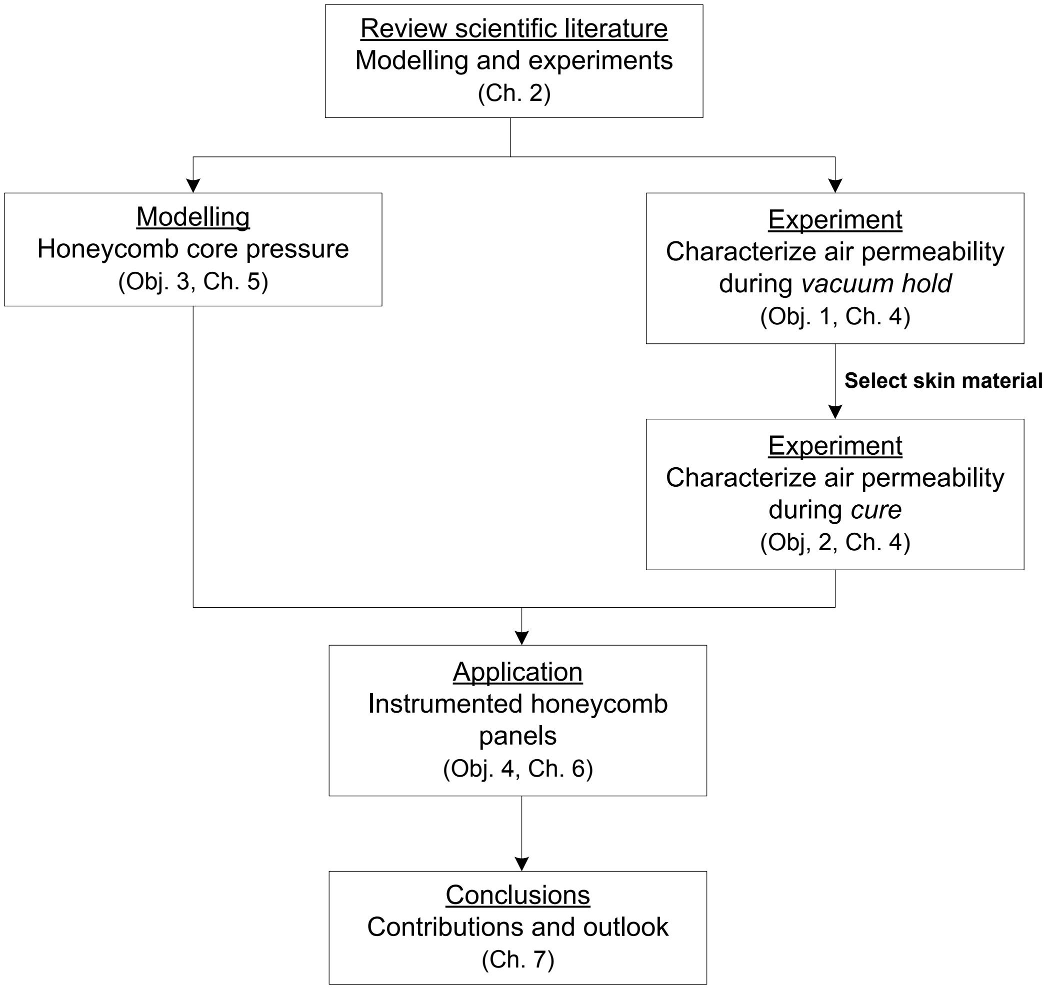

Figure 1.6. Flowchart of thesis organization with objectives.

Chapter 2

Review of Scientific Literature

Manufacturing honeycomb sandwich panels is a complex activity, influenced by many material and processing factors, including reinforcement (raw material, fabric style, weave pattern, and fibre sizing), prepreg (resin type, content, and impregnation), adhesive film (flow behaviour, carrier, and areal density), consumable materials (release film perforations, and breather density), and part manufacturing (layup, bagging arrangement, vacuum level, ambient pressure, and curing cycle). Researchers have investigated the effect of material and process parameters on the quality of lab-scale honeycomb panels using experiments, material characterization, and process modelling. Both approaches aim to identify the best manufacturing method available for the given materials and process parameters, however, they are difficult to relate.

This chapter begins by first reviewing the pertinent scientific literature for flow through porous media, and how it can be applied to characterize honeycomb skins and develop models for the honeycomb core pressure during processing. The second part of this chapter reviews experimental studies to identify what processing parameters have been considered to influence the quality of honeycomb panels during fabrication.

2.1 Flow through porous media

The material property that describes fluid flow through a porous medium is permeability [22-23]. The intrinsic permeability of a material is determined solely by the solid matrix, and is independent of both fluid properties and flow mechanisms [23]. In liquid composite moulding, the porous medium's flow characteristics are captured by using spatially averaged variables over a representative volume to model the motion of liquid resin flow through a fibre network [24]. The model requires permeability to predict processing parameters, such as filling time and resin pressure [25]. The coefficient of permeability is usually determined experimentally using the idealization shown in Figure 2.1a, and the relationship describing the volumetric flow rate, Q, is commonly expressed by Darcy's law:

$$Q = -\frac{KA}{\mu}\frac{dP}{dx} \tag{2.1}$$

where K is the permeability scalar in the flow direction, A is the cross-sectional area of the sample, dP/dx is the pressure gradient at position x, and μ is the fluid viscosity. Permeability physically represents the averaged cross-sectional area of the porous medium allowing fluid flow, and therefore has units of Length^2 [24].

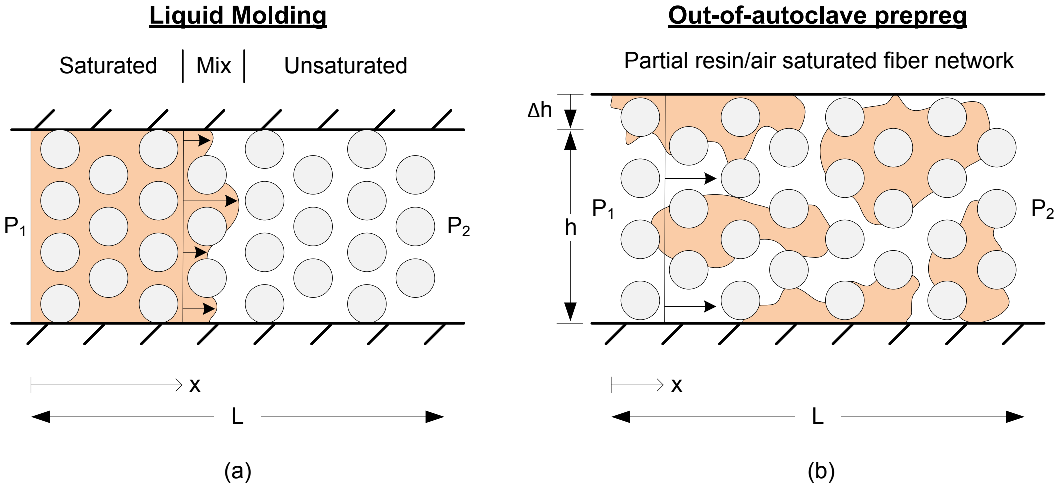

Figure 2.1. Microscopic idealization of flow through porous media: (a) incompressible resin flows through the void space and around the solid fibres within the rigid porous medium, and (b) compressible air flows through the consolidating void space and around the resin and solid fibre network within the porous medium.

Composite materials are usually considered anisotropic, where the full material permeability is describe by the tensor

$$\overline{\overline{K}} = \begin{bmatrix} K_{xx} & K_{xy} & K_{xz} \\ K_{yx} & K_{yy} & K_{yz} \\ K_{zx} & K_{zy} & K_{zz} \end{bmatrix}.$$

The permeability tensor for anisotropic fabrics can be calculated by the straight line passing through the plot of flow rate versus pressure drop for experiments performed in each principal flow direction [23]. Experimental error in these measurements is common because Darcy's law describes the macroscopic relationship between flow and pressure, and does not contain terms to describe the effects of porosity, tortuosity, or capillary effects [24]. The choice of test fluid can cause variation in measurements for the same fibre perform, tested in the same lab, direction, and fibre volume fraction [26]; the fibre sizing has been known to change the measured permeability value for different liquids [25]. Even with the same test fluid, variations in permeability are observed in woven fibrous materials because of pore size differences between the individual tows and within tow fibre bundles [27].

2.1.1 Flow of gasses in porous media

Gas flow can be used to characterize the fibre-bed permeability in-order to improve experimental cleanliness and reduce fibre rearrangement, wash-out, or swelling that occurs with liquid permeability experiments [23]. Gas compressibility causes the flow volume and velocity through the sample to change from the pressure inlet through the outlet, resulting in a non-linear differential equation to describe gas flow. If the gas behaves as an ideal gas, the flow rate can be described by Darcy's law at constant temperature [23]:

$$Q = -\frac{KA}{2L\mu}\frac{P_2^2 - P_1^2}{P_2}, \tag{2.2}$$

where P_2 is the outlet pressure, P_1 the inlet pressure, and L is the length of the sample, as shown in Figure 2.1.

Gas flow experiments with either low gas pressure or low permeability media can overestimate flow velocity because of the slip phenomenon—known as the Klinkenberg effect [28]. Darcy's law is based on laminar flow theory, which assumes zero fluid velocity at the interface between the gas molecules and the solid fibres [22]. In reality, fluid velocity at the gas/solid interface is not necessarily zero [22].

The Klinkenberg expression relates the gas permeability at a given pressure, K_g, to the intrinsic or liquid permeability, K_l, for the same porous medium [22-23, 28]:

$$K_g = K_l\left(1+\frac{b}{P}\right), \tag{2.3}$$

where P is the pressure at which K_g is measured, and b is a constant—known as the Klinkenberg factor—that is characteristic for both the gas and the porous medium.

Slip flow is more pronounced in fine-grained materials, such as sand, where the mean free path of the gas molecules approaches the pore dimensions. *Miguel and Serrenho* [29] demonstrated that free molecular flow becomes an important contribution to estimate the permeability of sand with 10 μm pores [29]. Since the pores in carbon fibres prepregs are on the same order of magnitude, free molecular flow is likely to occur at the pressures encountered in VBO processing.

Studies measuring both gas and liquid permeability of woven fibrous materials have validated Darcy's law for permeability measurements near atmospheric pressure, without having to compensate for Klinkenberg effects [30-34]. As the gas pressure, P, decreases towards vacuum in Eq. (2.3), the Klinkenberg effect will likely increase the difference between gas and liquid permeability. Klinkenberg effects can be neglected if the intrinsic permeability of the fabric is not needed, or corrections factors can be applied to estimate the intrinsic permeability from gas flow measurements [28].

Gas flow measurements have been used to measure the in-plane [35-39] and transverse [37-39] air permeability of prepregs. These studies report air permeability values by assuming that air is the only permeating fluid, otherwise a multi-phase flow exists. OOA prepregs have three distinct phases: solid fibrous network, high viscosity resin, and compressible air. The resin and gas partially saturate the fibre network, leaving a pore space, shown schematically in Figure

2.1b. If the pores are interconnected, gas transport can occur through the pore space from one end of the sample to the other [22]. If the pores are isolated, they cannot contribute to gas transport across the sample [23], and should be considered part of the solid matrix [22]. If air is assumed to flow around the resin, then the resin can be considered part of the solid matrix, and the coefficient of permeability to air can be measured. These measurements do not represent the intrinsic permeability of the woven fabric, but rather estimate the gas flow capacity of OOA multi-phase prepreg materials. The air permeability can then be used to predict vacuum hold times to evacuate air from the prepreg lay-up in the same way that liquid permeability is used to estimate flow front position in liquid composite molding.

2.1.2 Measurement of prepreg air permeability

The main differences between conventional permeability measurements for liquid molding applications and air permeability measurements of OOA prepregs was highlighted in Figure 2.1. Whereas resin is introduced into a rigid cavity at constant thickness for liquid permeability measurements, OOA prepregs have the optimal resin content pre-impregnated into the fabric before the air permeability measurement. Air permeability measurements are performed under vacuum pressure to simulate vacuum bag processing, and as a consequence, sample thickness may change because resin may flow into the pore space.

The prepreg resin viscosity has been tailored by the manufacturer to allow the prepreg plies to stick together during lay-up and minimize resin cold-flow during the vacuum hold prior to cure. This prevents the porous regions within the prepreg from becoming blocked. When the composite is cured at elevated temperature, the resin viscosity decreases in-order to fully-saturate the dry fibre regions [41], and cure the resin [42]. During cure, changes in sample air permeability are expected as the resin infiltrates the pore space, consolidating the prepreg layers [15,19].

Micro-CT has been used to gain insight into the micro-structural details of OOA prepregs [43], and could identify how the pore spaces in OOA prepregs become blocked or constricted when vacuum pressure is applied during the pre-processing vacuum hold and elevated temperature cure. A reduction in pore space is usually associated with a reduction in thickness, and slight thickness changes can cause significant error in permeability measurements [44]. Thickness changes are possible during OOA prepreg air permeability measurements, and need to be accounted for during testing.

Arafath et al. [37] and *Xin et al.* [38] showed the disparity between in-plane and transverse air permeability was two orders of magnitude for the same prepreg system. Furthermore, *Louis et al.* [39] reported an in-plane air permeability coefficient of 4.3 x 10^{-14} m^2 for 5 harness satin prepregs, but were unable to detect any transverse air permeability for more than two layers. Low transverse air permeability may lead to voids in monolithic laminates if entrapped air cannot be evacuated from between plies. However, these defects may be magnified in honeycomb panels because the volume of gas entrapped between honeycomb skins is much higher.

2.1.3 Falling pressure air permeability measurements

Pressure and time are easier to measure than low flow rates or velocities [45]. Adding reservoirs of calibrated volumes and measuring the time for the pressure in each volume to equilibrate may be more suitable for low permeability materials. The falling pressure (or pulse decay) method proposed by *Brace et al.* [45], relies on pseudo-steady state flow conditions arising in the test sample as the pressure between the two sides decreases. The falling pressure measurement technique has been broadly applied to measure the permeability of low permeability cores in soil sciences [45-52]. The consensus from these studies was that the initial condition for the experiments was to begin with constant pressure on either side of the test sample. The pressure in one reservoir would remain constant while the pressure in the other reservoir changed. The pressure was measured in both reservoirs, as shown in Figure 2.2, and the flow rate was calculated from the known volume in each reservoir, fluid compressibility, and rate of pressure change.

The falling pressure technique is well suited for vacuum bag molding processes, where prepregs have lower air permeability coefficients, and a pressure differential is usually applied during the manufacturing process. As a result, this approach has been used to measure the transverse air permeability of prepregs [19,53,40] and honeycomb skins [15, 20-21].

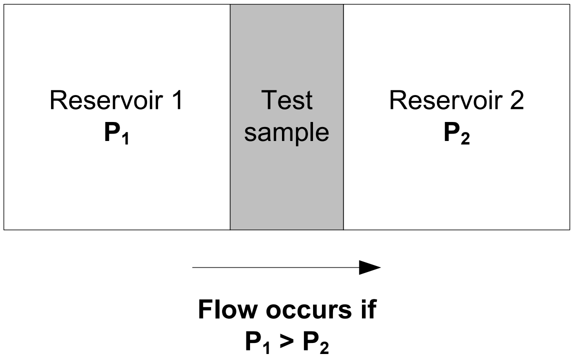

Figure 2.2. Schematic of falling pressure experimental set-up.

2.1.4 Air permeability of honeycomb skins

The steady-state and falling pressure air permeability measurement techniques can be applied to honeycomb skins if interconnected pores form several continuous paths from one side to the other. An idealized schematic of the pore space of a honeycomb skin is presented in Figure 2.3a. Honeycomb skins differ from laminates because they require an adhesive layer to help bond the prepreg to the core during cure. Unfortunately, the adhesive can act as a barrier to gas flow [15].

The transverse air permeability of unidirectional honeycomb skins has been thoroughly investigated by *Tavares et al.* [13,15,19–21]. They identified that unidirectional prepregs have very low air permeability (order of 10^{-20} m^2) in their as-received condition [19]. The air permeability of the material can be increased by introducing perforations into the adhesive film, individual prepreg plies, or entire honeycomb skins [15]. Alternatively, the air permeability was increased by increasing the dry fibre area (pore space) within the honeycomb skin by incorporating semi-prepregs, where the resin was applied in strips [21]. Semi-prepregs complicate the fibre infiltration process since the resin flow length increases from 0.1 to 5 mm. Resin-pooling and dry spots were observed in honeycomb panels [21]. Collectively, this body of work demonstrated the options available to measure honeycomb skin air permeability, and subsequently improve the air permeability of honeycomb skins.

The evolution of skin pore space during cure is represented in Figure 2.3b. As the resin infiltrates the pore space, the air permeability has been observed to decrease [15,19], and as a result, the honeycomb core pressure may increase during cure. When the honeycomb core pressure approaches the consolidation pressure during cure, higher skin porosity [12] and lower skin-to-core adhesion have been observed in cured panels [12,13]. Ideally, a cured honeycomb panel has a fully saturated fibre network, free of voids, with smooth fillets formed at the skin-to-core interface.

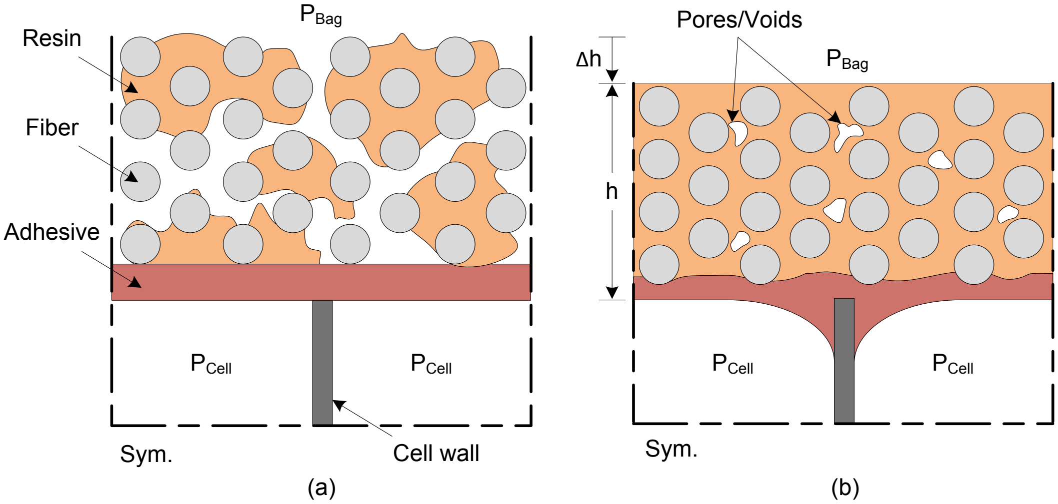

Figure 2.3. Illustration of the phases present in an out-of-autoclave honeycomb skin: (a) before cure, and (b) during cure. The air permeability through the skin is expected to change during processing as the resin and adhesive fill the narrow openings within the pore space, consolidating the fibre network while decreasing the skin thickness.

2.1.5 Diffusion of gasses through honeycomb skins

Transport of entrapped gasses (air, water vapour, or other volatiles released by the polymer resins) through the honeycomb skin can also occur through diffusion

[22]. Diffusion transport is governed by Fick's law, which estimates the diffusion time, t_d, as:

$$t_d = \frac{d^2}{4D} \tag{2.4}$$

where d is the diffusion length and D is the diffusion coefficient.

Diffusion coefficients in composite materials are typically measured for water in uncured epoxy or prepreg, with the aim to predict whether voids will grow or collapse during processing [54]. The second major consideration is water diffusion in cured composite laminates during service, with the aim of predicting hygrothermal strains [55].

Diffusion coefficients have been reported for water at room temperature in epoxy (2×10^{-13} m^2/s) [56], uncured carbon/epoxy prepreg (2.29×10^{-13} m^2/s) [54], and cured carbon/epoxy laminates (1.16×10^{-14} m^2/s) [55]. The diffusive properties of the carbon/epoxy materials change with temperature and degree of cure, but based on the reported values, water can be assumed insoluble in carbon fibres, and therefore diffusion mostly occurs through the epoxy matrix. Diffusion of dry air is less common in epoxies, however, a diffusion coefficient between 3 to 4×10^{-11} m^2/s has been reported for nitrogen gas in resin [57].

Given that a typical honeycomb skin thickness is between 1 to 2 mm, and according to Eq.(2.4), the time required for molecules to diffuse through the skin is estimated between 7 to 28 hours. The expected duration of a pre-processing vacuum hold to evacuate entrapped gasses is between 4 to 16 hours [58]. Given this, mass diffusion can be neglected as a major source of gas transport through the honeycomb skin during VBO curing.

2.2 Honeycomb core pressure during cure

Modelling the honeycomb core pressure during processing has been unnecessary to date because the consolidation pressure applied to autoclave cured honeycomb panels exceeds the honeycomb core pressure likely encountered during processing (see Figure 1.5). As a result, other than the ideal gas law of dry air or assuming a fixed relative humidity, no relationships exist to predict honeycomb core pressure during cure.

Researchers have studied the effect of temperature and moisture on the honeycomb pressure evolution during service and repair. Models were used to correlate gas pressure to hot/wet flatwise tension strength of honeycomb panels to predict joint failure during space shuttle re-entry [59,60] or honeycomb panel repair [61]. Models have been developed to predict honeycomb core pressure using moisture diffusion from the honeycomb core into the cell space [59,60]. A more conservative approach to predict honeycomb core pressure during repair considered the air within the cell space fully saturated with water vapour [61]. Granted, standing water is possible during repair operations [61], but unlikely to occur during manufacturing.

Given the low pressures encountered in VBO processing, a model is required to predict whether the honeycomb core pressure will approach the consolidation pressure. The approach outlined by *Zigrang and Bergmann* [59] and *Garrett et al.* [60] to consider moisture diffusion into the cell volume would offer reasonable predictions, and could be coupled with an air permeability model to capture the pressure response in processing conditions.

2.3 Experimental investigations of honeycomb panels

Researchers have investigated the effect of process parameters on the quality of honeycomb panels, and the key findings are presented in the following sections.

2.3.1 Resin and prepreg impregnation

Hot-melt prepregs have been shown to reduce porosity levels in both monolithic laminates and honeycomb panels, when compared to prepregs manufactured by solvent solution impregnation processes [62]. Moisture absorbed by the impregnating resin will be present in both types [1], however, the solvent solution process introduces a high volatile content into the prepreg when the reinforcement fabric passes though the resin bath during the impregnation process. In hot-melt impregnation, resin films are applied to the reinforcement fabric by rollers at elevated temperature, avoiding the need to use solvents to reduce the resin viscosity.

During elevated temperature processing, solvents can contribute to the gas pressure within the laminate, leading to a higher void content, or increase the honeycomb core pressure, thereby reducing the consolidation pressure applied to the honeycomb skin. In light of these drawbacks, solvent solution prepregs should be avoided. A resin formulated for hot-melt impregnation should be chosen for VBO processing of honeycomb panels.

The degree of resin impregnation in the prepreg reinforcement will influence the pore space available for gas flow during the vacuum hold prior to cure. Prepregs with lower impregnation levels (more dry regions) have been shown to produce void-free parts [6,62] with better skin to core bonds [62], than prepregs with higher initial degrees of impregnation. Lower impregnation levels will lead to a higher prepreg bulk-factor, increasing the likelihood of wrinkles in complex or highly contoured parts [63,64]. Increasing the prepreg impregnation level may be needed if wrinkles become problematic, however, this will likely increase the length of the vacuum hold prior to cure as the air permeability will likely decrease.

2.3.2 Adhesive film

The adhesive film plays an equally important role in honeycomb sandwich processing as the resin and impregnation process. Similar to resins, adhesives are available in many product forms that can influence panel quality and performance. The adhesive must allow entrapped gasses to escape the honeycomb core during the vacuum hold prior to cure and then flow to forms fillets with the honeycomb core during elevated temperature processing. Adhesives with a low air permeability coefficient have been observed to increase the time required for the core pressure to equilibrate to the vacuum bag pressure [15,65]. If the adhesive air permeability is too low or negligible, the adhesive can be perforated to increase the air permeability prior to cure without reducing cured panel performance [15].

Large adhesive fillets have been shown to absorb more energy during fracture [66], and as a result, improve the delamination resistance between the skin and core. Well formed, large fillets are important, however, the main failure criterion for honeycomb panels is that the core fails before the adhesive joint. Core failure is normally assessed by flatwise tension testing of cured honeycomb panels. Acceptable flatwise tension strengths are reported for VBO co-cured non-metallic honeycomb sandwich panels [9,10,67], even if bubbles are present in the cured adhesive [9,10].

An acceptable adhesive film for VBO processing has sufficiently high air permeability to allow gas evacuation from the core prior to cure and create a skin-to-core bond that produces core failure during flatwise tension or climbing drum peel testing. If poor bond strength is observed between the skin and core, sanding the exposed cells of fuzzy aramid cores before bonding has been observed to improve the skin-to-core bond strength [68].

2.3.3 Engineered pathways between the core and vacuum bag

If the air permeability of the composite skin is negligible, pathways can be introduced to evacuate entrapped air from the core during the vacuum hold. The skin can be perforated [15], or porous fabrics (such as low-density glass mat or cloth) can be placed between the core and adhesive [9] or between the prepreg and adhesive [65] to create highly porous regions between the honeycomb core and the vacuum bag. Perforating the skin and using breathing fabrics introduce additional lay-up steps and process variables. Perforations have been observed to damage carbon fibre filaments, resulting in reduced tensile strength [69]. Meanwhile, breathing fabrics add weight and depending on their areal weight, may require additional resin or adhesive to saturate the dry fabric. Ideally, introducing mechanical gas pathways should be avoided by selecting a permeable prepreg and adhesive film, but may be required to increase skin air permeability.

2.3.4 Vacuum level

The vacuum level achieved under the bag will play two very important roles in the VBO manufacturing process. First, the vacuum level is a direct measure of the gas pressure remaining in the bag, thereby defining the minimum achievable void pressure within the prepreg, and core pressure within the honeycomb. Second, the difference between the vacuum level and the atmospheric pressure will define the consolidation pressure applied to the honeycomb skin.

A direct correlation has been reported between void content and measured vacuum readings during cure of OOA prepreg laminates. A vacuum level of roughly 50 mbar was needed to reduce the void content of lab-scale laminates below 0.5 % [6]. It therefore becomes very important to achieve a high vacuum level in VBO processing because every 1 % increase in void content leads to a 7 % reduction in interlaminar shear strength [70]. Further reductions in interlaminar shear strength would be encountered as the consolidation pressure is reduced by poor vacuum levels.

A high vacuum level under the bag can lead to high vacuum levels in the honeycomb core for highly permeable skins or if the honeycomb panel is cured without close-outs. In these cases, air bubbles (sometimes referred to as foaming) may occur in the fillet of the skin-to-core bond. As discussed in the adhesive section 2.3.2, air bubbles can be detrimental to the performance of the skin-to-core joint if they lead to adhesive failure. Studies have shown that reduced vacuum level in the core has led to better skin-to-core adhesion than high vacuum levels [13,71]. In Ref. [13], metallic cores were used, which have a much higher flatwise tensile strength than non-metallic cores. As result, adhesive foaming at lower core pressures would degrade the bond strength between the skin and core. In Ref. [71], the honeycomb panels were cured without adhesive. Perhaps using an adhesive film would likely solve the poor adhesion between the skin and core at higher vacuum levels, however, panel weight would also increase. The highest achievable vacuum level should be the starting point for any VBO processing study, and only reduced if absolutely necessary.

2.3.5 Temperature cycle

Once an appropriate prepreg material is selected and a high vacuum level is achieved under the bag, the entire honeycomb panel assembly is cured in an oven at elevated temperature. The temperature profile has been identified as one of the dominant processing parameters influencing cured panel quality [71]. The cycle must allow the resin to fully saturate the dry areas in the prepreg, ensure the adhesive flows to form fillets between the skin and core, and compact the honeycomb assembly concurrently.

Many options can be varied in the temperature cycle, including dwell temperatures and ramp rates. Adjusting these parameters will change the cure and viscosity behaviour of the resin and adhesive, thereby changing the air permeability of the honeycomb skin. Introducing a devolatilization dwell near minimum viscosity has been effectively used to remove volatiles from honeycomb skins and compact the layers before gelation in autoclave curing [72,73].

The manufacturer's data sheet should be consulted to establish a baseline temperature cycle and then resin and adhesive cure models can be incorporated to predict cure and flow behaviour. If needed, the dwell temperatures and ramp rates can be adjusted to optimize the resin and adhesive flow, and skin air permeability during cure.

2.4 Honeycomb core pressure sensing

Studies of lab-scale honeycomb panels measure passive process variables, such as process temperature, vacuum bag pressure, and ambient pressure, but cannot easily measure the honeycomb core pressure. Material characterization and modelling studies focus on the constituents' influence on honeycomb core pressure by neglecting holistic effects (such as the tool-side skin and adhesive). A link is needed between the two techniques before scaling the manufacturing process to larger structures.

Approaches to measure the honeycomb core pressure in representative panels include passing capillary tubes between the core and tools side skin directly into the honeycomb cells [74, 75], passing hypodermic needles through the tool plate and bottom skin [65], and placing a vacuum valve between the core and bag-side skin [76]. These intricate approaches were used because of their useful results. These studies clearly demonstrated that minimizing the pressure differential between the autoclave and the honeycomb core reduced core crush and skin dimpling.

Honeycomb core crush is a major processing defect leading to part rejection or significant repair. Honeycomb skin dimpling is not as severe, but has been shown to reduce the tensile and compressive strength of honeycomb skins by 29 and 19 %, respectively, when compared to monolithic laminates [77]. As a result of measuring the honeycomb core pressure during the cure of actual panels, a combination of process parameters was identified to reduce core crush and skin dimpling.

Capillary tubes can be large (up to 0.8 mm in diameter [75]) and if rigid, may not conform to contoured parts. Fortunately, sensing techniques have improved recently, most notably the size and robustness of optical and piezoresistive sensors. Fibre Bragg grating (FBG) sensors have been used for structural health monitoring [78], and to measure process-induced strains between composite skins and cores [79,80]. Introducing sensors without altering the properties, behaviour, or creating leaks within the parent structure is challenging. Optical fibres are flexible and smaller than piezoresistive sensors, but are fragile. Grooves may need to be cut in the honeycomb core to protect optical fibres from being crushed by the cell walls, [80], and the sensor itself may impede fillet formation between the skin and core [80] or create resin rich areas [79].

A miniature, robust solution is needed to measure the honeycomb core pressure without impeding the process phenomenon occurring within the host structure. Microelectromechanical system (MEMS) sensors have been successfully used to measure the resin pressure in autoclave processing [81], and may offer a solution to measure honeycomb core pressure without disturbing the process phenomenon.

2.5 Summary

Material characterization and process models have been developed to offer insights into how the air permeability of the prepreg skin influences honeycomb core pressure during the pre-processing vacuum hold. During processing, similar characterization of air permeability has been performed, but this is not linked to honeycomb core pressure. An opportunity exists to develop a honeycomb core pressure process model during cure.

Most experimental studies of honeycomb panels evaluate material and process effects on panel quality in isolation—limited consideration is given to the effect of process parameters on honeycomb core pressure. Some studies have measured honeycomb core pressure using capillary tubes, and were able to link measured core pressure to panel quality. However, these results have no connection to process models. A link is needed to combine material characterization and process modelling with actual honeycomb panels.

Chapter 3

Honeycomb Core Pressure Measurements

This chapter details the experimental set-up that was used to measure the honeycomb core pressure throughout manufacturing. First, the measurement capabilities of the fixture are presented. Second, the equation is derived to calculate air permeability when a pressure differential is applied across a honeycomb skin. Third, the experimental set-up was analyzed using the computational fluid dynamics software FLUENT to identify if a 1-D flow regime exists within OOA prepregs. Finally, the concept of effective skin air permeability is introduced to calculate permeability in only the layers that allowed flow.

3.1 Instrumented pressure measurement fixture

Honeycomb panels were manufactured with only one skin–the bag-side skin–to measure the pressure inside the core. An experimental set-up was built based on the work of *Tavares et al.* [13,15,19–21] and is shown schematically in Figure 3.1. The main feature of the text fixture is a cavity with a square opening (150 mm × 150 mm) that is 60 mm deep; this is where the internal core pressure was measured. The honeycomb core was flush with the top surface of the fixture, and the honeycomb skin was placed on top of the core, extending 25 mm onto the aluminum fixture in all directions. The geometry of the skin is shown in Figure 3.3. The skin (adhesive and all prepreg layers for the test configuration) was laid-up by hand, and then trimmed to 200 mm × 200 mm before being placed on the fixture. Trimming ensured clean edges around the perimeter for edge breathing (in-plane gas flow) or sealing (transverse gas flow).

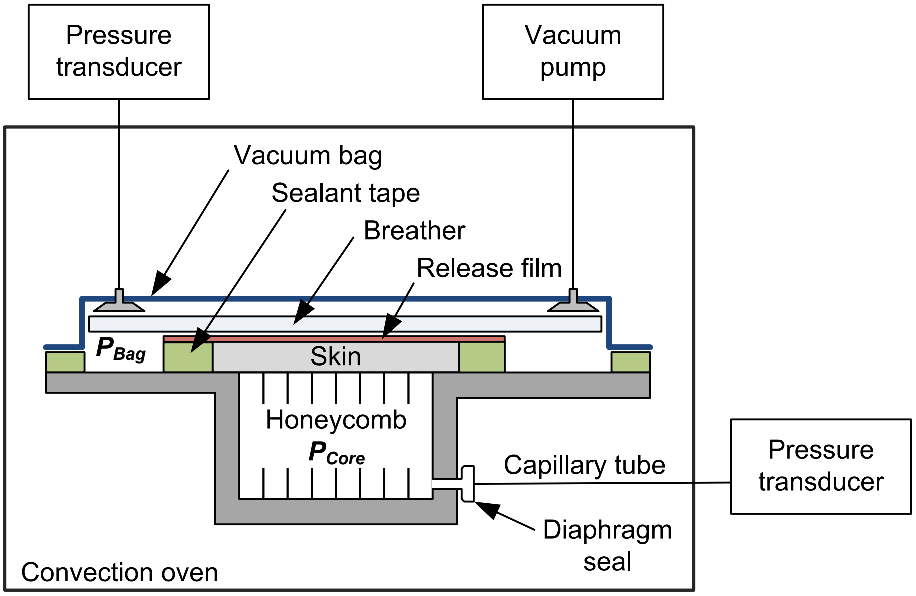

Figure 3.1. Schematic of the skin air permeability test apparatus. For in-plane measurements, the release film is non-perforated and edge breathing is used. For transverse measurements, a perforated release film is used with sealant tape around the perimeter (shown).

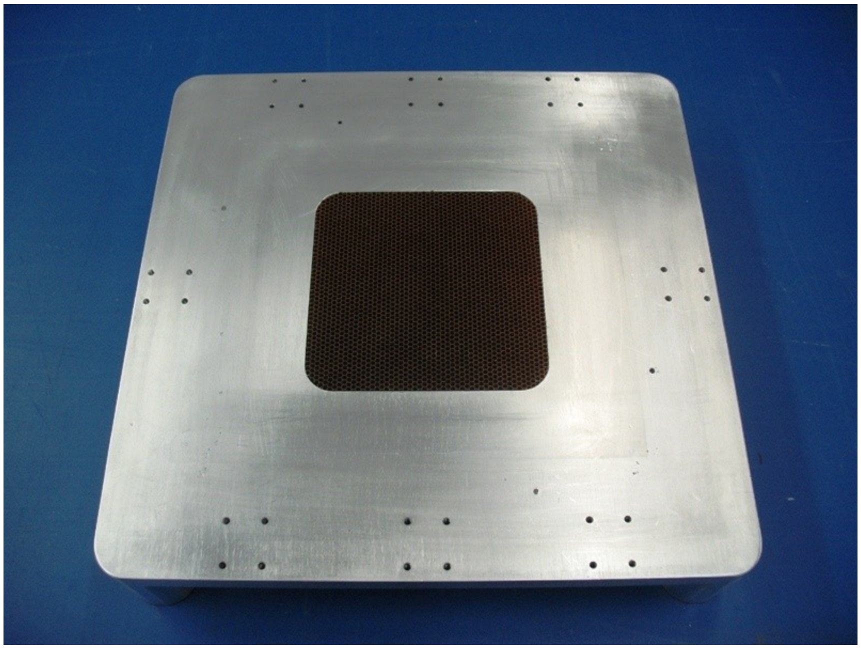

Figure 3.2. Picture of the test apparatus with honeycomb core inserted in the honeycomb core pressure measurement cavity.

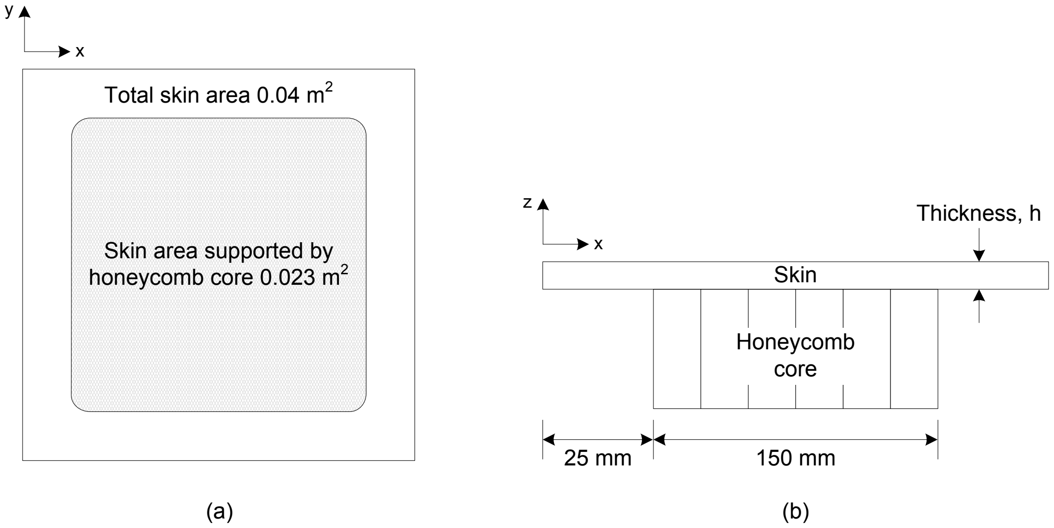

Figure 3.3. Details of the skin geometry used with the air permeability test apparatus.

The pressure inside the core was measured using a diaphragm seal that was connected to the cavity. A capillary tube connected the diaphragm seal to a Wika S-10 (range 0 to 1000 mbar) pressure transducer. The vacuum bag pressure was measured by connecting a 6.35 mm internal diameter vacuum hose between the vacuum bag and a Wika A-10 (Range 0 to 3000 mbar) pressure transducer. The pressure transducers were located outside the oven because the electronics are rated to 80 °C, and process temperatures were up to 125 °C.

3.2 Calculating air permeability

When vacuum is applied under the bag in Figure 3.1, the honeycomb core pressure will decrease if flow occurs through the skin and if no leaks are present within the fixture. If the mass flux through the skin is assumed to be constant during the measurement, the conservation of mass can be written as

$$\nabla \cdot \left(\rho \bar{v}\right) = 0 \tag{3.1}$$

where ρ is the density of the gas and $\bar{v}$ is the velocity. For laminar flow, the conservation of momentum of a fluid in a porous medium is governed by Darcy's law

$$\bar{v} = -\frac{\overline{\overline{K}}}{\mu} \nabla \bar{P}. \tag{3.2}$$

If the prepreg is isotropic in the X-Y plane, the flow through the skin can be analyzed in the X-Z direction, and Eq. (3.1) becomes

$$\frac{\partial(\rho v_x)}{\partial x} + \frac{\partial(\rho v_z)}{\partial z} = 0 \tag{3.3}$$

where $v_x = 0$ for 1-D transverse flow and $v_z = 0$ for 1-D in-plane flow. Working in the X direction to define the 1-D governing flow equation, $v_z = 0$, and substituting v_x from Eq. (3.2) into Eq. (3.3) yields

$$\frac{d}{dx}\left[-\rho \frac{K}{\mu} \frac{dP}{dx}\right] = 0 \tag{3.4}$$

Using the ideal gas law to correlate for changes in gas density, integrating Eq. (3.4) twice, and applying the following boundary conditions:

$$P(x = 0) = P_{Core}(t)$$

$$P(x = L) = P_{Bag}$$

yields the following pressure profile in the skin as function of position

$$P = \left[\frac{\left(P_{Bag}^2 - P_{Core}(t)^2\right)}{L} x + P_{Core}(t)^2\right]^{\frac{1}{2}} \tag{3.5}$$

Accordingly, the derivative of the pressure profile at the interface between the core and skin is

$$\left.\frac{dP}{dx}\right|_{x=0} = \frac{P_{Bag}^2 - P_{Core}(t)^2}{2L\,P_{Core}(t)}. \tag{3.6}$$

In order to calculate the permeability, we need to incorporate the flow rate of gas into the skin at the skin-to-core interface, where $x = 0$. Substituting Eq. (3.6) into Eq. (3.2) gives

$$-\frac{KA}{2L\mu} = Q \frac{P_{Core}(t)}{P_{Bag}^2 - P_{Core}(t)^2}. \tag{3.7}$$

Since the volumetric flow rate, Q, is related to the mass flow rate, dm/dt and the density of the gas by

$$Q = -\frac{1}{\rho}\frac{dm}{dt}, \tag{3.8}$$

and the mass flow into the skin is proportional to the change in pressure in the honeycomb core, the mass flow rate can be related to the change in honeycomb core pressure:

$$\frac{dm}{dt} = \frac{dP_{Core}}{dt}\frac{m(t)}{P_{Core}(t)} = \frac{dP_{Core}}{dt}\frac{\rho V_{Core}}{P_{Core}(t)}. \tag{3.9}$$

Eq. (3.8) and Eq. (3.9) can be substituted into Eq. (3.7) to describe the change in core pressure with time:

$$\frac{KA}{L\mu V_{Core}} = \frac{dP_{Core}}{dt}\frac{2}{P_{Bag}^2 - P_{Core}(t)^2}. \tag{3.10}$$

Integrating Eq. (3.10) from *0* to *t* yields:

$$-\frac{KAP_{Bag}}{L\mu V_{Core}}t = \ln\left[\frac{\left(P_{Core}(0)+P_{Bag}\right)\left(P_{Core}(t)-P_{Bag}\right)}{\left(P_{Core}(0)-P_{Bag}\right)\left(P_{Core}(t)+P_{Bag}\right)}\right] \tag{3.11}$$

to describe the one-dimensional laminar flow of a compressible gas at isothermal and adiabatic conditions through a porous medium.

The permeability, *K*, can be calculated by the slope of the left hand side of Eq. (3.11) versus time straight line plot. Outside the linear region, Eq. (3.11) returns errors as the honeycomb core pressure, $P_{Core}(t)$, approaches the vacuum bag pressure, P_{Bag}, because

$$\lim_{P_{Core}(t)\to P_{Bag}} \ln\left[\frac{\left(P_{Core}(0)+P_{Bag}\right)\left(P_{Core}(t)-P_{Bag}\right)}{\left(P_{Core}(0)-P_{Bag}\right)\left(P_{Core}(t)+P_{Bag}\right)}\right] = \infty.$$

Once the air permeability of the honeycomb skin is known, Eq. (3.11) can be solved for P_{Core} to predict the pressure evolution in the core during the vacuum hold prior to cure [13]:

$$P_{Core}(t) = P_{Bag}\frac{c+e^{-st}}{c-e^{-st}} \tag{3.12}$$

where *c* and *s* are:

$$c = \frac{P_{Core,i}+P_{Bag}}{P_{Core,i}-P_{Bag}}, \quad s = \frac{KAP_{Bag}}{L\mu V_{Core}}. \tag{3.13}$$

3.2.1 Model assumptions

To calculate air permeability, Eq. (3.11) ignores inertial losses in the flow by assuming laminar flow through the skin. Laminar flow occurs when the Reynolds numbers (Re) are less than 10, where

$$Re = \frac{\rho l v}{\mu} \tag{3.14}$$

where ρ is density, l is the reference length, v is flow velocity, and μ is air viscosity. The reference length was taken as the fibre diameter [33]. Fortunately, the dependence of air viscosity on pressures between 100 and 1000 mbar varies by only 0.05 % at room temperature [82], therefore a constant value for viscosity of 1.85 x 10^{-5} Pa·s was used. Given the expected air permeability of the prepregs, the Reynolds number was estimated between 0.01 and 0.6 for the flow in these experiments, avoiding inertial effects.

3.3 Analysis of experimental set-up in ANSYS FLUENT

A 2-D numerical analysis was performed on the honeycomb skins in the X–Z plane with boundary conditions representing the experimental test fixture shown in Figure 3.1. Flow of a compressible, laminar, steady-state fluid through a rigid porous medium was simulated using the ANSYS computational fluid dynamics program FLUENT. Porous media conditions were simulated in FLUENT by adding a momentum sink to the governing momentum equations [83]. The momentum sink is comprised of a viscous loss term and an inertial loss term. The inertial loss was neglected because the Reynolds number estimation was laminar, as discussed in section 3.2.1.

3.3.1 Governing equations solved by FLUENT

A pressure based solver was used in FLUENT to solve the governing equations for conservation of mass, momentum, and energy. The conservation of mass was:

$$\nabla \cdot (\rho \bar{v}) = 0 \tag{3.15}$$

The conservation of momentum reduced to Darcy's law:

$$\bar{v} = -\frac{K}{\mu} \nabla P \tag{3.16}$$

and the ideal gas law equation of state was chosen to describe the density of the fluid:

$$\rho = \frac{P_{op} + P}{\frac{R_u}{\omega} T} \tag{3.17}$$

where P is the local gauge pressure predicted by FLUENT and P_{op} is the operating pressure defined by:

$$P_{absolute} = P_{op} + P \tag{3.18}$$

The viscosity was assumed to remain constant throughout the simulation at 1.85 x 10^{-5} Pa·s because of the negligible changes in viscosity at the pressures encountered in these simulations [82].

In FLUENT, if a compressible fluid is selected to permeate the porous medium, the conservation of energy equation is automatically activated:

$$\frac{\partial}{\partial t}(\rho E) + \nabla \cdot \left(\bar{v}(\rho E + P)\right) = \nabla \cdot [\lambda \nabla T] \tag{3.19}$$

where E is the total fluid energy and λ is the thermal conductivity. The FLUENT analysis was performed at a constant temperature of 298 K, similar to the room temperature experiments. Errors could arise in the simulations if a constant operating temperature is not specified in FLUENT.

Prior to analyzing the flow in the experimental set-up, a benchmarking exercise was conducted on a rectangular sample with a pressure differential applied at the boundaries. This idealized simulation of a Darcy flow problem generated the steady-state pressure profile, validating the correct implementation of Darcy's law in FLUENT.

3.3.2 Porous zone mesh, properties, and boundary conditions

A structured quadrilateral cell mesh was generated for the porous zone using the ANSYS Meshing application in ANSYS Workbench. The mesh size was 2,000 elements. A segregated algorithm was used to solve the governing equations sequentially using the SIMPLE pressure-velocity coupling scheme to enforce mass conservation within each element. A second-order discretization scheme was chosen for the pressure, and first-order upwind discretization for density. The solution convergence criterion was a residual with a norm smaller than an absolute tolerance of 1×10^{-3}; convergence was achieved after 21–101 iterations.

A schematic of the boundary conditions for the in-plane simulations are shown in Figure 3.4a and the transverse simulations in Figure 3.5a. For both flow simulations, a pressure inlet condition was used for the air entrapped in the honeycomb core, a wall condition was used where the skin was seated against the aluminum test fixture, and a symmetric boundary condition was used in the centre of the skin. For in-plane flow (Figure 3.4a), a pressure outlet was used where the edge breathing was placed around the perimeter of the prepreg skins, and a wall boundary condition was used for the non-perforated release film. For transverse flow (Figure 3.5a), a pressure outlet was used for the perforated release film placed on top of the skin, and a wall was used at the perimeter of the prepreg skin to represent the sealant tape placed around the edges.

The rectangular skin was defined as a porous zone, and assigned air permeability values from the scientific literature. Measured in-plane ($K_{xx} = 2.2 \times 10^{-14}$ m^2) and transverse ($K_{zz} = 1.4 \times 10^{-16}$ m^2) air permeability values were found for the plain weave prepreg used in this study [84]. Unfortunately, measured air permeability values for the 5 harness satin and unidirectional cross-ply laminates used in this study were not available.

Air permeability values for out-of-autoclave prepregs with similar fabric properties were found in the literature. In-plane (K_{xx}) values for air permeability ranged from 9.6×10^{-15} m^2 for a cross-ply unidirectional prepreg [37], to 4.3×10^{-14} m^2 for 5 harness satin [39], and transverse (K_{zz}) air permeability values were much lower than in-plane, starting at 1×10^{-18} m^2 for 5 harness satin [39], increasing slightly to 3×10^{-18} m^2 for cross-ply unidirectional laminates [19]. The anisotropy of the in-plane and transverse air permeability values is 2 orders of magnitude for plain weave, 3 orders of magnitude for unidirectional cross-ply laminates, and 4 orders of magnitude for 5 harness satin prepregs.

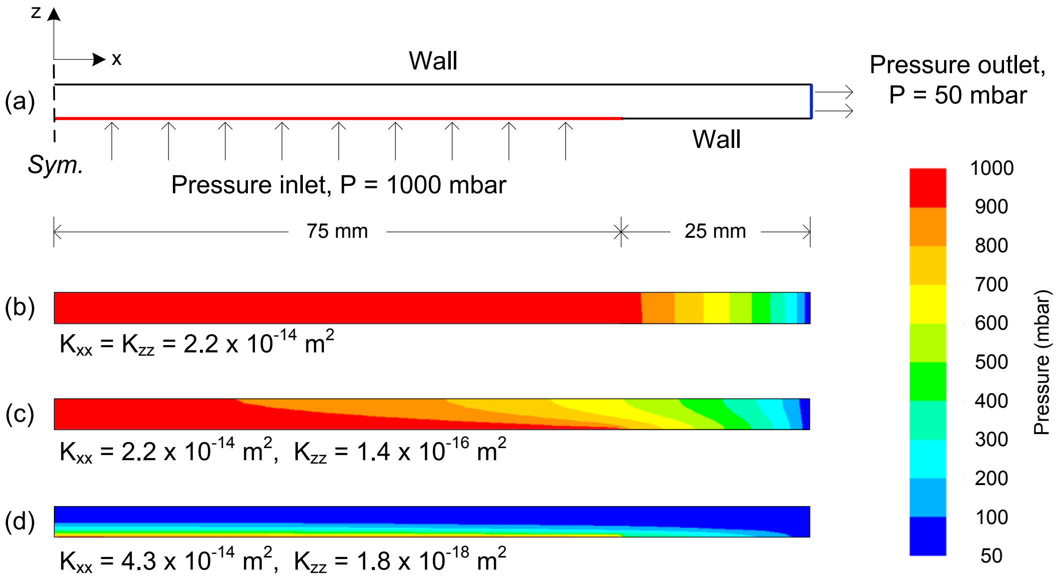

Figure 3.4. In-plane gas flow simulations in FLUENT of a honeycomb skin: (a) boundary conditions used in the simulations and pressure gradients for a material with (b) isotropic permeability, (c) anisotropic permeability separated by 2 orders of magnitude (such as plain weave), and (d) anisotropic permeability separated by 4 orders of magnitude (such as 5 harness satin).

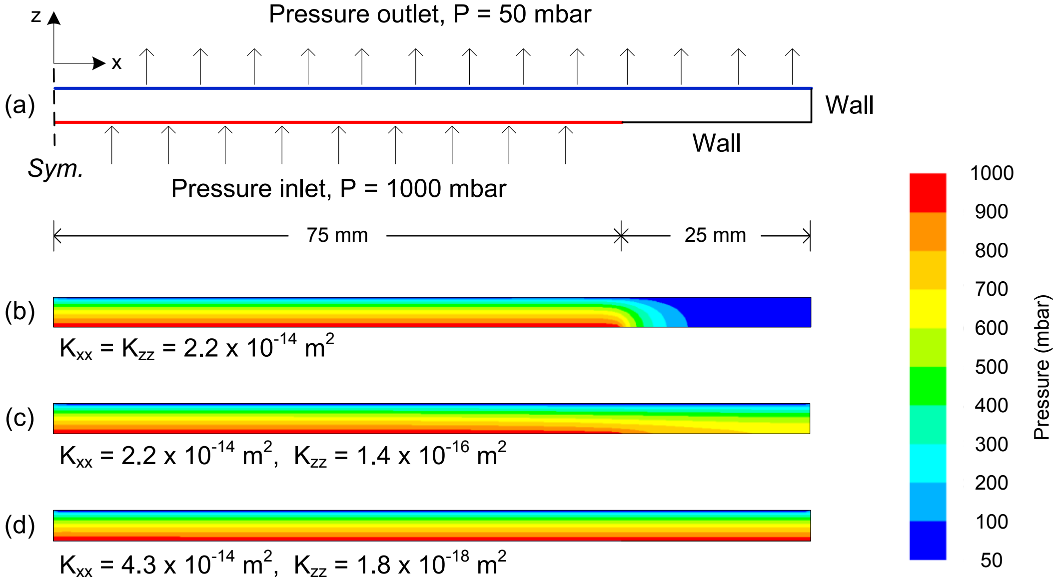

Figure 3.5. Transverse gas flow simulations in FLUENT of a honeycomb skin: (a) boundary conditions used in the simulations and pressure gradients for a material with (b) isotropic permeability, (c) anisotropic permeability separated by 2 orders of magnitude (such as plain weave), and (d) anisotropic permeability separated by 4 orders of magnitude (such as 5 harness satin).

Simulations were performed for three cases where prepreg permeability was isotropic (representing 1-D Darcy flow), slightly anisotropic (plain weave skins), and severely anisotropic (representing 5 harness satin skins). Simulations were performed with the unidirectional skins, the results lie in-between the plain weave and 5 harness skins, but are not shown because the experiments with the unidirectional cross-ply skins had no measureable air permeability, which will be discussed in section 4.2.3.2. The air permeability values that were used to define the porous zones were $K_{xx} = K_{zz} = 2.2 \times 10^{-14}$ m^2 for isotropic, $K_{xx} = 2.2 \times 10^{-14}$ m^2 and $K_{zz} = 1.4 \times 10^{-16}$ m^2 for slightly anisotropic, and $K_{xx} = 4.3 \times 10^{-14}$ m^2 and $K_{zz} = 1.8 \times 10^{-18}$ m^2 for the severely anisotropic case.

A constant thickness was used to simplify the analysis for each skin. The skin thickness used in the simulations was taken when skin thickness had stabilized during the vacuum hold, which will be discussed in Chapter 4.

3.3.3 Simulation results

Pressure contours for the in-plane gas evacuation simulations are shown in Figure 3.4b–d. The contours are shown for a 5 mm thick skin, in order to see the pressure gradient profile. For in-plane air evacuation, the case of isotropic permeability demonstrates that the pressure gradient mainly exists at the transition from honeycomb core to monolithic laminate, where the skin is seated on the experimental fixture. The near-vertical lines in the pressure contours are representative of a 1-D Darcy flow, and the decreased spacing of the pressure bands indicates the nonlinearity of the pressure change that occurs across the length of the porous zone due to gas compressibility.

As the skin becomes more anisotropic, as in Figure 3.4c & d, a 2-D pressure gradient occurs within the skin, as shown by the non-vertical lines in the pressure contours. Since the air is supplied at the skin-to-core interface, it must travel into the material before it can be extracted at the perimeter, through the edge breathing. The simulations demonstrate that air is more likely travelling in the bottom few plies because the high in-plane air permeability and the low transverse air permeability prevent equal distribution of the pressure gradient through the skin thickness.

If a 1-D pressure gradient and the area normal to flow were assumed to occur uniformly in all layers of the skin, the in-plane air permeability of the material would be underestimated. Therefore, the concept of effective skin air permeability, K^*, is introduced to calculate permeability in only the layers that allow flow:

$$K^* = PG \times ANF \times K \tag{3.20}$$

where *PG* and *ANF* (summarized in Table 3.1) are the percent 1-D Darcy pressure gradient and area normal to flow, respectively, and *K* is the air permeability calculated using Eq. (3.11). Effective skin air permeability is akin to effective porosity, where only interconnected pores are considered to contribute to flow across a porous medium [22-23]. From the in-plane simulations, the average pressure gradient and area normal to flow were calculated for each skin thickness. These values were compared to a 1-D flow, and the resulting percentage of a 1-D pressure gradient and area normal to flow is shown in Table 3.1.

Table 3.1. FLUENT simulation results of 1-D Darcy pressure gradient and cross-sectional area normal to flow for the plain weave and 5 harness satin prepreg skins.

			Skin thickness (mm)		
			0.75	1.25	2.11
In-plane	Plain weave	PG (%)	86.2	76.0	61.3
		ANF (%)	100	100	100
	5 Harness satin	PG (%)	41.8	34.8	24.3
		ANF (%)	100	100	57.1
Transverse	Plain weave	PG (%)	100	100	100
		ANF (%)	57.8	60.9	69.2
	5 Harness satin	PG (%)	100	100	100
		ANF (%)	86.7	91.2	93.4

Legend:
PG – pressure gradient
ANF –area normal to flow

The transverse gas evacuation pressure contours are shown in Figure 3.5b–d. The skin with isotropic air permeability values has an area normal to flow that is slightly larger than the area supported by the honeycomb core. As the skin air permeability becomes more anisotropic, the area normal to flow increases toward the total area of the prepreg skin. The percentage of the total skin area normal to flow was calculated for each skin thickness, and is summarized alongside the in-plane simulations in Table 3.1. In contrast to the in-plane simulations, the pressure gradient was 1-D for transverse gas evacuation because the pressure inlet and pressure outlet were parallel.

3.4 Summary

A fixture to measure honeycomb core pressure was constructed, and the equation to extract air permeability of the honeycomb skin was developed. Simulations were performed on the experimental test set-up to identify the flow regime for out-of-autoclave prepreg honeycomb skins. Computational fluid dynamics (CFD) modelling of the skins in FLUENT revealed a 2-D pressure gradient because OOA prepregs have an in-plane air permeability coefficient that is at least two orders of magnitude higher than the transverse direction. The simulations identified that in-plane gas flow prevails in the layers adjacent to the core for prepregs with low transverse air permeability. The concept of effective skin air permeability was introduced to calculate permeability in only the layers that allowed flow. All permeability results presented in the following chapters were corrected, and represent effective permeability coefficients.

Chapter 4

Physical Characterization of Honeycomb Skins

In this chapter, three out-of-autoclave (OOA) prepregs with different fabric styles are studied from the same manufacturer: unidirectional, plain weave, and 5 harness satin. First, the air permeability is measured during the vacuum hold prior to cure in-order to select a suitable skin material and breathing direction for honeycomb skins. Second, the air permeability is characterized during elevated temperature processing to identify how the skin evolves during the manufacturing process. Throughout this chapter, the air permeability results are correlated to the prepreg pore space using micro-CT in-order to identify how the fabric style influences the flow of air in OOA prepregs.

4.1 Materials

Hot-melt OOA prepregs from Cytec Engineered Materials were used throughout this thesis. Three fibre architectures were initially considered: unidirectional, plain weave and 5 harness satin. Cycom® 5320 resin was pre-impregnated into the fibre architectures by the material supplier. Photographs highlighting the differences in fibre architecture are shown in Figure 4.1 for the prepregs.

The fibre architectures have varying degrees of crimp—the number of warp and weft tow overlaps per unit area. The unidirectional architecture is not woven, leading to zero crimp, the 5 harness satin has more fabric crimp, and the plain weave fabric has the most crimp of the three materials studied because every warp tow overlaps every weft tow. The physical properties of the prepregs are summarized in Table 4.1. An adhesive film from 3M, AF 163-2K with a 294 g/m^2 areal weight, was used to co-cure the prepreg layers to the Nomex® honeycomb core. The core itself was 20 mm thick, with 3.12 mm diameter hexagonal cells, and a density of 96 kg/m^3.

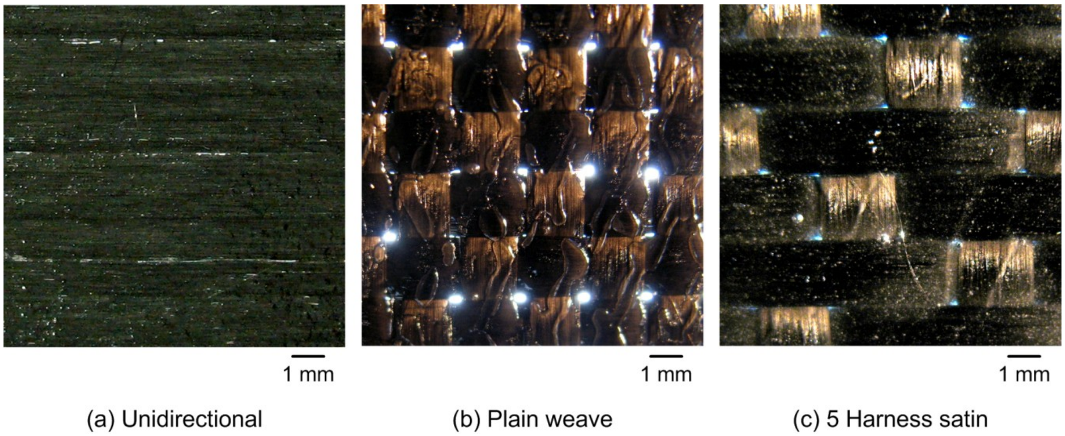

(a) Unidirectional (b) Plain weave (c) 5 Harness satin

Figure 4.1. Photographs of the prepregs with a fluorescent light source placed under the prepreg to highlight the extent of fabric crimp.

Table 4.1. Prepreg physical properties.

Prepreg	Fibre	Tow size (filaments/ tow)	Areal weight (g/m^2)	Resin content (wt. %)
Unidirectional	T40/800B	24,000	145	33
Plain weave	T650–35	3,000	196	36
5 Harness satin	T650–35	6,000	376	36

The consumable materials used throughout this thesis were a Fluorinated ethylene propylene (FEP) release film (non-perforated, and P3 with 0.38 mm perforations and 6.35 mm centres), breather cloth with an areal density of 0.34 kg/m^2, nylon vacuum bag, sealant tape, and 8 cm wide fibreglass cloth was used for edge breathing, when needed.

4.2 Skin behaviour during the vacuum hold prior to cure

The effect of fabric architecture on core air evacuation was evaluated during the vacuum hold prior to cure. Honeycomb skins were tested with of one layer of adhesive and between 1 to 12 prepreg plies, according to the text matrix shown in Table 4.2. The following sections outline the pore space characterization of the honeycomb skins and the corresponding air permeability during the vacuum hold prior to cure.

Table 4.2. Air permeability test matrix for transverse and in-plane breathing strategies.

Fibre architecture	n: Number of layers
Unidirectional $[0/90]_n$	4 8 12
Plain weave $[0]_n$	2 4 8
5 Harness satin $[0]_n$	1 2 4

4.2.1 Micro-CT imaging of honeycomb skins prior to cure

A Skyscan 1172 High-Resolution micro-CT system was used to scan a total of six prepreg samples. The scan resolution, or the size of the smallest detectable detail, was 7 µm/pixel. The scans were analyzed at both the micro and macro scale. At the micro-scale, the prepreg dry area percentage was calculated by observing the decrease in visible dry fibre tow area on successive micro-CT scans:

$$\%\, Dry\ Area = \frac{A_{Dry\,Tow}}{A} \times 100\ \% \tag{4.1}$$

where $A_{Dry\ Tow}$ is the visible dry fibre tow area and A is the total sample cross-sectional area. The macro-porosity in the prepreg layers was measured directly using the 3-D analysis feature of Skyscan's CTAn software. No heat was applied to the samples at any point during handling (layup, vacuum hold, or during scanning), therefore the resin viscosity remained constant at all times.

Two 100 mm × 100 mm laminates were laid-up by hand for each fabric architecture, and an 18 mm × 18 mm sample was cut from the center of one sample immediately after lay-up and scanned. The other laminate was vacuum bagged with edge breathing, and held under full vacuum for 16 h. An 18 mm × 18 mm sample was cut from the compacted laminate and scanned. The sample scanned immediately after lay-up represents the material in its as-received condition from the material supplier. The resin distribution and dry tow area of the prepregs were captured in the as-received condition, and once again after vacuum was applied in-order to identify how the resin distribution and fibre dry tow area changed during the vacuum hold.

Representative micro-slices are shown in Figure 4.2 for each material, and a summary of the sample analysis is presented in Table 4.3. The as-received samples show a higher level of macro-porosity around the tows and between the prepreg plies. By observing the x-ray micrographs, variations in pore space morphology is observed between the three fibre architectures.

For the plain weave (Figure 4.2a), the pore space is due to the gaps created by the interlacement of the warp and weft tows. The pores create a repeating pattern that was observed to create a connected transverse pore space through the thickness of the skin.

The 5 harness satin prepreg (Figure 4.2b) has almost twice the macro-porosity, however only isolated pores were observed. The 5 harness satin has interlacements of the warp and weft tows, however the crimp is less than plain weave. As a result, the macro-porosity observed in the laminate is mainly isolated pockets of entrapped air in-between the plies, opposed to connected pores.

The unidirectional material had negligible macro-porosity after layup (Figure 4.2c), even before vacuum was applied. Unidirectional plies are very flat by nature, and as a result, entrap few voids between layers. The volume of air that needs to be removed from the unidirectional OOA material is minimal during the vacuum hold. Unfortunately, no visible connected pore space was observed in the transverse direction, suggesting this material may encounter air evacuation challenges for honeycomb panels.

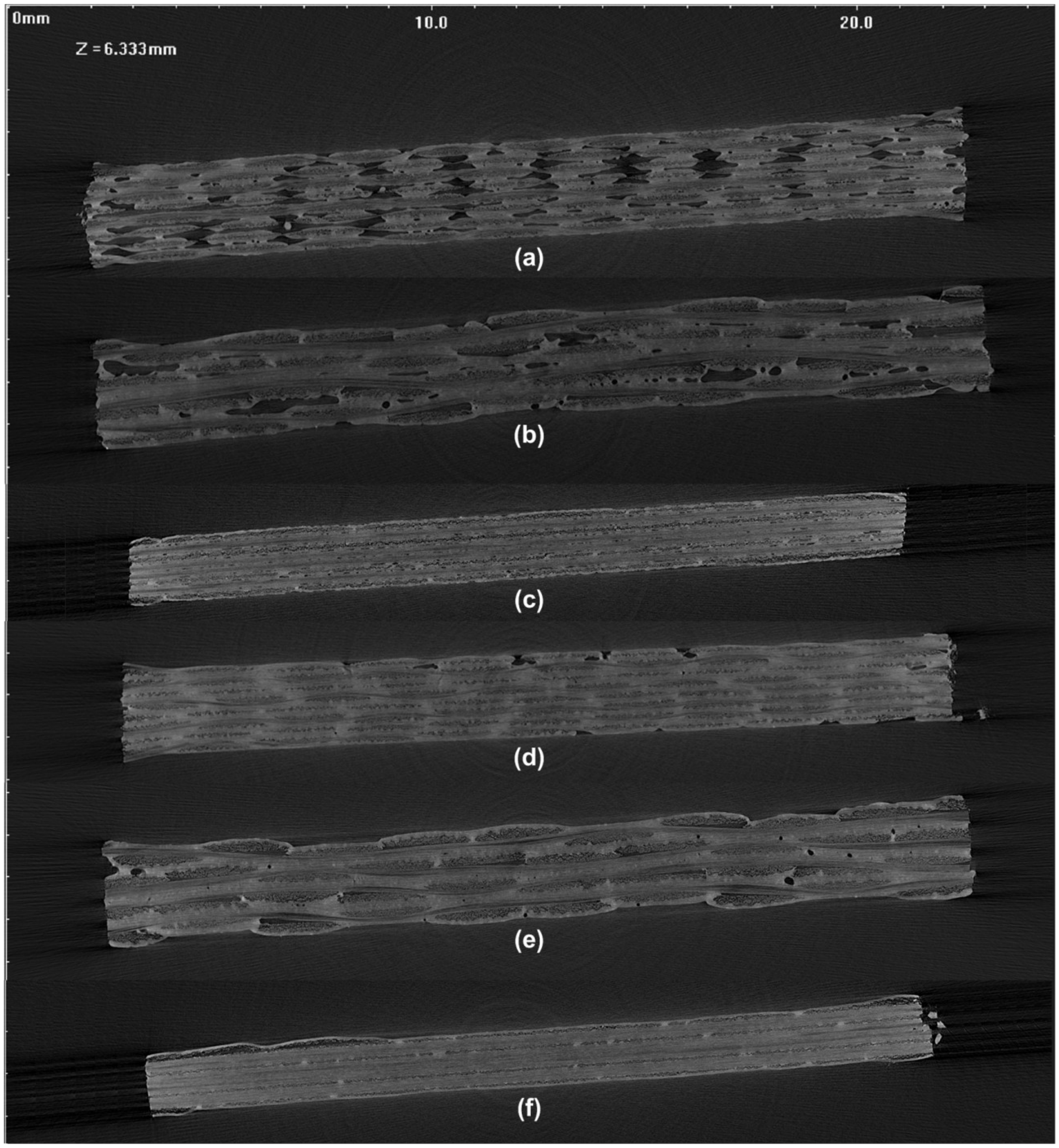

Figure 4.2. Representative x-ray micrographs at 7 μm/pixel for uncompacted (a) plain weave prepreg showing the alignment of the macro-porosity networks, (b) 5 harness satin prepreg showing large porosity, but no connected networks, (c) very straight unidirectional prepreg with no macro-porosity. After a 16 h vacuum hold at room temperature, only micro-porosity was detected within the tows of the (d) plain weave, (e) 5 harness satin, and (f) unidirectional prepregs.

Table 4.3. Micro-CT scan results.

Sample	Material	Lay-up	Macro-porosity (%)	$A_{Dry\ Tow}$ [c] (mm^2)	Prepreg dry area [d] (%)
A	Plain weave[a]	$[0]_8$	7.94	11.4	24.4
B	5 Harness satin[a]	$[0]_{2S}$	12.0	12.7	26.6
C	Unidirectional[a]	$[0/90]_{4S}$	0.05	12.3	46.8
D	Plain weave[b]	$[0]_8$	0.50	9.12	23.5
E	5 Harness satin[b]	$[0]_{2S}$	2.41	12.6	29.0
F	Unidirectional[b]	$[0/90]_{4S}$	0.00	9.91	39.7

[a] Uncompacted
[b] Compacted
[c] Visible dry tow area
[d] Calculated from Eq. (4.1)

Once the prepregs were compacted under vacuum for 16 h, the macro-porosity decreased to nearly 0 % for both the plain weave (Figure 4.2d) and the unidirectional prepregs (Figure 4.2f). Higher porosity of 2.41 % remained within the 5 harness satin prepreg (Figure 4.2e), caused by isolated pockets of entrapped air in the resin rich regions between layers. The residual air pockets within the 5 harness satin laminate demonstrate the difficulty of complete air evacuation for that prepreg. Even for small 100 mm × 100 mm laminates with full edge breathing, incomplete air evacuation within the resin-rich layers was observed after a 16 h vacuum hold. Macro-pore reduction during the vacuum hold does not preclude air permeability because partially impregnated tows remain within the prepregs.

The micro-porosity of the prepregs was analyzed by comparing the evolution of visible dry fibre tow area and percent sample dry tow area during the vacuum consolidation. The results are included in Table 4.3. During the vacuum hold, the visible dry fibre tow area of the unidirectional and plain weave fabrics decreased by 19.5 % (from 12.3 mm^2 to 9.9 mm^2) and 20 % (from 11.4 mm^2 to 9.1 mm^2), respectively, while the 5 harness satin decreased by only 1 % (from

12.7 mm^2 to 12.6 mm^2). The larger decrease in the plain weave and unidirectional fabrics is likely due to a combination of fibre re-arrangement and resin flow into the dry areas. The 5 harness satin is more likely to show consistent in-plane air permeability during and after the vacuum hold because the fabric retains most of its initial dry porous network.

The collapsing macro-pores during the vacuum hold can influence the evolution of percent sample dry tow area. The 5 harness satin percent sample dry tow area increased after the vacuum hold because the consolidation pressure collapsed the macro-pores, meanwhile the total visible dry tow area remained constant. On the other hand, the plain weave and unidirectional prepregs showed a decrease in percent sample dry tow area, caused by both collapsing macro-porosity and decreasing visible dry tow areas. These trends are visually observed in Figure 4.2.

In spite of the reduction in air evacuation paths, micro-porosity may remain in both unidirectional and plain weave skins; voids smaller than 7 μm, and therefore difficult to detect at the current scan resolution, possibly remain inside the dry tow areas and between plies. A higher scan resolution at 2 μm/pixel could reveal more microscopic details within the tows, but would have reduced the sample size to roughly 3 mm × 3 mm, reducing the number of tows scanned.

4.2.2 Skin consolidation prior to cure

The changes in macro-porosity and visible dry tow area observed in the micro-CT imaging indicate that a thickness change should occur in the honeycomb skins during the vacuum hold prior to cure. This can lead to errors in reported permeability coefficients because the thickness is needed for flow length in the transverse direction, and cross-sectional area in the in-plane direction.

To identify the skin thickness evolution during the vacuum hold, a 100 mm × 100 mm skin was laid-up by hand for each configuration presented in Table 4.2. The thickness was measured after at 3 locations using a micrometer to obtain a baseline thickness after lay-up. Careful attention was paid to avoid compressing the skin between the micrometer spindle and anvil when taking the measurements.

The skins were then placed on a flat aluminum tool covered with non-perforated release film. Edge breathing was placed around the perimeter of each sample, followed by one layer of perforated release film, breather, and the vacuum bag was secured to the tool with sealant tape. The sample was held under 50 mbar of vacuum for 5 minutes, the bag was removed, and thickness measurements were taken for each skin as described above. This process was repeated for increasing time intervals over a 24 h vacuum hold.

The skin thickness evolution during the 24 h vacuum hold is presented in Figure 4.3. The results indicate that the majority of the thickness change due to consolidation occurs within the first 15 to 30 min of the vacuum hold, and that the skin thickness is consistent after the first hour. As a result, the average thickness between hours 1 to 24 was used in the permeability calculations.

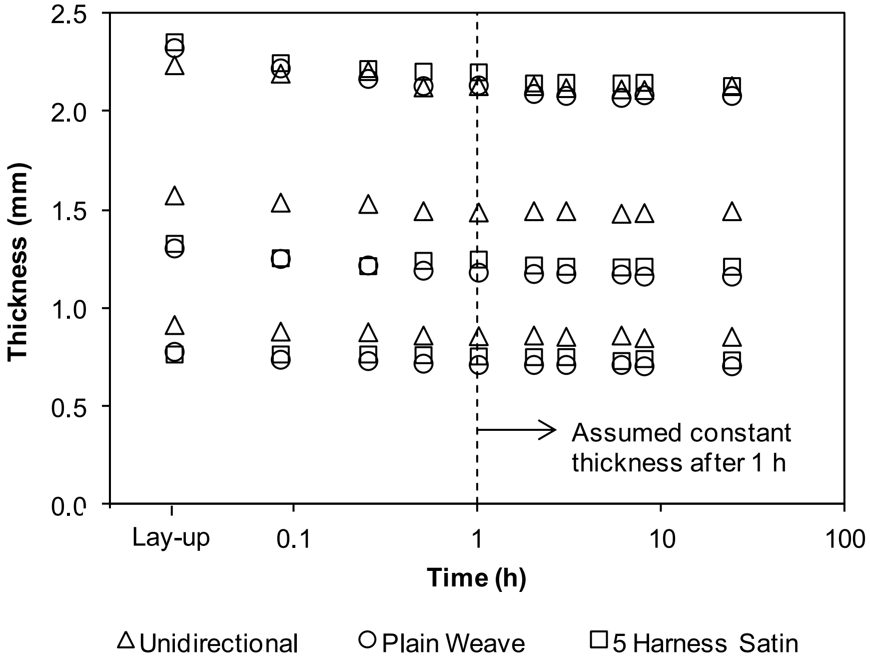

Figure 4.3. Thickness measurements of honeycomb skins during the 24 h vacuum hold prior to cure.

4.2.3 Evolution of honeycomb core pressure prior to cure

In-plane and transverse air permeability measurements were performed using the experimental fixture presented in Figure 3.1. The in-plane air permeability experiments were restricted to in-plane flow by placing a non-perforated release film over the skin and using edge breathing around the perimeter to permit gas evacuation by the vacuum bag assembly. The transverse permeability experiments were performed with sealant tape placed around the perimeter of the skin to prevent in-plane air evacuation, and a perforated release film was used to connect the prepreg stack to the vacuum bag assembly.

One layer of breather was placed over the release film, and the vacuum bag was secured to the test fixture with sealant tape. Neither heat nor vacuum pressure was applied to the skin during lay-up. The first application of vacuum was when the vacuum pump was started for the experiment. A vacuum hold was applied for 24 h for each skin configuration in Table 4.2, and each test was repeated five times with new samples.

An example of the honeycomb core pressure data recorded for one skin configuration is shown in Figure 4.4. The pressure decrease in these experiments occurred in the first 10 h of the vacuum hold. Three features are apparent when examining this data set. First, even though vacuum pressure is applied at time 0, a period of time passes before the pressure begins to decrease. Second, the rate with which the pressure decreases shows considerable variability. And third, the pressures at the end of each experiment are different.

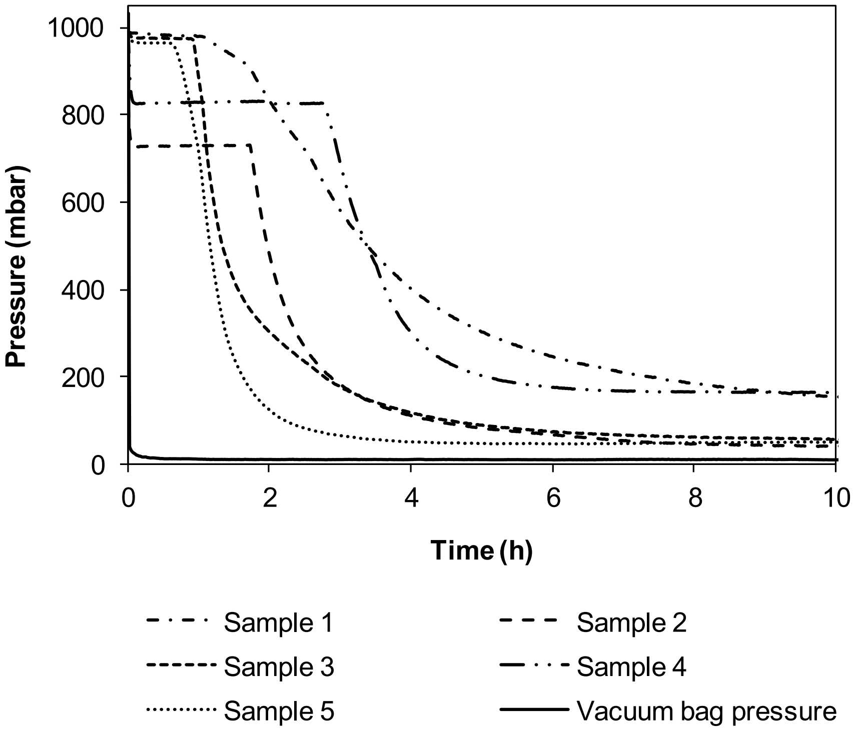

Figure 4.4. Experimental data showing the measured honeycomb core pressure for the 4-ply plain weave skins tested in the transverse breathing direction.

Large variability in experimental data required definition of three parameters to describe the pressure behaviour in each experiment. The parameters are shown in Figure 4.5. First was the delay time: the time between starting the vacuum hold and the beginning of the honeycomb core pressure decrease. Second was the air permeability measurement: when pseudo-steady state flow was observed in the recorded pressure data. This allowed the flow capacity of each skin material to be estimated by calculating the air permeability using Eq. (3.11) to a coefficient of determination greater than 0.99 for the linear region.

The coefficient of determination, R^2, was defined as [87]:

$$R^2 = 1 - \frac{\sum_{i=1}^{m} (y_i - \hat{y})^2}{\sum_{i=1}^{m} (y_i - \bar{y})^2}, \tag{4.2}$$

where y_i is the observed value, $\hat{y}$ is the predicted value, and

$$\bar{y} = \frac{1}{m}\sum_{i=1}^{m} y_i \quad . \tag{4.3}$$

The third and final parameter was the lowest observed pressure: the magnitude of honeycomb core pressure measured after the 24 h vacuum hold. Together, these parameters define the time before air evacuation begins, how quickly evacuation proceeds, and the pressure when the experiment ended.

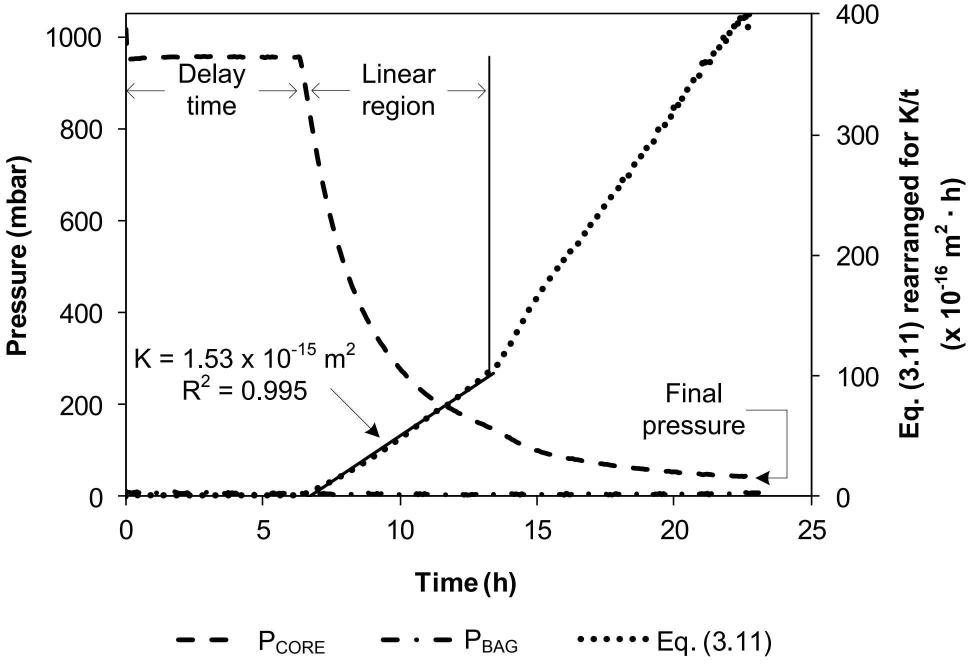

Figure 4.5. Example of permeability test data from an in-plane permeability experiment on a 4-ply, 5 harness satin skin. This graph shows a period of constant pressure before air evacuation began. Three parameters (delay time, air permeability, and final pressure) are needed to define the evacuation behaviour of a honeycomb skin.

4.2.3.1 Delay time prior to honeycomb core pressure decrease

The delay time for the fibre architectures is presented in Figure 4.6. Once the vacuum pump was connected to the vacuum bag, the initial core pressure decreased slightly from atmospheric pressure in each experiment, and remained constant before the honeycomb core pressure began to decrease. This non-Darcian behaviour of the skins occurred because no continuous channels existed within the skin at this time in the vacuum hold.

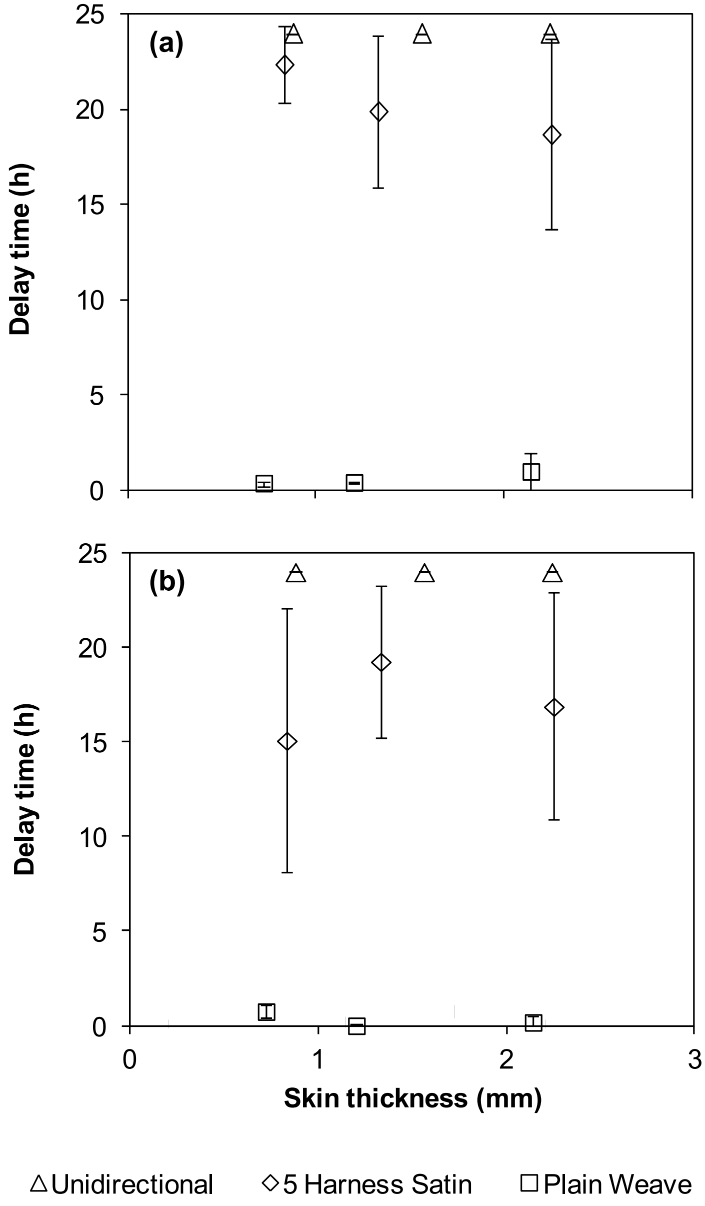

Figure 4.6. Average (symbols) and standard deviation (error bars) of the delay time before the honeycomb core pressure decreased: (a) transverse and (b) in-plane.

As consolidation pressure is applied by the vacuum bag, resin may flow into open pores, constricting channels in the prepreg until enough time has passed for the air pressure gradient to overcome the resin and form new flow channels within the skin. The average delay time was under 1 h for the plain weave fibre architecture in both the transverse and in-plane breathing directions. On the other hand, the average delay time for the lower crimp 5 harness satin fibre architecture was usually above 10 h, one of the few exceptions is shown in Figure 4.5. The average delay time for the 5 harness satin prepreg is higher than the plain weave, and the 5 harness satin exhibited more considerably more variability. Some samples prevented core evacuation from proceeding. If the material was held under vacuum for longer, air evacuation may have started. The higher variability and instances with limited air evacuation could lead to high part-to-part variability with the 5 harness satin prepreg in production. The unidirectional prepreg was consistent more consistent; unfortunately entrapped air could not escape the core during the 24 h vacuum hold with the unidirectional prepreg.

4.2.3.2 Determination of effective air permeability for honeycomb skins

The effective transverse and in-plane air permeability coefficients for honeycomb skins are shown in Figure 4.7 for the plain weave and 5 harness satin prepregs. No air permeability was detected for the unidirectional prepreg since no entrapped air escaped the core in either the in-plane or transverse breathing configurations.

The measurable effective transverse air permeability was $1.6 \pm 0.9 \times 10^{-17}$ m^2 and in-plane air permeability was $8.5 \pm 2.4 \times 10^{-15}$ m^2 for the 5 harness satin, over the thickness range tested. The plain weave fabric was the most permeable, with an effective transverse air permeability of $6.4 \pm 1.4 \times 10^{-17}$ m^2, and in-plane air permeability of $7.3 \pm 3.5 \times 10^{-15}$ m^2.

The micro-CT images (see Figure 4.2) revealed that the higher crimp plain weave fabric has aligned macro-porosity networks consisting of both tow cross-overs and inter-tow spaces that remained aligned with an increasing number of plies. In contrast, the lower crimp 5 harness satin fabric and flat unidirectional prepreg do not have aligned networks, and as a result, the air must follow a more tortuous path to escape the honeycomb core. The uniform layer of resin impregnated into the thin, flat unidirectional layers, produced no visible conduits in the micro-CT images, and therefore precluded air permeability measurements for skins with that material.

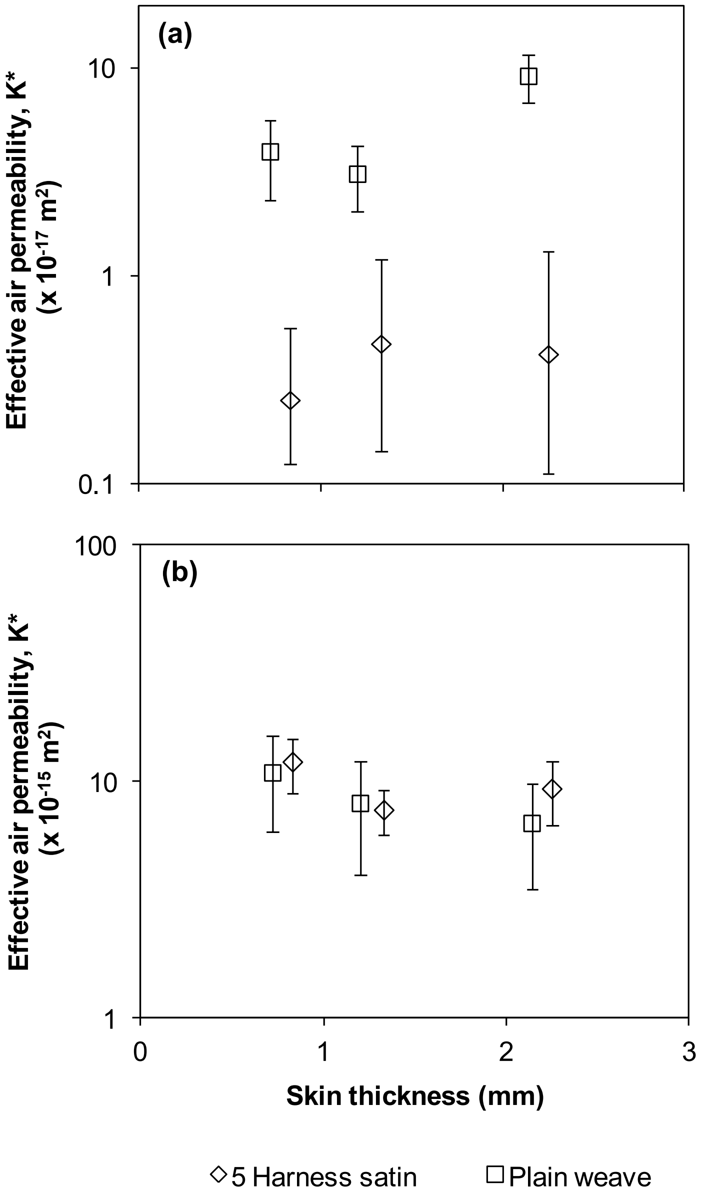

Figure 4.7. Average (symbols) and standard deviation (error bars) of the effective air permeability coefficients for the unidirectional, 5 harness satin, and plain weave skins: (a) transverse and (b) in-plane. The unidirectional prepreg showed no measureable air permeability for honeycomb processing.

The effective in-plane air permeability coefficients are alike for the plain weave and 5 harness satin skins, as shown in Figure 4.7. A slight reduction in the average air permeability was observed for increasing thickness in both materials, however, the overlap of the error bars indicate that effective honeycomb skin air permeability is more of a range than a specific value. The range of in-plane air permeability measurements are two orders of magnitude larger than the range of transverse air permeability measurements, supporting the findings in the literature [37-39]. If the visible dry tow area of the prepreg was lower, the effective in-plane air permeability would most likely decrease. Lower dry tow areas could arise during lay-up if a combination of heat and pressure are needed to make the prepreg conform to a mold with complex features. If the vacuum hold was performed with higher consolidation pressure than vacuum, such as in an autoclave with positive pressure, the degree-of-impregnation may increase, causing the air permeability to decrease.

The extent of anisotropy between the transverse and in-plane air permeability is shown in Figure 4.8. The permeability bounds are extracted as the average and ± one standard deviation from Figure 4.7. The plain weave fabric had effective transverse air permeability values an order of magnitude higher than the 5 harness satin. Although the 5 harness satin skins in this study feature more macro-porosity than the plain weave skins, the 5 harness satin transverse air permeability was lower because small pores restricted air flow through the skin. Part of the flow restriction comes from the weave pattern. Although the 5 harness satin skins have more macro-pores (Table 4.3) it has fewer interlacements between the tows than plain weave (Figure 4.8), and as a result, the plain weave has more pores available for transverse flow.

The compensation needed for anisotropic materials is shown in Figure 4.8. The uncompensated and effective air permeability of the plain weave prepreg is within the same order of magnitude, however, since the anisotropy is higher in the 5 harness satin prepreg, the air permeability measurement error would have been an order of magnitude without using the compensation presented in Eq. (3.20). The uncompensated values are lower than the effective permeability coefficients. Since these values could be used to predict pre-processing vacuum hold times, the parts would be held under vacuum for a longer period than needed. This may have negligible effect on part quality, but this would increase the length of the production cycle.

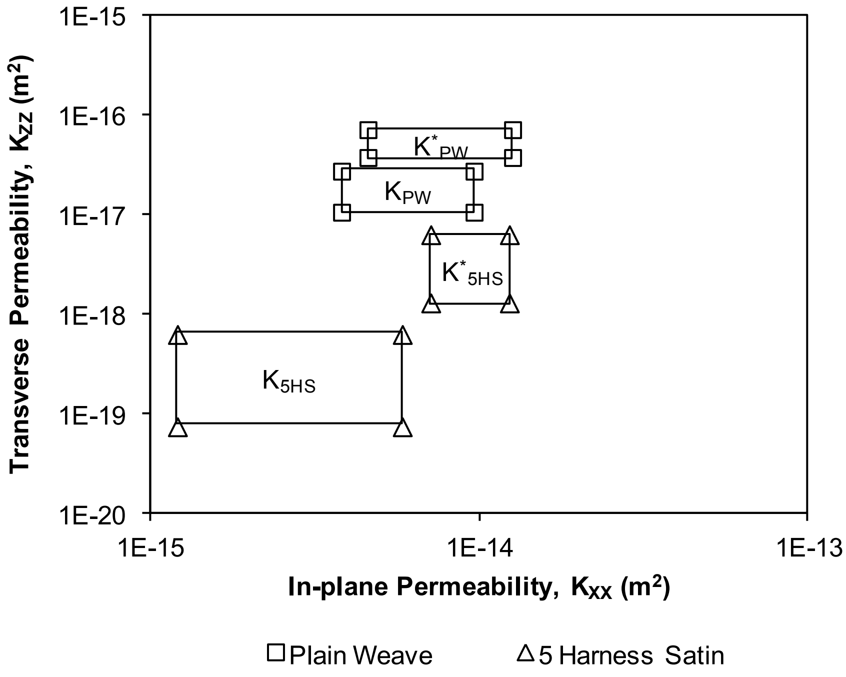

Figure 4.8. In-plane and transverse air permeability coefficients. Comparison of uncompensated permeability, K, calculated using Eq. (3.11), and effective permeability, K^* calculated using Eq. (3.20).

4.2.3.3 Lowest observed pressure

The final data extracted from each permeability test was the lowest observed pressure – the honeycomb core pressure after the 24 h vacuum hold. The results are shown in Figure 4.9. Both the transverse and in-plane breathing strategies had similar observed pressure trends after the 24 h vacuum hold, however, the different fabrics had a polarized behaviour. The plain weave had the lowest observed pressure between 131 and 272 mbar, the 5 harness satin was higher between 466 and 885 mbar, and the unidirectional material was the highest between 872 and 1015 mbar.

Core pressures between 400–700 mbar have been observed to reduce adhesive foaming and improve skin-to-core adhesion during cure [13], but cores pressures nearing atmospheric pressure during cure can lead to reduced skin-to-core adhesion [12,13] and high porosity [12]. The variation in core pressure at the end of the vacuum hold could lead to inconsistent cured panel quality for the different skin materials.

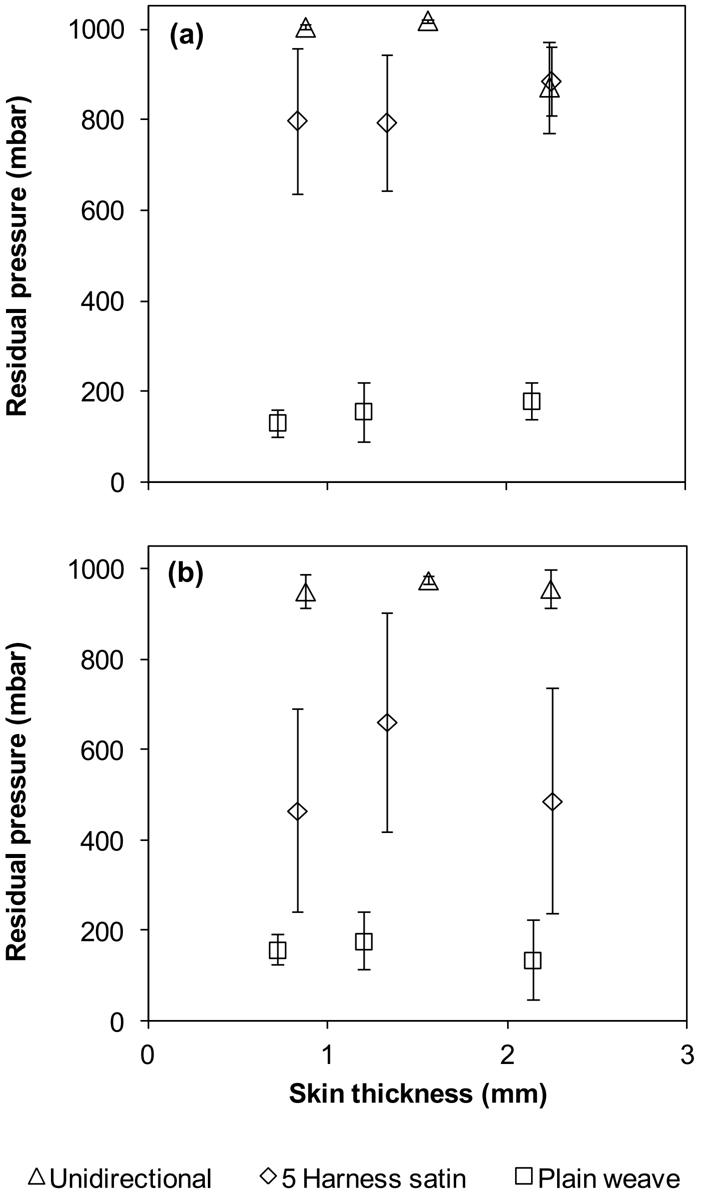

Figure 4.9. Average (symbols) and standard deviation (error bars) of the lowest observed honeycomb core pressure after the 24 h vacuum hold: (a) transverse and (b) in-plane.

4.2.4 Discussion of results during the vacuum hold prior to cure

The experiments performed during the pre-cure vacuum hold highlight the non-Darcian behaviour of gas flow in OOA prepregs. At first glance, the prepregs have similar porosity, but extreme behaviour in honeycomb core pressure was observed through experimental characterization. The plain weave skins demonstrated a consistent behaviour in delay time, effective air permeability and final observed pressure (see Figure 4.6 to Figure 4.9), whereas the 5 harness satin skins were erratic, and the unidirectional skins were impermeable.

All OOA prepregs studied have void spaces, however, not all prepregs may be suitable for honeycomb processing in their as received condition. A continuous network is required through the skin for entrapped air to escape the honeycomb core. In practice, it is probably impossible to align the pores between tows to create a network of channels, but the material can be altered to increase air permeability. *Tavares et al.* [15] increased the air permeability of unidirectional honeycomb skins from 1–20 x 10^{-20} m^2 to 2 x 10^{-18} m^2 by spiking individual layers. When they spiked the complete skin, the air permeability increased to 3 x 10^{-15} m^2. These results imply that aligned porosity networks will provide higher transverse skin air permeabilities than unaligned networks.

4.2.4.1 Material selection

Interconnected porosity in the flow direction should be considered when selecting a material for VBO processing. The simple experiments used in this study can identify if incoming prepregs are suitable for honeycomb processing, and by calculating the effective permeability, one can predict the duration of the vacuum hold needed to evacuate the core. Between the unidirectional, plain weave, and 5 harness satin prepregs studied in this work, the plain weave provides the best balance of transverse and in-plane honeycomb skin air permeability. As a result, a 4-ply plain weave skin will be used for the remainder of the thesis work.

If higher performance fabrics, such as unidirectional or 5 harness satin, are desired for honeycomb skins, their placement in the honeycomb skin stacking sequence should be where air flow is less critical. For example, plain weave layers should be placed adjacent to the adhesive film, and an in-plane breathing strategy should be used in-order for the plain weave prepreg to evacuate entrapped air from the core.

4.2.4.2 Air evacuation direction

Selecting the preferred flow direction will depend on the size of the part being manufactured, skin thickness, and both the transverse and in-plane air permeability coefficients. The dominant flow direction can be identified from the steady-state continuity equation:

$$\nabla \cdot \left(\rho \bar{v}\right) = 0 \tag{4.4}$$

where the momentum is described by Darcy's law:

$$\bar{v} = \frac{\bar{\bar{K}}}{\mu}\overline{\nabla P}\,. \tag{4.5}$$

If the change in density, ρ, is assumed to be proportional to the change in pressure, P, and substituting Eq. (4.5) into Eq. (4.4) yields the following governing expression for air flow through the prepreg skin:

$$\nabla \cdot \left(P\frac{\bar{\bar{K}}}{\mu}\overline{\nabla P} \right) = 0\,. \tag{4.6}$$

Expanding Eq. (4.6) yields the following non-linear expression for pressure within a prepreg:

$$\frac{\partial}{\partial x}\left(P\frac{K_{xx}}{\mu}\frac{\partial P}{\partial x} \right) + \frac{\partial}{\partial z}\left(P\frac{K_{zz}}{\mu}\frac{\partial P}{\partial z} \right) = 0\,. \tag{4.7}$$

Eq. (4.7) can be solved numerically to identify the pressure gradient within a honeycomb panel; however, the pressure gradient can be approximated as:

$$K_{xx}\frac{P^2}{\delta x^2} + K_{zz}\frac{P^2}{\delta z^2} = 0\,, \tag{4.8}$$

and a non-dimensional parameter, Ω, can be introduced to relate the transverse and in-plane air permeability to the skin thickness, h, and panel length, L, in-order to identify which flow direction dominates:

$$\Omega = \frac{K_{xx}}{K_{zz}}\left(\frac{h}{L}\right)^2\,. \tag{4.9}$$

The influence of prepreg anisotropy on Ω is plotted as a function of the thickness to length aspect ratio in Figure 4.10. For an isotropic material, $K_{xx}/K_{zz} = 1$, transverse flow dominates planar flow because of the length scale. As anisotropy increases, planar evacuation may be more effective for some part sizes. For the plain weave prepreg, where $K_{xx}/K_{zz} \approx 100$, transverse flow predominates in 1 mm thick panels larger than 90 mm × 90 mm. Given that the intended application of VBO panels is much larger than this, transverse flow will be used for the remainder of this thesis work.

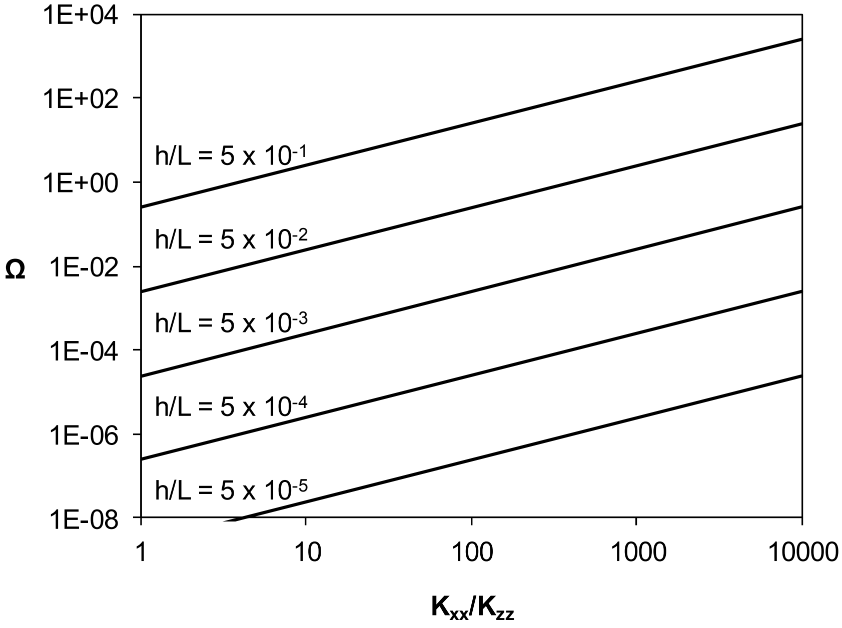

Figure 4.10. Predominant flow direction in out-of-autoclave prepregs as anisotropy increases for different aspect ratios. If Ω << 1, transverse flow dominates.

4.3 Skin behaviour during elevated temperature processing

Once elevated temperature processing begins, resin viscosity will decrease to fully impregnate the remaining dry fibre regions before cross-linking causes the resin to gel, and eventually a glassy solid. At gelation, any remaining voids are locked into the skin, and it is therefore very important to understand how the air permeability evolves during cure. During elevated temperature processing, entrapped gasses will pressurize and must escape the core through the skin to avoid disbonds. The following sections present the air permeability characterization of a 4-ply prepreg skin during elevated temperature processing.

4.3.1 Cure cycle definition

All elevated temperature processing was performed in an atmospheric pressure Blue M 1406 convection oven. The cure cycle was adapted from the material supplier's data sheet. Cytec recommends two cure cycles for Cycom® 5320, and they are summarized in Table 4.4. Cure cycle A offers a shorter cycle time, and therefore would most likely be preferred for production. The higher cure temperature in Cycle A would likely increase the honeycomb core pressure higher than Cycle B. For similar lay-up conditions, Cycle B would most likely produce honeycomb panels with fewer defects.

Table 4.4. Material supplier's recommended cure cycles for Cycom® 5320 [58].

Cure cycle	Ramp rate (°C/min)	Cure temperature (°C)	Soak time (h)
A	0.6–2.8	121 ± 6	2
B	0.6–2.8	93 ± 6	8

In order to investigate a more relevant and challenging problem, a modified version of cure cycle A was used. From the manufacturer's data sheet, the median 1.7 °C/min temperature ramp rate and the higher 121 °C cure temperature were chosen for all elevated temperature processing. The soak time was extended from 2 to 4 h in order to characterize the core pressure evolution through resin gelation. The temperature of the bag-side honeycomb skin was recorded using a K–type thermocouple embedded in the skin. The skin temperature for cure cycle A is shown in Figure 4.11, and the viscosity behaviour of the resin and adhesive film are plotted alongside temperature to show key process parameters, such as minimum viscosity and gelation. The viscosity models for the resin and adhesive are developed in Appendix A.

The adhesive and resin are both thermoset polymers, but have different cure and viscosity behaviour during cure (Figure 4.11). Both materials decrease in viscosity as the temperature rises, however the adhesive viscosity remains significantly higher than the resin viscosity throughout the cure cycle. The resin reaches minimum viscosity at the same time as the adhesive gels, which occurs an hour before the resin gels.

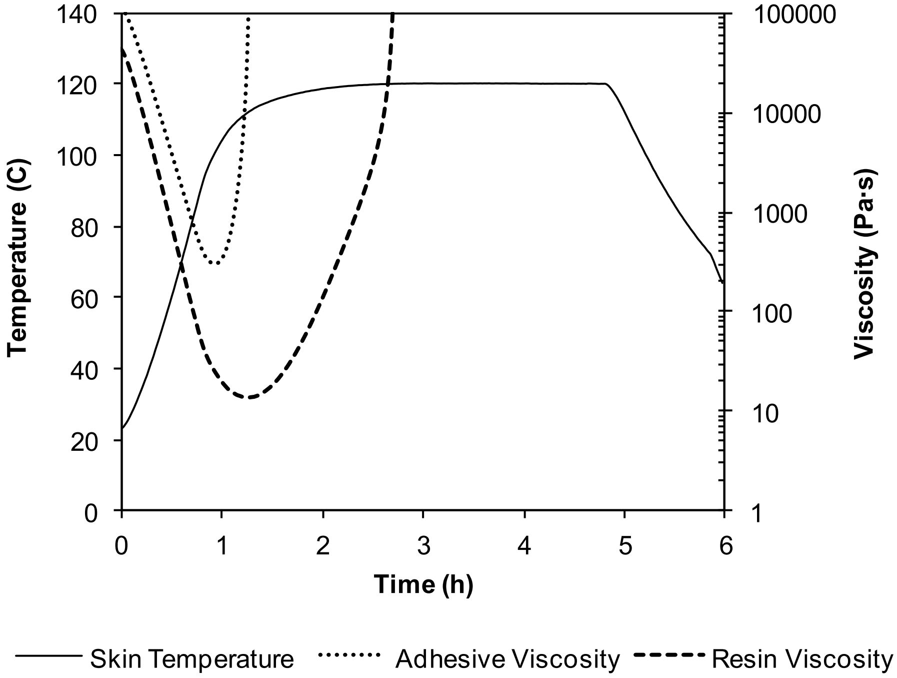

Figure 4.11. Cure cycle showing the measured skin temperature during oven cure and the viscosity profile of the adhesive film and epoxy resin.

4.3.1.1 A stepwise temperature profile to characterize skins during cure

During elevated temperature processing, the ply thickness decreases as the dry fibre areas are impregnated during processing [41]. Any thickness change during processing presents some challenges for permeability measurements because Darcy's law requires constant thickness for the porous medium. For this reason, a stepwise temperature profile was developed to characterize the permeability at constant temperature, when limited changes in viscosity, and therefore, limited changes in thickness would occur.

The stepwise temperature profile of the skin is shown in Figure 4.12a. The first air permeability measurement occurred during the vacuum hold prior to cure at time *t* = –16 h. When the vacuum pump was started, the pressure would decrease shown in Figure 4.4. The second air permeability measurement was taken 30 minutes prior to elevated temperature processing to assess the decrease in air permeability caused by the vacuum hold. The temperature was increased in 20 °C intervals up to 100 °C. The temperature was increased as quickly as possible between steps by setting the oven controller to the target temperature. A period of one hour was required for the skin temperature to reach equilibrium (within 1 °C) with the oven temperature. The number of stepwise temperature repetitions is summarized in Table 4.5. The last stepwise permeability measurement was taken at 100 °C because the adhesive had gelled and the resin was beginning to gel. As a result, a separate series of single-step permeability experiments were performed at 121 °C to identify the air permeability at that processing temperature. The timing of the permeability measurements at 121 °C is shown in Figure 4.12b, and these tests were repeated 5 times. The X marks in Figure 4.12 show the location where the permeability was measured and where some tests were interrupted to freeze the microstructure for micro-CT analysis.

The stepwise temperature increments afforded to opportunity to interrupt some experiments at a constant temperature to examine the micro-structure of the skin at the same moment when a permeability measurement would be performed. Micro-CT imaging was used to identify the status of the pore space within the skin, and the thickness of the skin. The skin could be compared to tow impregnation models, in-order to evaluate whether the stepwise temperature increments reduced the pore space differently than a constant temperature ramp, which would be used in the manufacturing process of actual panels. Furthermore, the thickness of the skin could was measured at the time when a permeability measurement was performed. The skin thickness is summarized in Table 4.5.

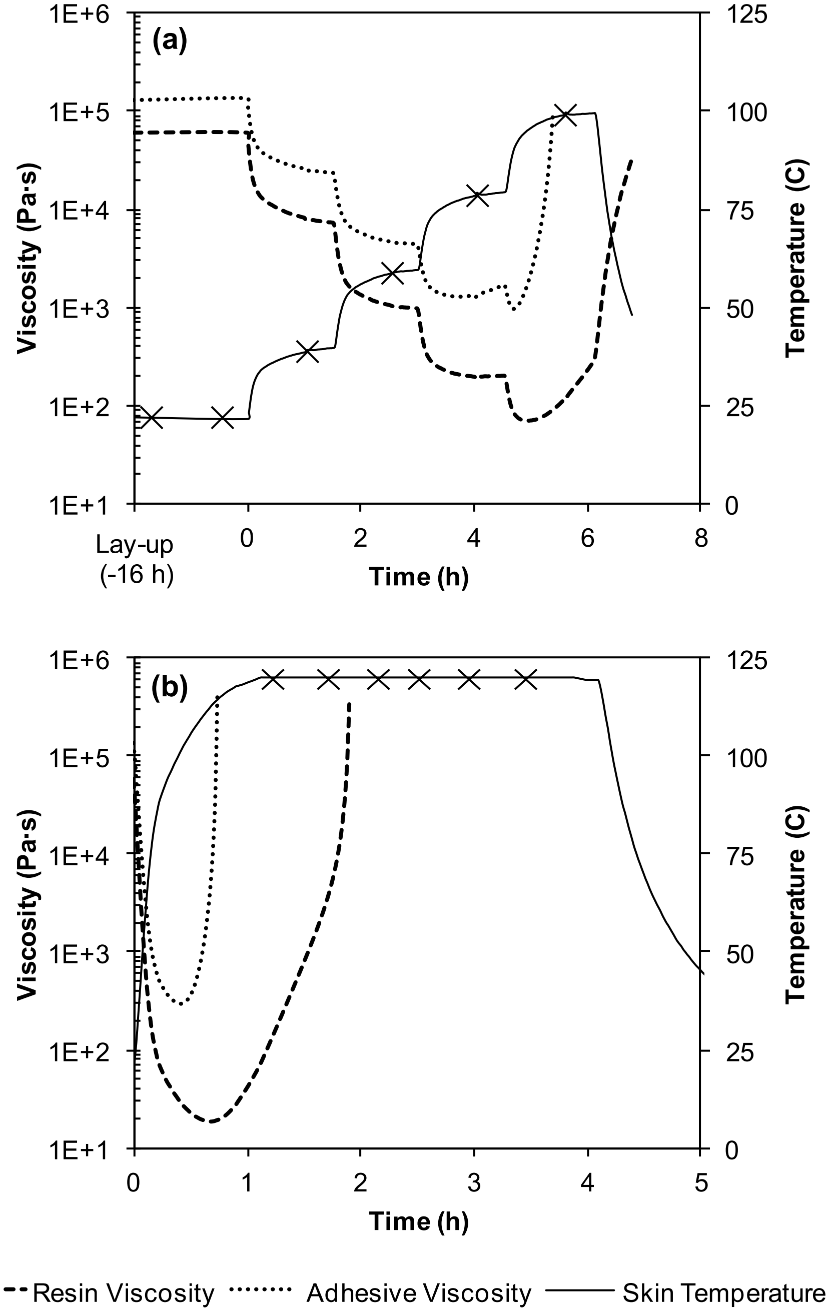

Figure 4.12. Elevated temperature permeability measurements: (a) step-wise permeability measurements up to 100 °C and (b) single-step permeability measurements at 121 °C. The X marks indicate a measurement location.

Table 4.5. Test matrix for stepwise permeability measurements.

Permeability measurement	Temperature (°C)	Skin thickness (mm)	No. repeats	Micro-CT image in Figure 4.13
1	22 ± 2	1.28	12	(a)
2	22 ± 2	1.25	11	(b)
3	40 ± 1	1.25	10	(c)
4	60 ± 1	1.20	9	(d)
5	80 ± 1	1.08	8	(e)
6	100 ± 1	1.05	7	(f)

4.3.2 Micro-CT imaging of honeycomb skins during co-cure

A total of six prepreg samples were scanned and analyzed using the procedures outlined in section 4.2.1. A sample was scanned for each stepwise permeability measurement in Table 4.5. The first sample was taken 1 h into the vacuum hold, and the remaining five were taken at the points shown in Figure 4.12a.

To collect samples at elevated temperature, the fixture was removed from the oven and cooled using a fan, while a cold (–10 °C) block of aluminum was placed on top of the vacuum bag. The skin temperature, measured by an embedded thermocouple, dropped to below ambient within 2 to 3 minutes, limiting any further resin flow. Once the fixture had cooled to room temperature, the vacuum bag was vented, the test sample removed, and an 18 mm × 18 mm sample was cut from the centre, and stored in a freezer until it was scanned.

Representative micro-CT slices of the honeycomb skin are shown in Figure 4.13 for each permeability measurement. Each image shows four prepreg plies, a layer of adhesive, and a portion of honeycomb core. The scans show the resin saturated regions (pale grey), the dry fibre tows (dark ellipses), entrapped volatiles or macro-voids (black regions), and the adhesive film (bright areas). The images show the evolution of the skin pore space as vacuum pressure and temperature are applied to the skin. The air evacuation is indicated by the decrease in visible macro-voids entrapped between plies, while the progressive tow impregnation is seen through the decrease in visible dry fibre tow areas. Entrapped air present after 1 h of vacuum (Figure 4.13a) is mostly gone after 16 h (Figure 4.13b) and completely gone at 40 °C (Figure 4.13c). The dry fibre tows are clearly visible until 60 °C, the adhesive film begins to form fillets at the skin-to-core interface and flow into the skin at 60 °C (Figure 4.13d). Tow saturation varies between 75 and 100 % and the adhesive forms fillets at 80 °C (Figure 4.13e). The fibre tows are fully saturated at 100 °C (Figure 4.13f).

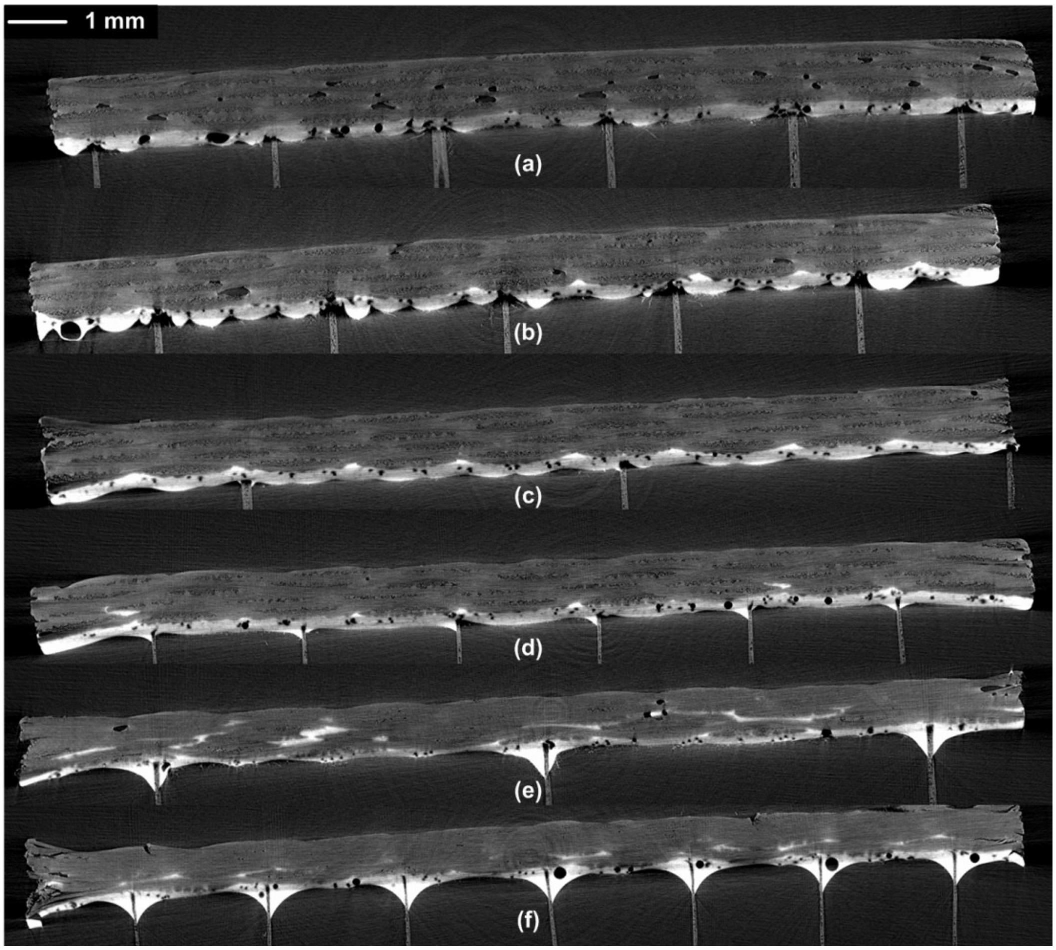

Figure 4.13. Micro-CT slices at 7 μm/pixel of the honeycomb skin for each permeability measurement in Figure 4.12a: (a) 1 h into vacuum hold, (b) 16 h into vacuum hold, (c) 40 °C , (d) 60 °C, (e) 80 °C, and (f) 100 °C.

As elevated temperature processing progressed, the void space reduced and some of the adhesive film migrated into the skin during the permeability measurements, as observed in Figure 4.13d–f. The adhesive appears to be located around the fibre tows, not within the tows. Without any definitive method to trace the flow of gas through the skin during elevated temperature processing, the location of the adhesive film in the cured skins may provide some insight into the path escaping gas follows.

The adhesive is unlikely to flow into the skin on its own accord because the viscosity of the adhesive is always higher than the resin throughout processing. The flow of gas through the skin during the permeability measurements could have forced the adhesive between the fibre tows. Observing the final location of the adhesive within the skin does not identify all air paths available, but does show that the highest viscosity fluid in the honeycomb skin was displaced from the skin-to-core interface, suggesting that some gas escaping the core flowed around the tows that were being impregnated by resin.

The percentage of adhesive film within the skin was measured directly using the 3D analysis feature of Skyscan's CTAn software. The results are presented in Figure 4.14. After the vacuum hold prior to cure, the increase in adhesive in the skin is due to the variable interface between the prepreg and adhesive. At the skin-adhesive interface, adhesive can flow between the elliptical tows. The boundary of the skin was defined as the centre of the tows in the prepreg ply adjacent to the adhesive. Therefore, an increase in adhesive was measured after more adhesive was compressed in between the tows during the 16 h vacuum hold. The adhesive viscosity was sufficiently high to prevent displacement into the skin as elevated temperature processing began. However, the adhesive content within the skin doubled at 80 °C and remained constant up to 100 °C. These observations suggest that the adhesive is more likely to be displaced if flow occurs through the honeycombs skins at the higher processing temperatures. No error bars are included in Figure 4.14 because the adhesive content was measured for only one sample.

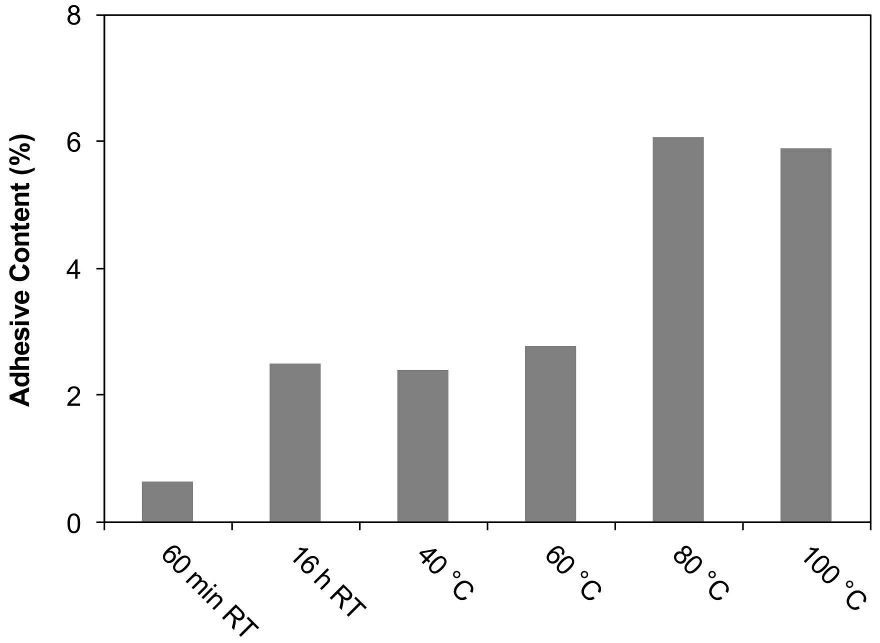

Figure 4.14. Adhesive content in honeycomb skin during stepwise permeability measurements.

The measured degree-of-impregnation at each stepwise air permeability measurement was compared to the predicted degree-of-impregnation in Figure 4.15 for the cure cycle shown in Figure 4.11. The predicted degree-of-impregnation was calculated using the model presented by *Centea and Hubert* [41] for the same Cycom® 5320 plain weave prepreg material used in this study. The measured and predicted values of degree-of-impregnation agree, confirming that using stepwise permeability measurements was a reasonable approach to measure the air permeability during the ramp without altering the prepreg micro-structure. This proved to be a convenient method to simulate a dynamic temperature ramp in-order to characterize the air permeability at constant skin thickness.

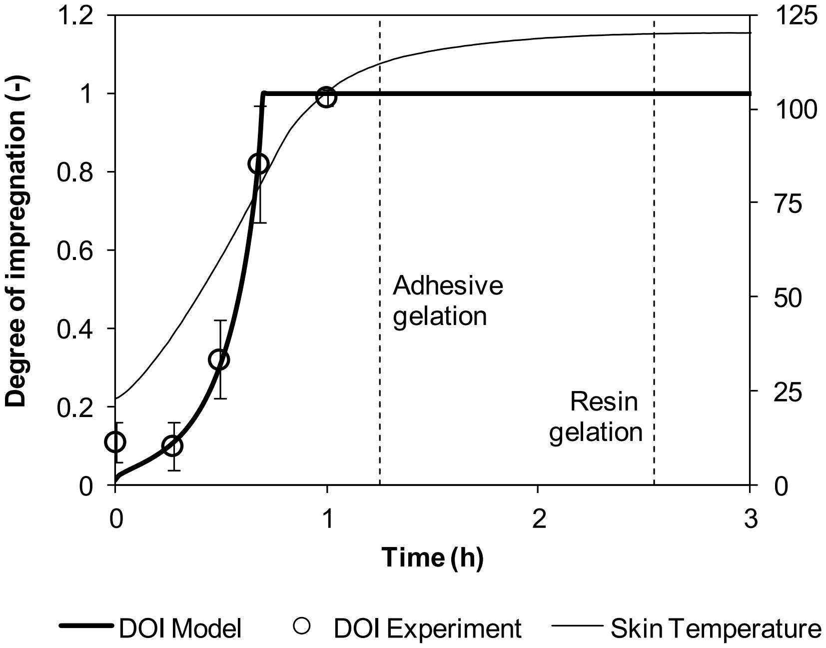

Figure 4.15. Cure cycle showing the measured skin temperature profile and degree of impregnation of the dry fibre tows during cure. The stepwise permeability experiments produce a skin architecture equivalent to a temperature ramp of 1.7 °C/min.

4.3.3 Air permeability of honeycomb skins during co-cure

The transverse air permeability was measured using the experimental set-up shown in Figure 3.1. An initial value of air permeability was calculated from the pressure drop during the vacuum hold prior to cure. To identify any changes in air permeability during the vacuum hold, a second room temperature permeability measurement was performed 30 minutes before the elevated temperature processing measurements, as shown in Figure 4.16.

The honeycomb core pressure had decreased towards the vacuum bag pressure after the initial vacuum hold prior to cure in Figure 4.16. As a result, air was introduced into the cavity to enable subsequent permeability measurements. *Tavares et al.* [15,19] introduced air into the core to at two pressure levels, and they reported higher air permeability coefficients for higher core pressure levels. In this study, air pressures of 500 mbar were introduced to the honeycomb core side of the skin to make subsequent measurements after the initial vacuum hold.

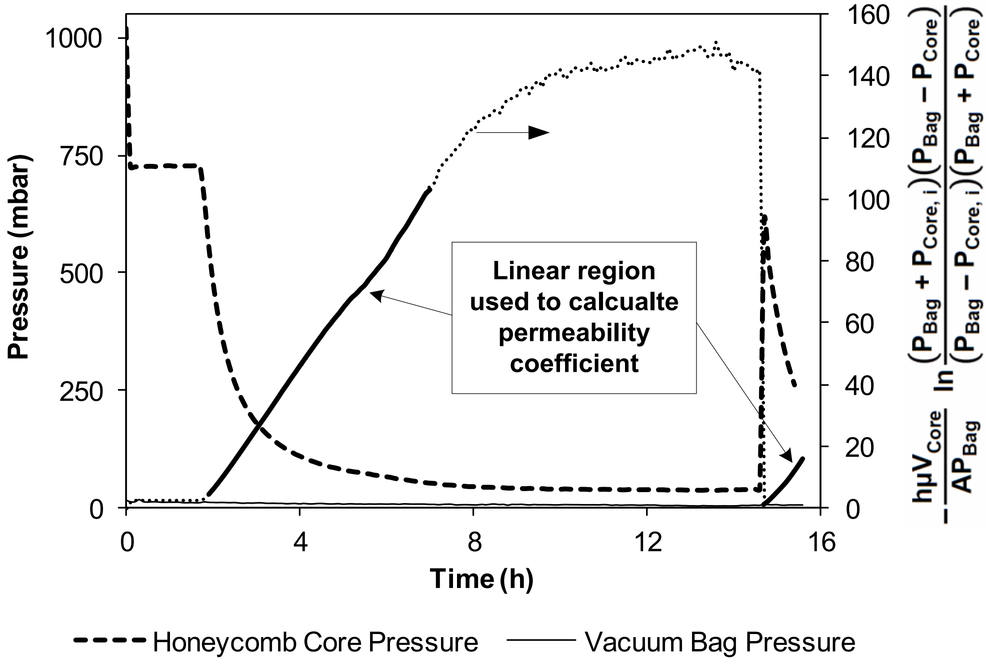

Figure 4.16. An example of repeated air permeability measurement on the same sample at room temperature. The first measurement simulates the vacuum hold prior to cure.

The permeability measurements during processing are plotted in Figure 4.17 alongside the skin temperature profile during processing. These measurements follow the trend observed in liquid composite molding, where variability is commonplace in permeability measurements for the same perform in the same lab [85]. All air permeability measurements (from Figure 4.12) are plotted alongside the average value. Linear interpolation between experimental data points was used to estimate the air permeability values for this specific honeycomb skin, bagging arrangement, and cure cycle. The air permeability function can now be used as an input for process models to predict honeycomb core pressure during cure.

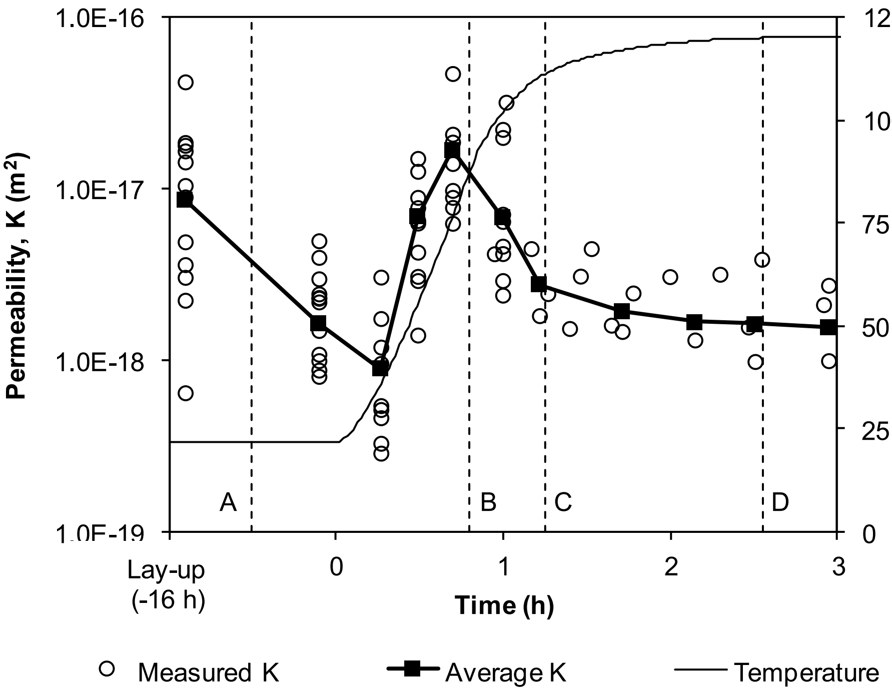

Figure 4.17. Evolution of skin air permeability during cure. All experimental data is shown and the average air permeability for each measurement. Key boundaries in the cure cycle are shown: A – end of the pre-cure vacuum hold at time t = -0.5 h, B – the dry tows are saturated, C – the adhesive film gels, and D – the resin gels. Each symbol represents a permeability measurement.

4.3.4 Discussion of air permeability results during processing

A decrease in air permeability was observed after the vacuum hold prior to cure. The skin was consolidated through a combination of fibre re-arrangement and resin flow into the void spaces around the tows. The entrapped air within the core encountered more resistance to flow after the vacuum hold, and accordingly, the transverse air permeability was lower.

As the temperature was increased to 40 °C, the viscosities decreased by an order of magnitude, but no discernible decrease in sample dry tow area was measured in the micro-CT images. Nevertheless, a decrease in transverse air permeability was observed. A similar behaviour was observed by *Tavares et al.* [15,19], and they propose that the reduction in air permeability was caused by the resin filling small air paths. The measured data in the current study supports their view. Since the viscosities decrease and all other skin properties remain constant, the resin and adhesive become tackier, but sufficiently stiff that the escaping gas cannot form a flow channel through the skin for the air to escape the honeycomb core at 40 °C.

At 60 °C, the resin and adhesive viscosities decreased again, by roughly an order of magnitude. The resin viscosity was sufficiently low for noticeable flow to occur since an increase in tow impregnation was observed. Even though the skin micro-porosity decreased, the air permeability increased. This was observed again at 80 °C. The resin and adhesive viscosities dropped, causing the largest rise in tow impregnation and transverse air permeability. A similar increase in air permeability was observed by *Tavares et al.* [15,19] as the temperature was increased. They suggested that the increase in air permeability was caused by the mobility of low viscosity resin at higher temperatures. At low viscosity, the resin is in a favourable condition to allow flow channels to form through the skin, enabling higher air permeability. This was confirmed at 100 and 121 °C, where the transverse air permeability decreased because tow impregnation was complete, the adhesive had gelled, and the resin viscosity was increasing. At elevated temperatures, the air permeability increased, even though tow impregnation increased, because the resin viscosity enabled gas to flow more easily.

The elevated temperature air permeability measurements signify that the least resistance to flow through the honeycomb skin will occur near 80 °C. A devolatilization dwell could be introduced near 80 °C to reduce the honeycomb core pressure before the onset of resin and adhesive gelation. The resin will be in a high mobility state, affording time to evacuate entrapped gasses before they are locked into the skin as voids.

4.4 Summary

The effective air permeability was measured during the vacuum hold prior to cure for three out-of-autoclave prepreg honeycomb skins: unidirectional, plain weave, and 5 harness satin. The pore space in the plain weave prepreg offered the most consistent, predictable, air permeability results. Transverse breathing was identified as the predominate flow direction for entrapped air to escape the honeycomb core in large panels. In light of these results, the plain weave prepreg was chosen as the skin material, and transverse breathing was chosen as the flow direction for this study.

A stepwise temperature profile was developed to measure the honeycomb skin transverse air permeability during elevated temperature processing. Micro-CT images were also taken of the skin during processing to measure skin thickness and understand the evolution of the pore space. These results will be used in the following chapters to develop and validate process models for honeycomb core pressure.

Chapter 5

Honeycomb Core Pressure Model

Consolidation pressure is needed during elevated temperature processing to suppress voids, compact the prepreg layers, and bond the skin to the core. Inconsistent part quality may arise if entrapped gases pressurize during cure and oppose the consolidation pressure. The objective of this chapter is to develop a model for honeycomb core pressure that links the manufacturing process parameters to the material properties. A control volume was applied to the honeycomb cell void space, and the pressure within the control volume was governed by the inflow of moisture from the honeycomb cell walls and the outflow of moist air through the honeycomb skin. After the model was validated with experiments, it was used to study the process parameters, and provide recommendations to minimize the risk of defects when manufacturing honeycomb panels.

5.1 Model development

The following sub-sections detail the control volume used to predict honeycomb core pressure during cure. The mass flow into the control volume was discretized to predict the inflow of moisture from the honeycomb cell walls using Fick’s law, and the outflow of moisture using Darcy’s law. The moisture diffusion coefficient was then determined for the honeycomb core. Finally, the model assumptions and limitations are discussed.

5.1.1 Control volume

The void space within a honeycomb cell is bounded by the paper walls, the bag-side skin, and the tool-side skin. A control volume was created with these boundaries to describe a repeating honeycomb cell, and a schematic is shown in Figure 5.1. Four paper walls absorb and release moisture into the control volume bounded by a permeable bag-side skin and an impermeable tool-side skin. The model predicts pressure based on the current mass of air and water vapor, m_{cell}, comprised of the influx of water vapor from the paper walls, $\dot{m}_{Honeycomb}$, and the outflow of moist air through the permeable bag-side skin, $\dot{m}_{Bag\ Side}$.

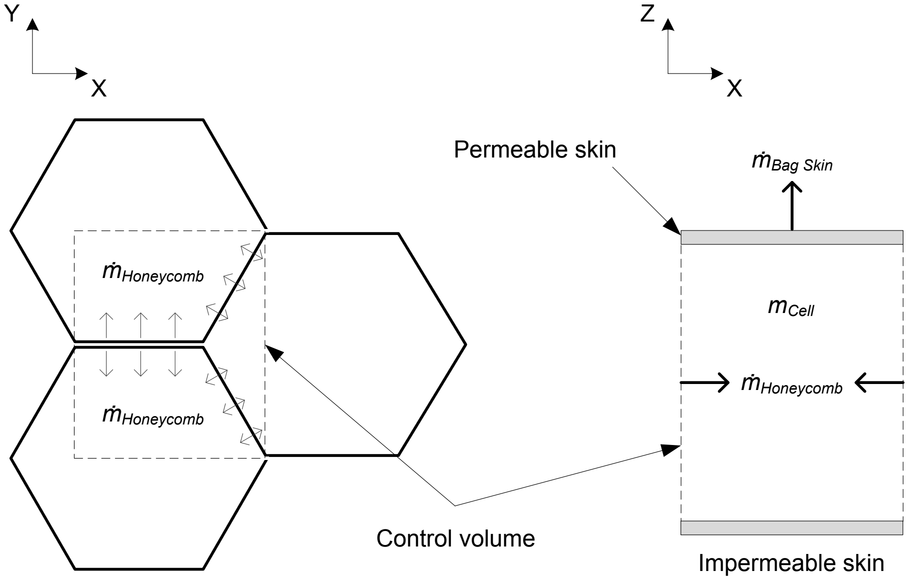

(a) (b)

Figure 5.1. Schematic of the honeycomb core: (a) repeating unit and, (b) control volume used for pressure modelling.

The evolution of the honeycomb core pressure within the control volume is both space and time dependant, and follows the conservation of mass:

$$-\nabla \cdot \left(\rho \bar{v}\right) = \frac{\partial \rho}{\partial t} \tag{5.1}$$

where ρ is the density of the gas and $\bar{v}$ is the velocity of the gas in the control volume (or honeycomb cell). Integrating Eq. (5.1) relates the amount of matter entering the control volume, V, through its boundaries:

$$-\iiint_V \nabla \cdot (\rho \bar{v}) dV = \iiint_V \frac{\partial \rho}{\partial t} dV \, . \tag{5.2}$$

Using the divergence theorem to transform the volume integral into a surface integral yields the following expression:

$$-\oiint_{Honeycomb} \rho \bar{v} \cdot \bar{n} \, dS - \oiint_{Bag\,Skin} \rho \bar{v} \cdot \bar{n} \, dS - \oiint_{ToolSkin} \rho \bar{v} \cdot \bar{n} \, dS = \frac{\partial}{\partial t} \left(\iiint_V \rho \, dV \right) \tag{5.3}$$

where the left hand side of Eq. (5.3) describes the outward fluxes of matter from the control volume (Figure 5.1b) through surface normals, $\bar{n}$. If we assume that, transverse gas flow through the bag-side skin dominates, the flux through the tool-side skin can be neglected, and all therefore outward flow is assumed to occur through the bag-side skin. Transforming the honeycomb flux to an inward flux and integrating relates the change in mass with time, $\dot{m}$:

$$\dot{m}_{Honeycomb} - \dot{m}_{Bag\,Skin} = \dot{m}_{Cell} \, . \tag{5.4}$$

To predict the honeycomb cell pressure, the mass in the honeycomb cell can be calculated by discretizing Eq. (5.4) over time step Δt:

$$\dot{m}_{Honeycomb} - \dot{m}_{Bag\,Skin} = \frac{m_{Cell,\, t+\Delta t} - m_{Cell,\, t}}{\Delta t} \, . \tag{5.5}$$

From Eq. (5.5), the change in mass in the honeycomb cell void space is controlled by the diffusion of moisture out of the honeycomb cell walls and the permeation of moist air through the bag-side skin.

The velocity of this flow is very low (see Reynold's number estimation in section 3.2.1), therefore the momentum equation was ignored. Since the effect of velocity on the pressure was neglected, the total pressure in the honeycomb core, P_{Core}, can be calculated at any time step, Δt, using the ideal gas law equation of state and by assuming that neither air nor water molecules are biased during outflow:

$$P_{Core} = \frac{R_u T}{V_{Core}} \left[\frac{m_{Air,i}}{\omega_{Air}} + \frac{\left(m_{Vapor} + \dot{m}_{Honeycomb}\, \Delta t \right)}{\omega_{Vapor}} - \dot{m}_{Bag\ Skin}\, \Delta t \left(\frac{\gamma_{Air}}{\omega_{Air}} + \frac{\gamma_{Vapor}}{\omega_{Vapor}} \right) \right] \tag{5.6}$$

where R_u is the universal gas constant, T is the temperature, V_{Core} is the empty volume of the honeycomb core, γ is the mass fraction of air and water vapor in the cell, and ω is the molar mass of air and water vapor.

The moisture exchange from the cell walls into the cell space and the gas permeation through the bag-side skin were decoupled and solved at 10 second time intervals during elevated temperature processing using the procedure shown in Figure 5.2.

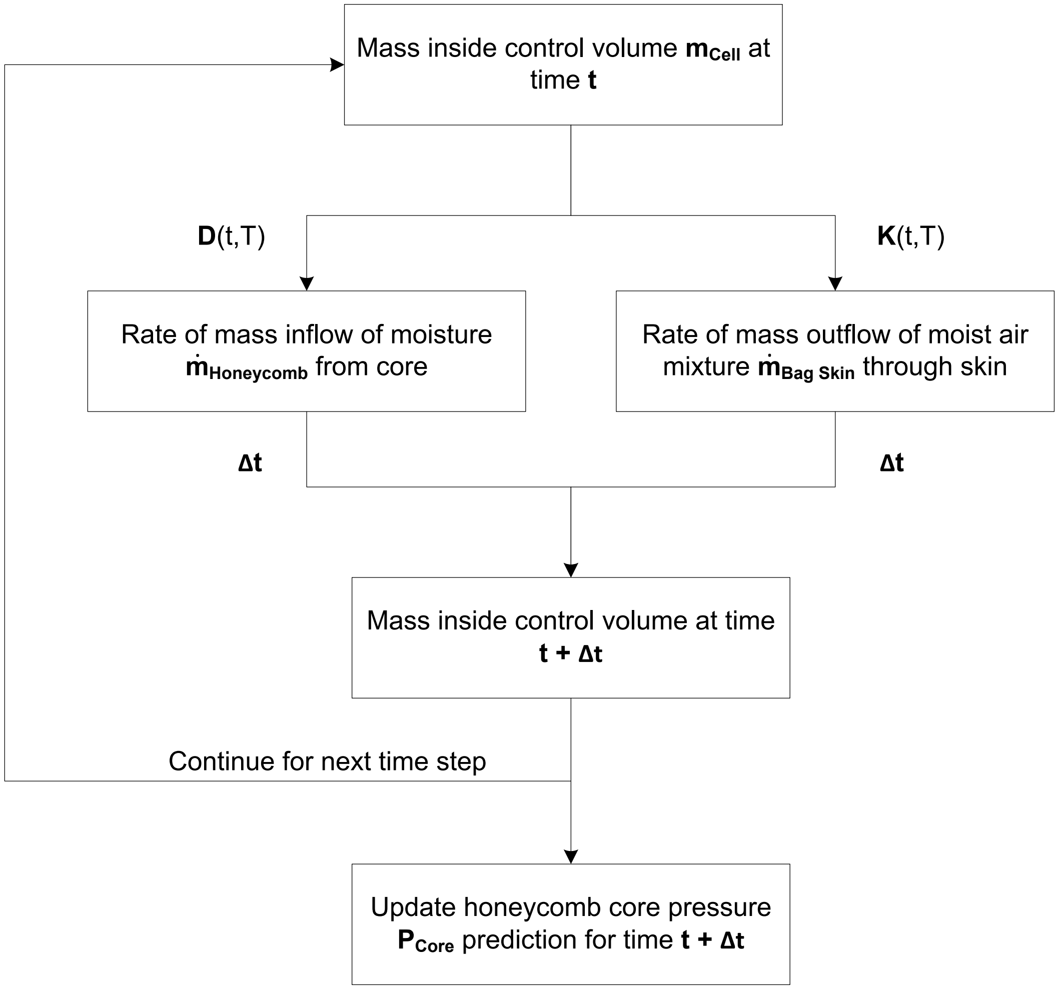

Figure 5.2. Flowchart of the approach used to model the honeycomb core mass and pressure during cure.

5.1.2 Mass outflow due to air permeability

The low air permeability coefficients of prepreg confine the gas flow through the skin to low Reynold's numbers, $Re << 10$. As a result, laminar flow of a compressible gas through a porous medium can be predicted by Eq. (3.7). Adapting the volumetric flow rate in Eq. (3.7) for mass flow rate through the bag-side skin, $\dot{m}_{Bag\ Skin}$, gives:

$$\dot{m}_{Bag\ Skin} = -\frac{\rho KA}{2\mu h}\frac{P_{Bag}^2 - P_{Cell}^2}{P_{Bag}} \tag{5.7}$$

where ρ is the density of the gas, which was assumed to be constant during each time-step.

The density of air and water vapor in the honeycomb cell void space were calculated directly:

$$\rho_{Air} = \frac{m_i}{V_{Cell}} \tag{5.8}$$

where m is the mass of substance i. The saturation pressure was needed to account for the initial mass of vapor in the cell volume from the relative humidity of entrapped air. The saturation pressure was calculated (in kPa) as a function of the temperature using the empirical Antoine Equation:

$$\ln P_{SAT} = A - \frac{B}{C+T} \tag{5.9}$$

where $A = 18.3036$, $B = 3816.44$, and $C = -46.13$ are the constants for water.

The viscosities of the gasses within the honeycomb cell were accounted for using Sutherland's law for air and water vapour as a function of temperature:

$$\mu(T) = \mu_0 \left(\frac{T}{T_0}\right)^{\frac{3}{2}} \left(\frac{T_0 + S}{T + S}\right) \tag{5.10}$$

where T is the temperature in Kelvin, S is the Sutherland constant ($S_{Air} = 111$ K and $S_{Vapour} = 961$ K), and T_0 and μ_0 are reference values. The semi-empirical formula proposed by *Wilke* [86] was used to calculate the viscosity of the mixture:

$$\mu_{mix} \approx \sum_{i=1}^{2} \frac{x_i \mu_i}{\sum_{j=1}^{2} x_j \phi_{ij}} \tag{5.11}$$

and

$$\phi_{ij} = \frac{\left[1 + \left(\mu_i / \mu_j\right)^{1/2} \left(\omega_j / \omega_i\right)^{1/4}\right]^2}{\left(8 + 8\,\omega_i / \omega_j\right)^{1/2}} \tag{5.12}$$

where ω is the molecular weights of mixture substances i (air) and j (water vapor).

5.1.3 Mass inflow due to moisture diffusion

The rate of mass diffusion within the individual components of a sandwich panel can be modelled using Fick's first law of diffusion:

$$J = -D\,\nabla c \tag{5.13}$$

where J is the moisture flux, D is the diffusion coefficient, and c is the concentration. Fick's second law of diffusion can be used to account for the change in moisture concentration with time:

$$\frac{\partial c}{\partial t} = D\,\nabla^2 c \tag{5.14}$$

by assuming the moisture concentration and diffusion coefficient are constant within a single time-step. The diffusion coefficient can be assumed to be unaffected by changes in ambient humidity with minimal error, however changes in temperature will strongly influence the diffusion coefficient [88]. The diffusion coefficient can be described by an Arrhenius relationship for changes in temperature, T:

$$D = D_0 \exp\left(\frac{-E_D}{R_u T}\right) \tag{5.15}$$

where D_0 is the pre-exponential factor, E_D is the activation energy, and R_u is the universal gas constant.

To simplify the analysis, researchers have used percent moisture content, M, instead of concentration, c, when modelling the moisture flow in composite materials [88–89]. As a result, Eq. (5.13) & (5.14) become:

$$J = -\frac{D\rho}{100}\frac{\partial M}{\partial x} \tag{5.16}$$

$$\frac{\partial M}{\partial t} = D\frac{\partial^2 M}{\partial x^2} \tag{5.17}$$

where the percent moisture content of a material can be described as:

$$M = \frac{m - m_D}{m_D} \times 100 \tag{5.18}$$

where m is the current mass and m_D is the dry mass of the material through which moisture is diffusing [88].

The conservation of mass between the interfaces of structures comprised of multiple materials requires the moisture leaving material A to enter material B [59]. Applying this to Eq. (5.16) results in:

$$D_A\rho_A\left(\frac{\partial M}{\partial x}\right)_A = D_B\rho_B\left(\frac{\partial M}{\partial x}\right)_B . \tag{5.19}$$

In the case of a material exposed to humid air, the moisture content can be described by [88]:

$$M = M_U H^{\xi} \tag{5.20}$$

where M_U is the percent moisture by mass at 100 % relative humidity, H is the relative humidity in percent, and ξ is a constant.

An experimental investigation into the diffusion coefficients for carbon-epoxy skins, epoxy adhesive, and Nomex core showed $b = 1$ for all materials [60]. Accordingly, the moisture level at the interface of the honeycomb paper walls and the cell void space can be described as:

$$M_{Paper}\, M_{U,Cell} = M_{Cell}\, M_{U,Paper} . \tag{5.21}$$

Combining Eq. (5.16) & (5.21) and including the area through which moisture flux occurs yields the following expression to describe the outflow of moisture from the honeycomb core walls into the core void space:

$$\dot{m}_{Honeycomb} = -D\rho A_S\left(\frac{M_{Paper}}{M_{U,\,Paper}} - \frac{M_{Cell}}{M_{U,\,Cell}}\right) \tag{5.22}$$

where A_S is the exposed surface area of the honeycomb cells. The mass flow of moisture from the paper walls into the honeycomb cell void space, $\dot{m}_{Honeycomb}$, can be predicted if the maximum and instantaneous moisture content of the paper walls is known and if the saturation pressure of water vapor can be calculated. The maximum and instantaneous moisture content of the paper walls is characterized in the following section. The saturation pressure of the water vapour can be calculated if the percent relative humidity is known, or can be assumed equal to the lay-up room conditions, at the start of elevated temperature processing.

5.1.4 Characterization of honeycomb core diffusion coefficient

The constants for the Arrhenius diffusion coefficients (D_O and E_D) were obtained by conditioning separate core samples at three moisture levels, and heating the moist samples in the cavity of the experimental set-up shown in Figure 3.1. A 6 mm thick aluminum plate was used instead of the composite skin. As a result, $\dot{m}_{Bag\ Skin} = 0$, therefore the only unknown term needed to predict P_{Core} in Eq. (5.6) was the diffusion coefficient. Curve fitting for the pre-exponential factor, D_O, and activation energy, E_D, in Eq. (5.15) solves for the diffusion coefficient in Eq. (5.22). The predicted honeycomb cell pressure is plotted alongside the measured pressure in Figure 5.3 using the curve-fit constants $D_O = 7.2 \times 10^{-1}$ m^2/s and $E_D = 3.8 \times 10^4$ kJ/kg.

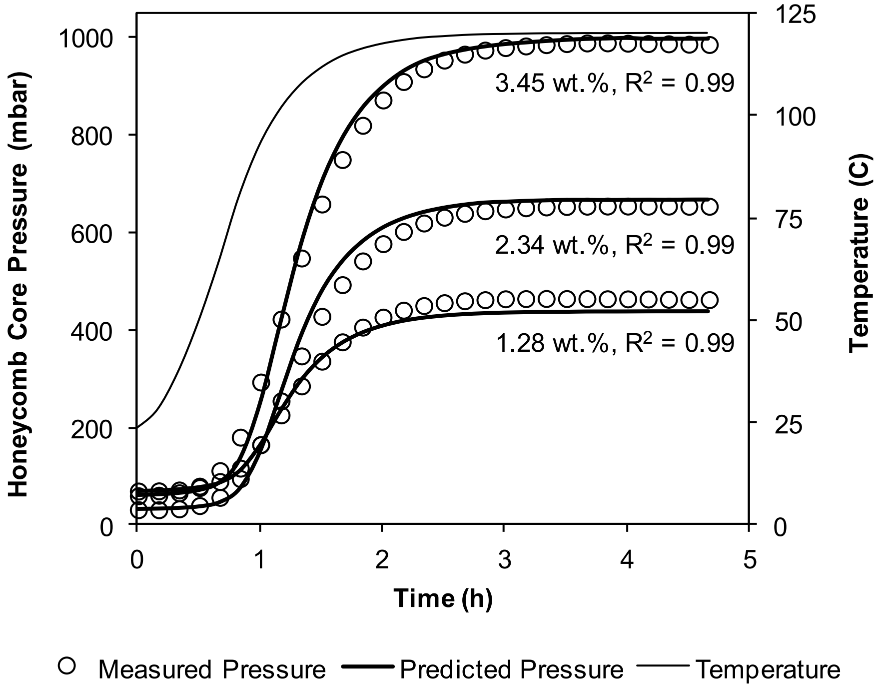

Figure 5.3. Predicted and measured honeycomb core pressure in a sealed volume during cure.

Visually, the quality of the fit is quite good with these constants and is confirmed quantitatively by the R^2 values above 0.99. The fit of the diffusion coefficient enables the model to predict the cell pressure by 6 % at the lowest moisture level tested and by 1 % at the highest moisture level. Moisture levels were tested up to 3.45 wt.% moisture because testing cores with higher moisture content risked exceeding the operating pressure (1000 mbar) of the pressure transducer connected to the cavity of the measurement fixture. This core moisture content was absorbed at an ambient relative humidity of 50 to 55 %, highlighting that moisture absorbed during handling and storage can significantly increase in core pressure during cure.

5.1.5 Model assumptions and limitations

Assumptions were used to simplify the analysis and experimental characterization needed for the honeycomb core pressure model. Possible effects of the assumptions are presented in the following sub-sections.

5.1.5.1 Ideal gas equation of state

The ideal gas equation of state was used to predict the behaviour of real gasses, air and water vapor, in Eq. (5.6). Error in the pressure-volume-temperature relationship increases as the critical pressure is approached. For VBO processing, the maximum pressure in the core cannot exceed the applied consolidation pressure of 1000 mbar. As a result, the ideal gas law has a maximum error of 1.6 % for VBO processing, which occurs at 100 °C and 1000 mbar. Above 100 °C, the error decreases. At the low pressures encountered in VBO processing, this error was accepted to avoid using steam look-up tables. Error tolerance should be re-evaluated before using this model for higher pressure processes, such as press or autoclave moulding.

5.1.5.2 Klinkenberg effects (slip flow)

As discussed in section 2.1.1, gas flow experiments with either low gas pressure or low permeability media can overestimate flow velocity because of the slip phenomenon—known as the Klinkenberg effect [28]. Klinkenberg effects were neglected in Eq. (5.7) because the air permeability measurements were conducted and applied in conditions that closely resemble the actual manufacturing process.

5.1.5.3 Diffusion into a stagnant medium

The linear relationship proposed by *Fick* [90] describes the rate of mass diffusion of one chemical species into a stagnant medium of another chemical species based on the local concentration gradient. The medium in the cell void space is not stagnant, it is moving according to Eq. (5.7). Choosing a stagnant medium in the void space drastically simplified the mass transfer analysis and experimental characterization. This assumption was found to be sufficient for the slowly leaking moist air mixture, as will be shown in section 5.2. If honeycomb skins with higher air permeability are used, the gas in the cell may not be stagnant, and a honeycomb core diffusion coefficient for a moving medium may be required.

5.2 Model comparison with experiments

The honeycomb core pressure model was compared to experiments using moist honeycomb core and 4-ply skins characterized in section 4.3.3. The Nomex® cores were conditioned at ambient temperature, 21 ± 2 °C, and four humidity levels: 12, 30, 70, and 99 % RH. The 12 and 30 %RH samples were conditioned using ambient humidity, and a desiccant chamber was used for the 70 and 99 %RH levels. A schematic of the humidity conditioning chamber is presented in Figure 5.4. A saturated salt solution (NaCl table salt in tap water) was used to create a 70 %RH level in the chamber, and tap water was used to create the 99 %RH level.

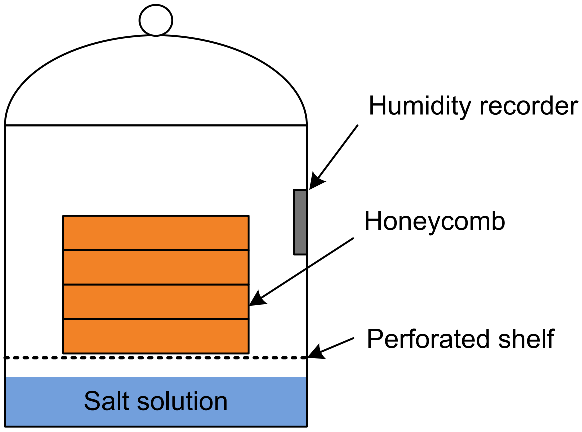

Figure 5.4. Desiccant chamber modified for humidity conditioning.

Six honeycomb samples were initially dried in a convection oven at 180 °C until the weight change was less than 0.01 wt.%. After drying, the samples were weighed daily until the change in moisture was less than 0.05 wt.%. The equilibrium moisture levels are presented in Figure 5.5. The results show that the Nomex® core moisture absorption was linear, and increased with relative humidity. As a result, Fick's laws of diffusion are valid for this material.

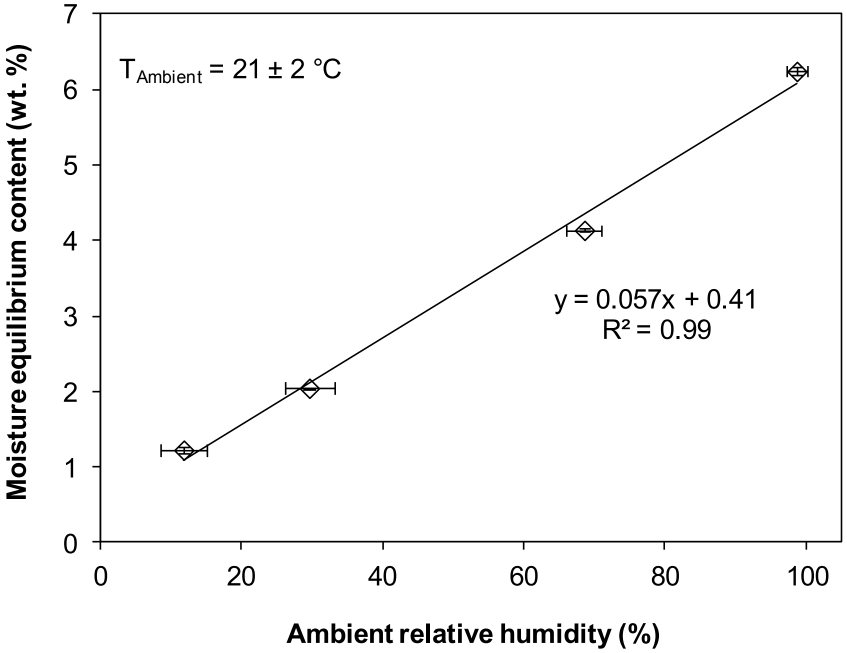

Figure 5.5. Moisture equilibrium content for the Nomex® honeycomb core used in this study.

The moist honeycomb cores were cured according to the procedure outlined in section 4.3.1 using the fixture shown in Figure 3.1. The measured honeycomb core pressure, and the model predictions using Eq. (5.6), are presented in Figure 5.6. The initial honeycomb core pressure is consistent for all experiments because the vacuum pump was connected to the cavity for 3 to 5 minutes before starting the oven. This was done to provide a consistent initial honeycomb core pressure within the cavity, in-order to identify the effect of moisture, and avoid variability that could be caused by dissimilar initial pressures.

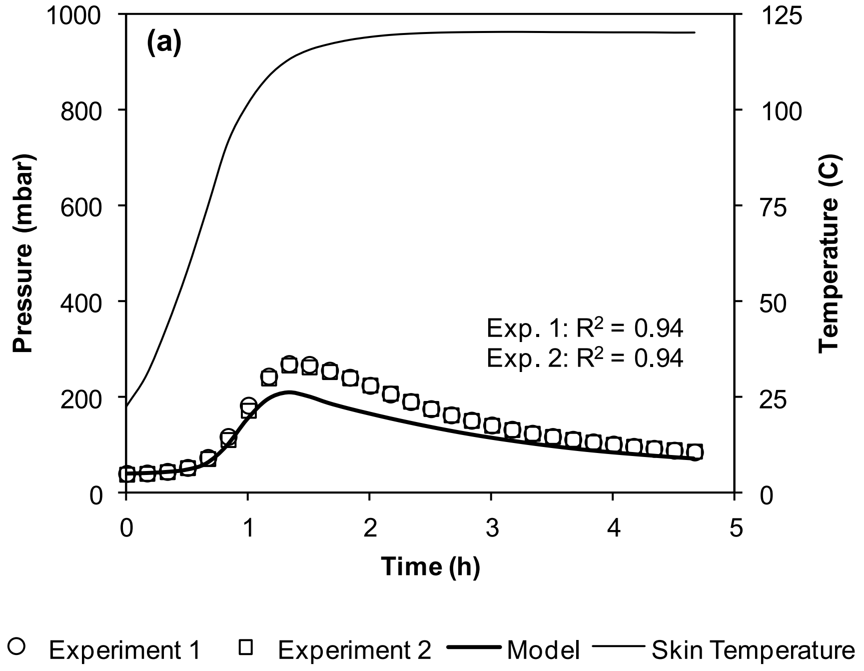
(a)
Pressure (mbar)
0
200
400
600
800
1000
Temperature (C)
0
25
50
75
100
125
Time (h)
0
1
2
3
4
5
Exp. 1: R² = 0.94
Exp. 2: R² = 0.94
○ Experiment 1
□ Experiment 2
Model
Skin Temperature

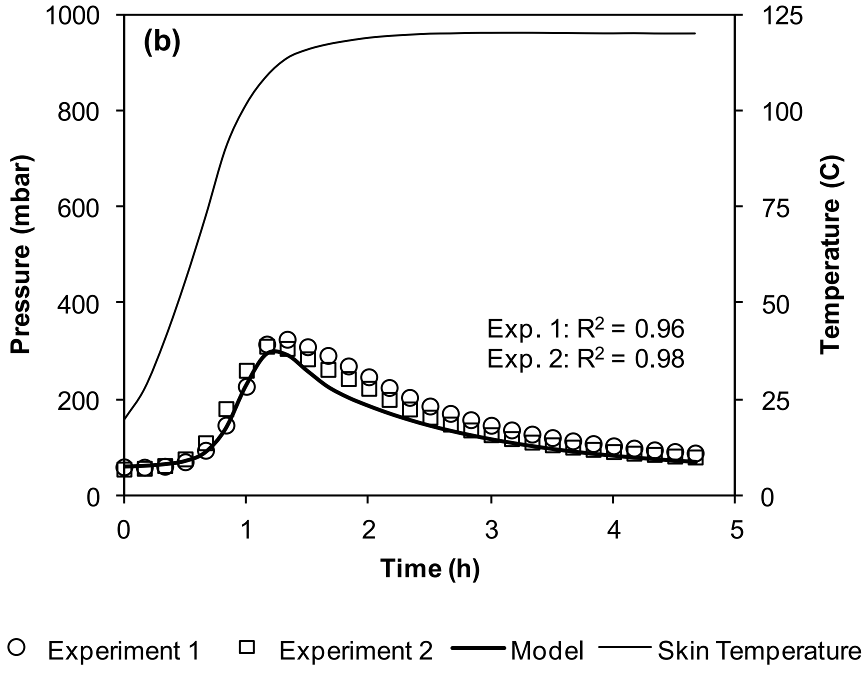
(b)
Pressure (mbar)
0
200
400
600
800
1000
Temperature (C)
0
25
50
75
100
125
Time (h)
0
1
2
3
4
5
Exp. 1: R² = 0.96
Exp. 2: R² = 0.98
○ Experiment 1
□ Experiment 2
Model
Skin Temperature

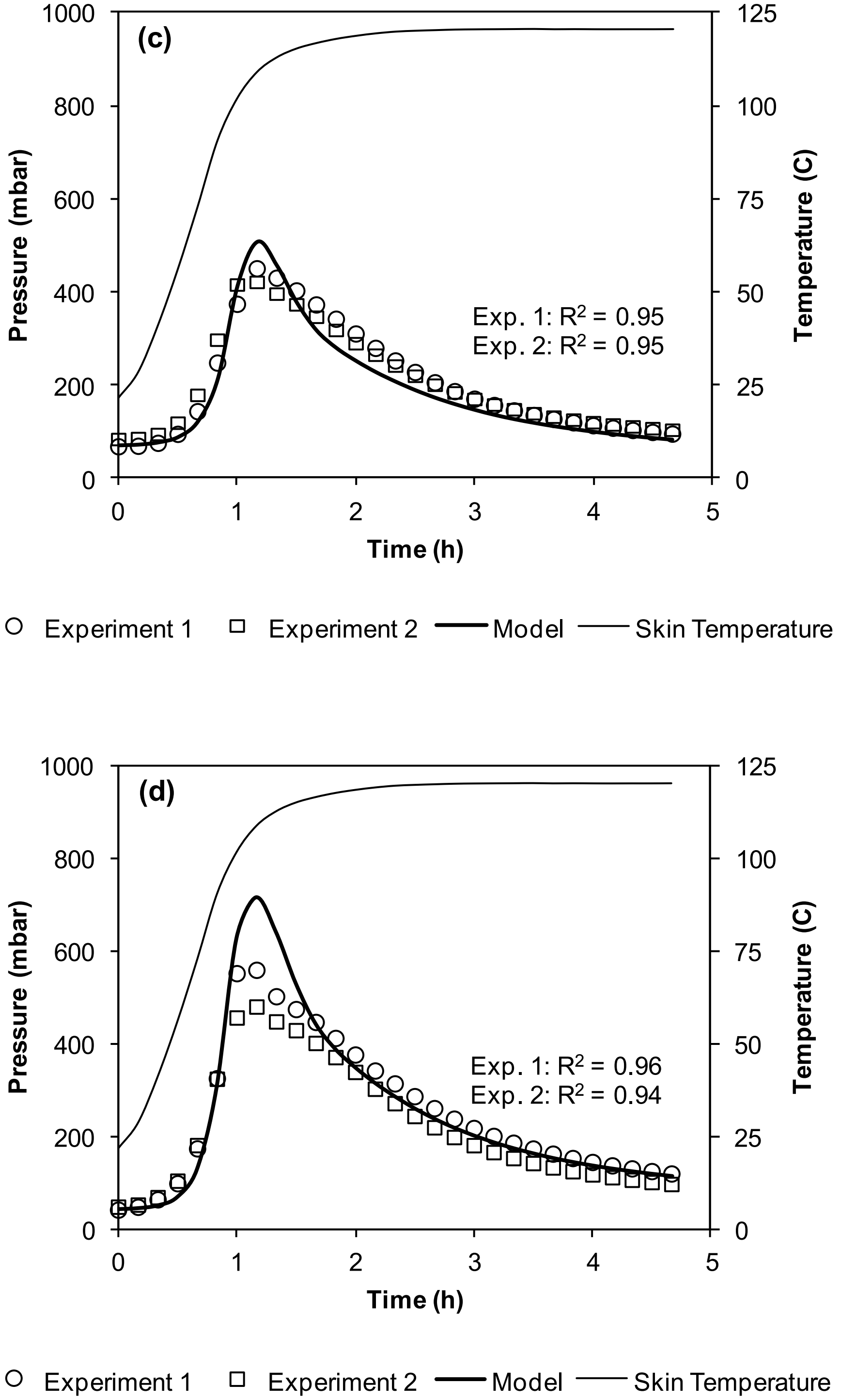

Figure 5.6. Comparison of measured and predicted honeycomb core pressure during cure. Two experimental runs are shown for each core moisture content: (a) 1.23 wt.%, (b) 2.05 wt.%, (c) 4.14 wt.%, and 6.24 wt.%. The R^2 values for both experiments indicate good agreement through most of the cure cycle.

The experimental results presented in Figure 5.6 demonstrate the effect of increasing absorbed moisture on the honeycomb core pressure during processing. Higher core moisture levels prior to cure lead to higher honeycomb core pressures during elevated temperature processing. However, the moisture-induced core pressure was not retained by the composite skin. The honeycomb core pressure decreased during processing because of gas flow through the honeycomb skin. The extent of flow on pressure can be identified by examining the different pressure responses between Figure 5.3 and Figure 5.6a. In Figure 5.3, the core that absorbed 1.28 wt.% moisture content was cured with an aluminum plate, creating a sealed volume, and had a honeycomb core pressure of roughly 450 mbar. When a composite skin was cured to a core with a similar absorbed moisture of 1.23 wt.%, as in Figure 5.6a, the peak honeycomb core pressure was 250 mbar. An absorbed moisture content of 3.45 wt.% caused the core pressure to 1000 mbar during processing in Figure 5.3. Higher moisture contents of 4.14 and 6.25 wt.% resulted in lower measured core pressured of between 400 and 550 mbar in Figure 5.6c–d.

The lower core pressures observed during processing with composite skins in Figure 5.6 is caused by gas flow through the skin. More flow through the honeycomb skin increases the likelihood of void formation during processing. Given the high air permeability of the plain weave skins, the pressure response in Figure 5.6 remained below the atmospheric consolidation pressure, decreasing the likelihood of delaminations, however, the core pressure could exceed the consolidation pressure if the materials and processing parameters were changed.

Visual inspection of the curves in Figure 5.6 indicate good agreement between the model predictions and experiments. The R^2 values between the model and experiment was calculated for each trial using Eq. (4.2). The high R^2 values confirm that the model captures the overall behaviour of the honeycomb core pressure during the processing, however, most of the deviation between the model and experiment arises near the observed peak pressure during cure. Given that the peak pressure is an important indicator for delaminations and disbonds, the error between the model and experiments was examined further in Figure 5.7.

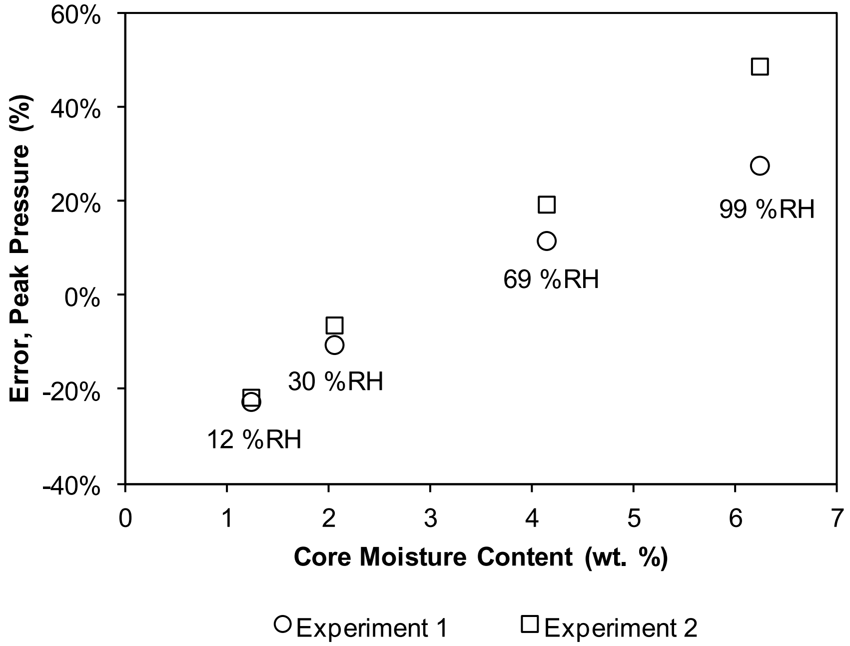

Figure 5.7. Error between honeycomb core peak pressure predictions and bag-side skin experiments. The relative humidity at which moisture equilibrium was achieved is included for reference.

In Figure 5.7, the model captured the experimental pressure within 25 % for the cores conditioned at 12, 30 and 69 %RH. The peak honeycomb core pressure error for the cores conditioned at 99 %RH is between 30 and 50 %. Some of the error at higher humidity could be attributed to the low atmospheric humidity in the lab, which was between 20 and 30 %RH during testing, therefore, it is possible that the higher humidity samples could have desorbed moisture from the time they were weighed until the cores were placed in the test fixture cavity, the skin and consumables were place over the core, the vacuum bag was installed, and the vacuum pump started—this process was approximately 30 minutes. Given that a lay-up room humidity level of 99 % is rare in a composite manufacturing environment, these results identify that the material characterization performed using bag-side skins in Chapter 4 can be successfully transitioned to the process models developed in this chapter.

5.2.1 Analysis of cured skins

The quality of the cured skins and the strength of the skin-to-core bond were evaluated by microscopy and mechanical testing. Two 60 mm microscopy samples were cut 50 mm from the edge of every cured panel and were polished to look for voids and other defects. The strength of the bond between the skin and core was evaluated using the flatwise tensile strength test of sandwich constructions. An electromechanical testing machine was used with a test fixture built to ASTM C297 specifications, and the test was conducted in accordance with the ASTM standard [91]. A total of four coupons were tested for both void content and flatwise tensile strength for each moisture level.

The void content of each skin was measured by taking images of every void and comparing the total void area to the total area of the sample, as shown in Figure 5.8. The average and standard deviation of the void content measurements of the cured skins is presented in Figure 5.9. The average void content of all skins was less than 1 %, and all visible voids were located in the resin rich region between the fibre tows. These types of voids are the result of entrapped air that is caused by poor evacuation during the vacuum hold prior to cure, or due to air flowing through the skin during cure.

Given that all panels were subjected to the same 16 h vacuum hold prior to cure, the void content was expected to increase with increasing core moisture content. This was not the case. The higher moisture content did not increase the void content of the skins, which may be caused by the air permeability of the skins. Since the skins were thin and permeable, the gas escaping the core through the skin may have completely evacuated the skin, leaving no signs of increased porosity.

The void measurement technique of analyzing a representative slice may not fully capture the void distribution within the skin. If the microscopy samples were taken from an area of the panel where less or no gas flowed through the skin, the void content measurements may show a lower void content. Determining the location within a skin where gas travelled was difficult since visual observation of the cured part showed no visible surface variations, and the resin spots in the breather after cure were approximately the same size and evenly distributed.

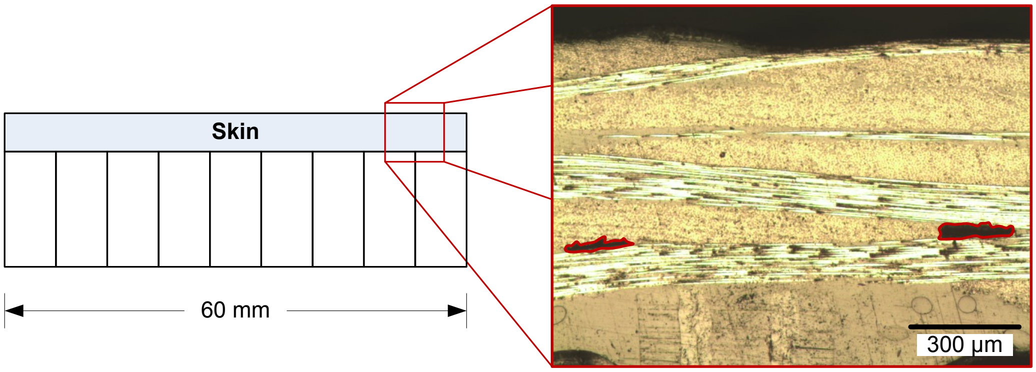

Figure 5.8. Void content measurement approach.

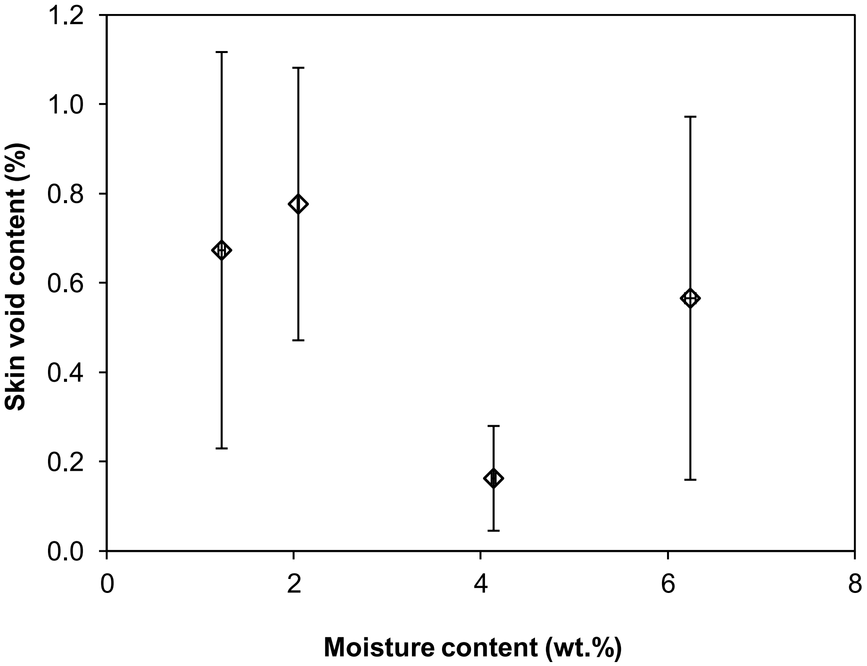

Figure 5.9. Void content measurements of cured skins.

The cured panels were tested for flatwise tensile strength and the average and standard deviation of four test samples are shown in Figure 5.10. The increased moisture content may have resulted in higher honeycomb core pressures during cure, however, these pressures were insufficient to degrade the flatwise tensile strength of the skin-to-core bond. All samples failed in the honeycomb core, not the skin-to-core bond (see Figure 5.11).

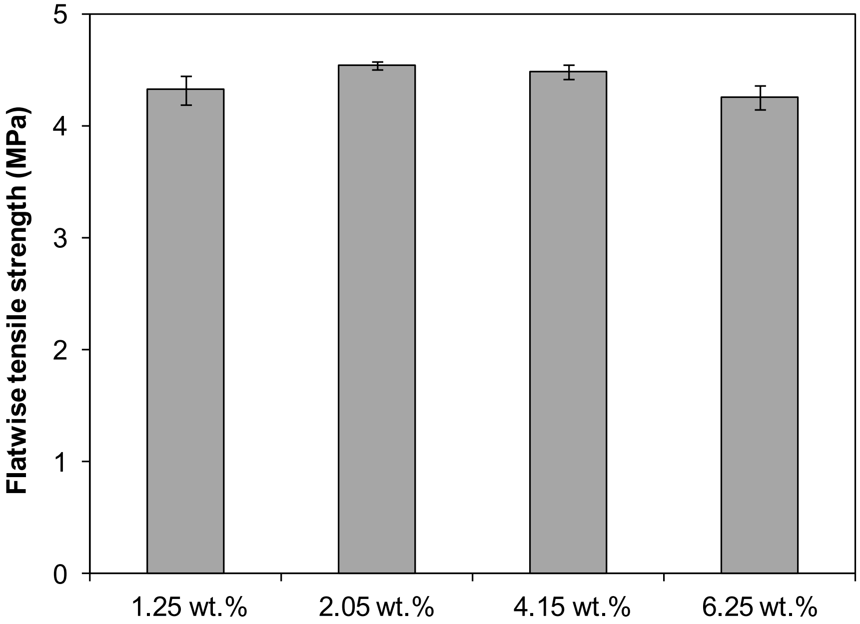

Figure 5.10. Flatwise tensile strength of Nomex® honeycomb core sandwich assemblies.

Figure 5.11. Flatwise tension test showing 100 % core failure.

5.3 Parametric Study

Models can provide detailed information about a process and can be used to reduce the trial and error approach used to develop a composite manufacturing process [85]. A parametric study can be used to present model factors in a simple format that can quickly identify their effect on the key process parameters. The honeycomb core pressure is one key processing parameter that influences consistent, predictable part quality for VBO honeycomb panels. Major defects have been observed in cured parts when the honeycomb core pressure equals or exceeds the consolidation pressure at during elevated temperature processing [12]. If this occurs near gelation, the panel will likely be scrapped, however, consistent part quality is more likely if the honeycomb core pressure remains below the applied consolidation pressure throughout processing. The process parameters that influence the honeycomb core pressure can be indentified from Eq. (5.6), Eq. (5.7), and Eq. (5.22), and they are listed in Table 5.1.

Table 5.1. Material and process parameters influencing honeycomb core pressure.

Parameter	Type	Significance
K	Material property	Reduces P_{Core} by allowing gas flow through the bag-side skin
D	Material property	Increases P_{Core} by introducing moisture into the cell void space
P_{Bag}	Process condition	Determines the pressured gradient through the skin and applies the consolidation pressure to the honeycomb panel
M_{Paper}	Process condition	Influences the mass of vapor introduced to the cell void space
$m_{Air,\ i}$ & $m_{Vapor,\ i}$	Material property and process condition	Determines the initial P_{Core} at the start of elevated temperature processing.

This parametric study focused on the parameters likely to change in a manufacturing environment: the influence of air permeability of different fabric forms, percent moisture absorption in the honeycomb core, and the initial honeycomb core pressure at the start of curing. These parameters were chosen because they can vary with the fabric architecture (see Figure 4.7) and storage and handling prior to processing (see Figure 5.5).

A unidirectional prepreg skin with adhesive is likely to have lower air permeability during cure, on the order of 10^{-19} m^2 [15], when compared with the plain weave prepreg studied in this chapter. As part size increases, lay-up times will also increase, exposing honeycomb cores to ambient moisture for longer periods, likely causing the core moisture content to reach equilibrium with the lay-up room humidity level. The last parameter studied was the initial honeycomb core pressure (caused by the mass of air and vapor in the cells). This can change with variability in skin air permeability during the vacuum hold prior to cure, the length of the vacuum hold, the volume of the core, and the relative humidity of the entrapped gas. For this study, the relative humidity of the air initially entrapped within the honeycomb core was assumed to be constant at 50 %RH—a common lay-up room set-point.

These three parameters were varied independently using the model presented in section 5.1, and the maximum predicted core pressure was recorded for the cure cycle shown in Figure 4.15. The simulations result in a 3-dimensional surface plot of pressure as a function of skin air permeability and core moisture content. An example where the initial core pressure was 50 mbar is shown in Figure 5.12. If the combination of moisture and skin permeability creates a condition where the maximum core pressure during elevated temperature processing exceeds 1000 mbar, the honeycomb core pressure moves from the light (blow atmospheric pressure) region into the dark (above atmospheric pressure) region of the graph.

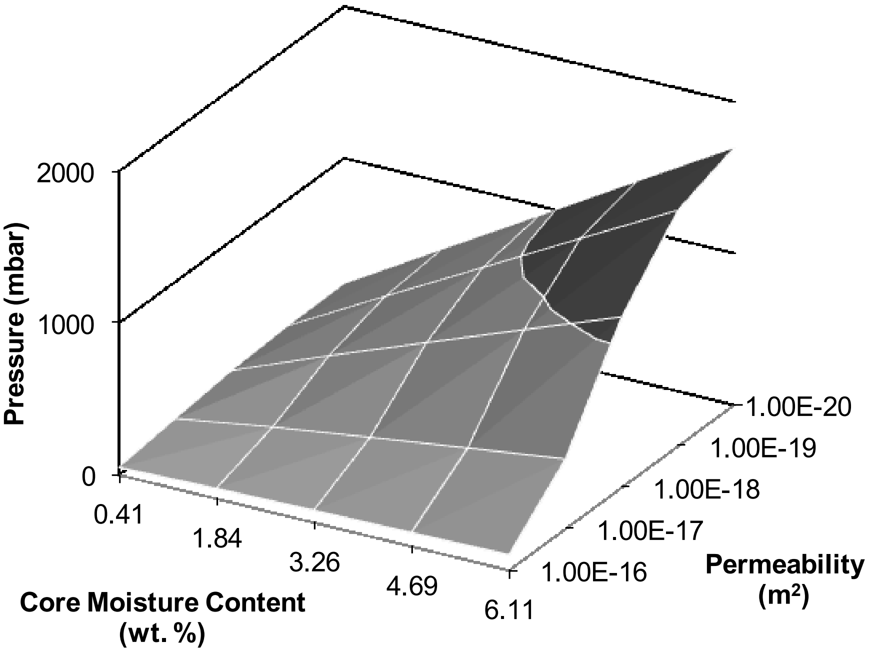

Figure 5.12. 3-D surface plot showing the maximum honeycomb core pressure observed during cure with increasing core moisture and decreasing skin permeability. The initial core pressure in this plot was 50 mbar.

Multiple 3-D surfaces can be created with increasing initial honeycomb core pressures. Overlaying these plots onto a 2-dimensional contour can provide a process map to identify what combination of initial core pressure, material air permeability during processing, and core moisture content is needed to prevent the honeycomb core pressure from exceeding the process consolidation pressure. This was done for two consolidation pressures in Figure 5.13. A 1000 mbar of consolidation pressure, would be achieved by a high vacuum level (20–30 mbar) at sea level, and is presented alongside a scenario where a reduced consolidation pressure of 800 mbar was encountered during processing. The reduced consolidation pressure could be caused by tooling leaks, poor bagging, insufficient vacuum pump capacity, moisture off-gassing of the consumable materials, or manufacturing at altitudes higher than sea level. As a consequence, process robustness suffers with reduced consolidation pressure.

These process maps can be used to identify if core pressure could exceed the consolidation pressure during processing. For example, cores that have reached a moisture equilibrium at 50 %RH, no $P_{Core,i}$ at point A will cause the core pressure to equal the consolidation pressure during processing. If skin air permeability was reduced, as in point B, $P_{Core,i} < 250$ mbar is required for the core pressure to remain below the consolidation pressure throughout processing. For the same prepreg and core moisture content, at point C, $P_{Core,i} < 500$ mbar and at point D, $P_{Core,i} < 50$ mbar for the honeycomb core pressure to remain below the reduced consolidation pressure.

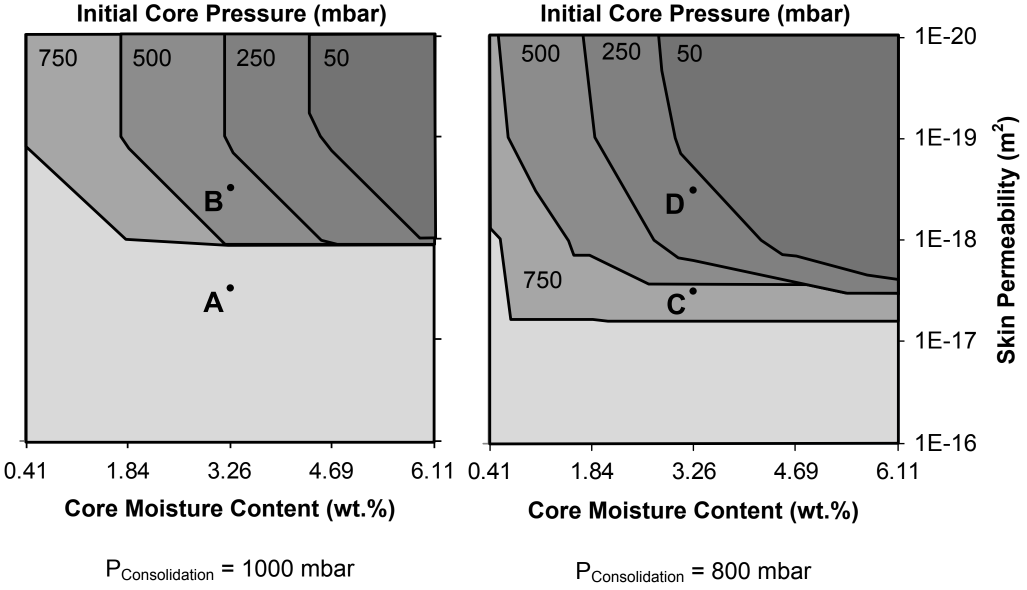

Figure 5.13. Process maps for honeycomb core pressure during 121 °C processing cycle with 1000 mbar (left) and 800 mbar (right) of consolidation pressure. The honeycomb core pressure remains below the consolidation pressure in the light area and exceeds the consolidation pressure in the dark area.

In practice, these process maps could be used to select materials or solve processing issues for non-metallic honeycomb sandwich panels. If poor quality parts are being fabricated, five options can be considered to move the peak (predicted) honeycomb core pressure from the dark (above atmospheric pressure) to the light (below atmospheric pressure) regions of the process map:

1. Process modifications: The consolidation pressure can be increased by improving the vacuum level achieved under the vacuum bag. This

could be achieved by fixing tooling leaks, improving vacuum pump capacity and/or achievable vacuum level.

2. Tighter process controls: The layup room humidity set-points can be lowered or creative solutions may be needed to dry the honeycomb core, and then prevent or slow moisture adsorption during the lay-up process.
3. Improving the skin air permeability: The pre-processing air permeability of the honeycomb skin can be characterized as outlined in section 4.2.3, and the duration of the pre-processing vacuum hold can be increased based on the predictions from Eq. (3.12) to lower the initial honeycomb core pressure. If the permeability results in a time-consuming vacuum hold that limits production, perforating the skins can reduce the pre-processing vacuum hold period [15], or selecting a combination of skin materials (prepreg and adhesive films) with higher air permeabilities can be considered.
4. Processing cycle: Modifying the temperature profile could improve panel quality but change cured resin physical properties. Increasing the time spent at maximum air permeability (by introducing a devolatilization dwell), or lowering the cure temperature could be considered to reduce the honeycomb core pressure observed during cure.
5. Selecting a different honeycomb core: Korex® or Kevlar® based honeycomb cores may be more suitable than Nomex® for VBO manufacturing because they absorb less moisture. As a result the honeycomb core pressures observed during processing would be reduced. However, these cores are more expensive.

These materials and processing variables are summarized in Figure 5.14. If none of these variables can improve honeycomb panel quality to meet the performance requirements, increasing the applied consolidation pressure or lowering the material design allowables may be considered.

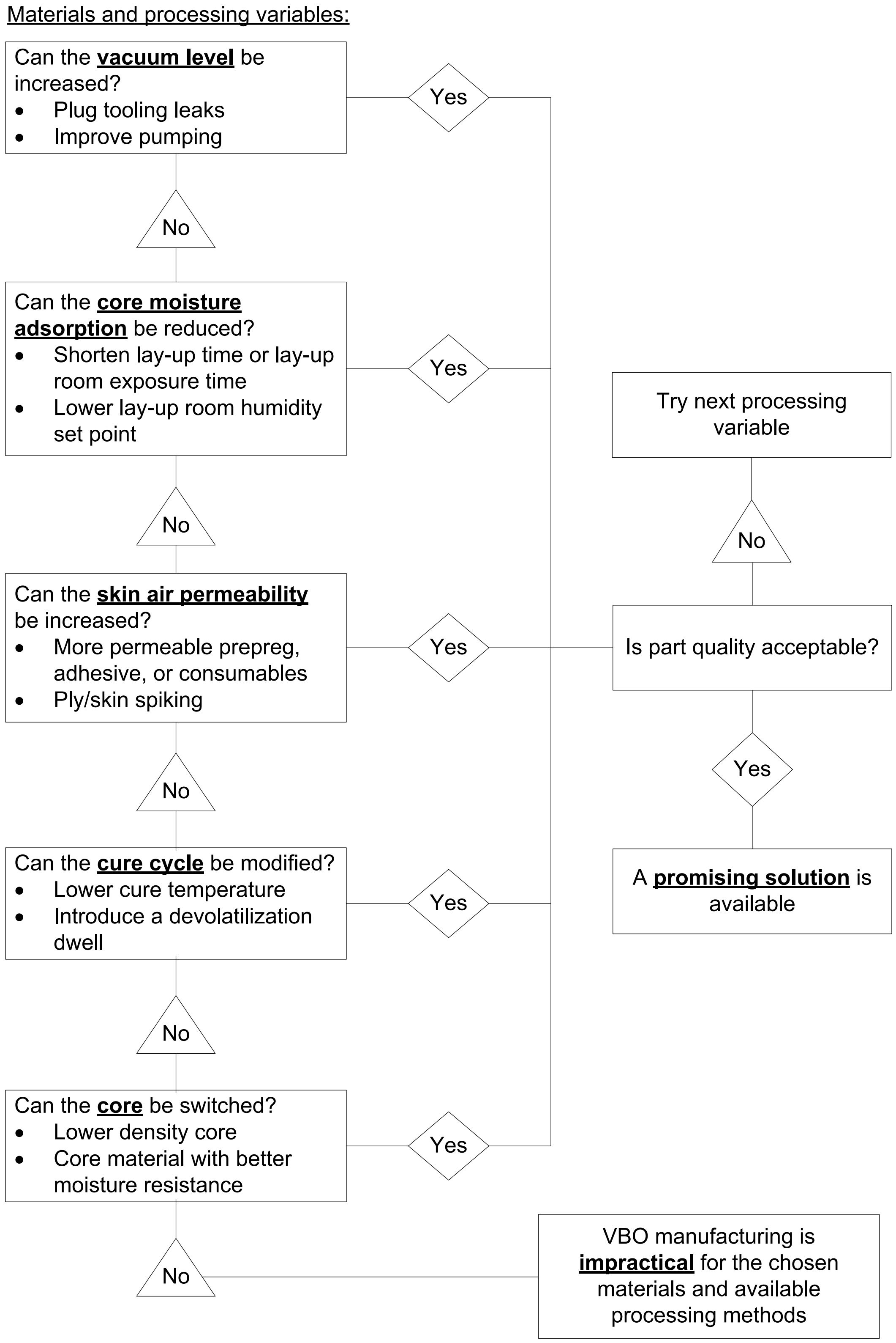

Figure 5.14. Flowchart to evaluate materials and processing variables to improve VBO honeycomb panel quality.

5.4 Summary

A process model for vacuum bag only co-curing was developed to predict the honeycomb core pressure during cure. The inflow of moisture from the honeycomb paper walls into the core space was governed by Fick's law, and the flow of moist air out of the core, through the bag-side skin, was governed by Darcy's law for a compressible gas. Although some deviation existed between the measured and predicted honeycomb core pressure, the characterization techniques and modelling approaches were found to provide practicable inputs to predict the honeycomb core pressure during cure.

The honeycomb core pressure did not exceed atmospheric pressure in this study because the air permeability of the honeycomb skin was sufficiently high to allow entrapped air and moisture to flow through the skin. The increasing pressure gradient of the Nomex® sandwich assemblies produced similar flatwise tensile strength values because the Nomex® core was the limiting factor in the strength of the assembly. In terms of porosity, the void contents were similar for all configurations because the thin permeable skins allowed any gas travelling through the core to simply pass through, and not remain entrapped within the skin. These observations are encouraging, demonstrating the robustness of the skins chosen in this study.

Process maps were produced where skin permeability, moisture content, and the initial honeycomb pressure were varied for a 121 °C processing cycle. The process maps showed how the honeycomb pressure can exceed the consolidation pressure for a combination of moisture content, skin air permeability, and high initial core pressures. The likelihood of the honeycomb pressure exceeding the consolidation pressure increased when the manufacturing environment leads to reduced consolidation pressures, such as vacuum bag leaks or a high-altitude manufacturing facility. Recommendations were presented to troubleshoot the VBO honeycomb manufacturing process.

Chapter 6

In-situ Process Monitoring

In this chapter, process models are combined with dual-skin lab-scale honeycomb panels by embedding micro-fabricated pressure sensors in the honeycomb core. As a result, the honeycomb core pressure is measured throughout the manufacturing process, linking the previously developed process models to real honeycomb panels. A patented miniature sensor technology from Convergent Manufacturing Technologies was used [81]. A technique was developed to embed the pressure sensors into honeycomb cores in-order to minimize disturbing the process phenomena and avoid creating leak paths. Once embedded, the honeycomb core pressure was measured during the vacuum hold prior to cure and during elevated temperature processing in an oven. Panels were also autoclave cured to identify the effect of higher consolidation pressure on the measured honeycomb core pressure response and model predictions.

6.1 Experimental

A lab-scale solution is developed in the following sections to simulate co-curing of large composite structures. First, the sensors are described. Second, the embedding procedure is developed. Finally, the test matrix is presented.

6.1.1 Sensors

A piezoresistive silicon micromachined pressure sensor from Measurement Specialties (model number: MS5407-AM) was selected to measure the honeycomb core pressure. A picture of the sensor is shown in Figure 6.1. The actual pressure sensor is 2 mm × 2 mm, but the associated packaging increased the total size to 6.4 mm × 6.2 mm. This sensor was chosen because it offered 0.2 % linearity within the operating pressure, and an operating temperature of 125 °C.

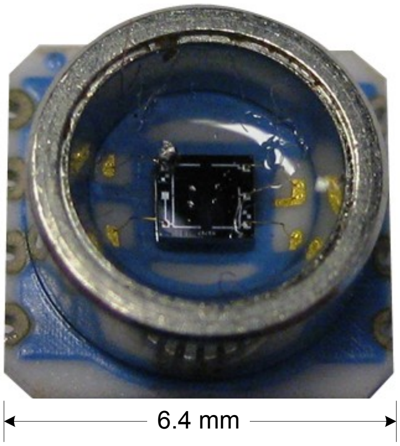

Figure 6.1. Miniature surface mounted pressure sensor from Measurement Specialties. The micro-machined piezoresistive silicon sensor is mounted in the center of a ceramic carrier, and protected by a metal cap filled with gel.

The sensor has a Wheatstone bridge wiring configuration, and therefore required 4 wires to be soldered to the back side of the carrier. Enamel coated copper magnet wire was used to connect the sensor to the data acquisition system to avoid introducing leaks along the wiring. Twenty-eight gauge wire was found to offer the best balance of handling, durability and size; thirty-two and thirty-six gauge wires were evaluated, but those sizes readily became entangled and broke at the solder joints, even with very cautious manipulation.

These pressure sensors offered temperature compensation by embedding a fluorocarbon polymer coated thirty-gauge K–type thermocouple wire beside the pressure sensor within the honeycomb. The temperature compensation required a four-point calibration at two temperatures: 22 °C and 125 °C, and two pressures: 0 and 1000 mbar.

6.1.2 Embedding sensors in a honeycomb core

A simple solution was sought to embed the pressure sensor and pass the wires through the panel without introducing leaks and subsequently disrupting the pressure behaviour. A schematic of the embedding technique is presented in Figure 6.2. To restrict in-plane air flow at the perimeter of the core, a 150 mm × 150 mm × 20 mm aluminum frame was fabricated from 12 mm thick square tubing. Six slots (3 mm wide × 4 mm deep) were machined on one side to allow the wires to pass through the frame. A blind 3 mm diameter hole, 3 mm deep, was drilled in the center of the slot to provide an anchoring point. The wires were potted with a Room Temperature Vulcanizing silicone rubber (RTV silicone) that was temperature resistant up to 200 °C after seven days at room temperature.

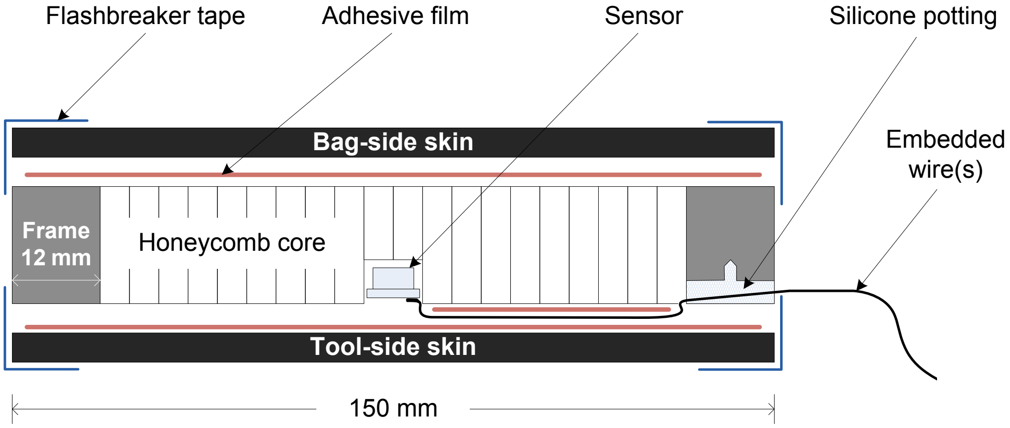

Figure 6.2. Cross-section schematic showing the sensor position and embedding technique.

The quality of the wire potting was evaluated using two approaches: first a flow meter leak test, and second, a hot water bath to visually confirm no leaks were present. The frame with embedded wires was sandwiched between two aluminum plates using rubber to create a seal between the plates and the frame with potted wires. A flow meter and pressure transducer were connected between one of the plates and a vacuum pump. If the flow rate fell to zero once vacuum was achieved in the frame, this confirmed that the embedded wires did not create any leak paths through the edges of the frame. To visually confirm the leak test was valid, atmospheric pressure was vented into the frame, and the assembly was submerged into a water bath at 50 °C to identify if the wires leaked. If a leak was identified, it was repaired with additional silicone and the evaluation procedure was repeated until both the flow meter registered zero flow and no bubbles appeared when the frame was submerged in the hot water bath.

The pressure sensor was located in the centre of the frame, but the pressure sensor did not fit into a single 3.1 mm honeycomb core cell. A 12 mm diameter blind hole was drilled 8 mm deep into the centre of the honeycomb core, connecting a total of five cells. The six wires (four for the Wheatstone bridge and two for the thermocouple) were encapsulated between two layers of adhesive film between the pressure sensor and the edge of the frame, as shown in Figure 6.3a. Alternative solutions that were considered included cutting a groove in the core for the wires, but this would allow air migration between the edge and centre of the panel. Air migration could be eliminated by potting the wires in the groove with silicone, but this would introduce a foreign material near the sensor, possibly skewing the measured pressure. Sealing the wires between 2 layers of adhesive film between the sensor and panel edge offered a solution that could be scaled to larger parts without adding foreign materials or additional weight to the panel.

After the wires were sandwiched between two layers of adhesive film (Figure 6.3b), the prepreg and surfacing film were laid-up directly onto the adhesive, completing the tool-side skin. A layer of Airtech's Flashbreaker® II polyester film tape was applied around the perimeter of the skin to prevent in-plane gas flow during processing (Figure 6.3c). The frame was then placed tool-side down onto a non-perforated release film covering 12 mm thick aluminum tool. The bag-side adhesive film and prepreg layers were applied (Figure 6.3d) over the core. Again, Fashbreaker® II tape was placed around the perimeter of the panel. Sealing the panel edges was intended to reproduce the pressure in a large honeycomb panel by preventing in-plane flow. The embedded wires were sealed at the exit point of the aluminum frame and the vacuum bag between two layers of sealant tape.

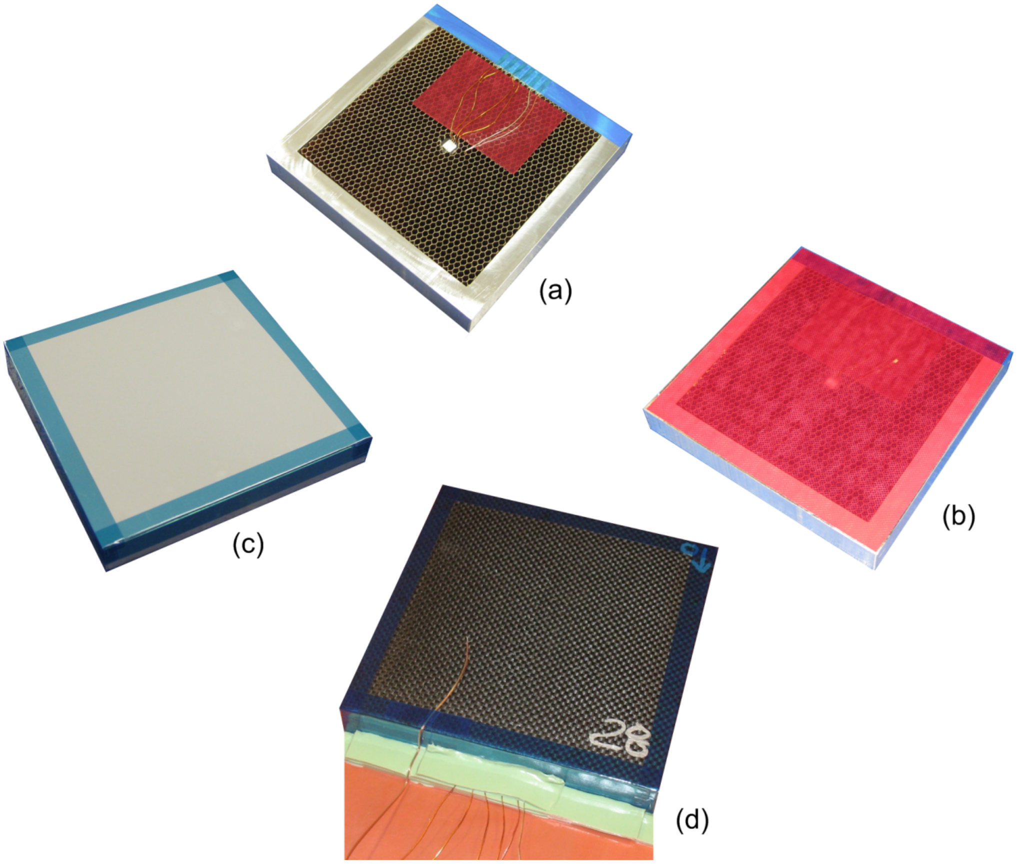

Figure 6.3. Embedding procedure: (a) honeycomb core with embedded pressure sensor in the centre with wires passing above a layer of adhesive film to the exit points of the aluminum frame, (b) adhesive film covering the core and sandwiching the wires, (c) tool-side skin with surfacing film and taped edges, and (d) bag-side skin with taped edges skin thermocouple and embedded sensor wires exiting the panel between sealant tape.

6.1.3 Test matrix

Elevated temperature processing was performed in an atmospheric pressure oven and an autoclave. The autoclave was located at the National Research Council of Canada Institute for Aerospace Research. The test matrix is presented in Table 6.1. The oven experiments (Trials 1 through 3) were used to identify the effect of moisture absorbed by the honeycomb core on the measured and predicted core pressure. The autoclave experiments (Trials 4 through 7) were used to identify the effect of consolidation pressure on the measured and predicted core pressure.

Table 6.1. Embedded sensor panel test matrix.

Trial	Cure type	Core moisture content, MC_{Core} (wt. %)	Target ΔP_{Skin} (mbar)	Measured vacuum bag pressure (mbar)[d]	Measured external bag pressure (mbar)[d]	Number of panels
1	Oven[a]	1.59	1000	118 ± 23	1024 ± 1	1
2	Oven[b]	2.44	1000	16 ± 4	1021 ± 2	1
3	Oven[a]	3.93	1000	118 ± 23	1024 ± 1	1
4,5	Autoclave[c]	2.44	1000	1017 ± 1	2028 ± 140	2
6,7	Autoclave[c]	2.44	2000	99 ± 4	2028 ± 140	2

[a] Cured together on the same tool in the same oven run
[b] Cured on an identical tool, in the same oven, but a different oven run
[c] All panels cured in the same autoclave run on separate tools
[d] Average and standard deviation measured during cure

The consolidation pressure exerted on the honeycomb skin during cure was equivalent in Trials 1 through 5 (see Figure 6.4). Trials 1 through 3 were conducted under 1000 mbar of vacuum pressure, and trials 4 and 5 were performed with a total of 1000 mbar of positive pressure – the vacuum bag was vented to atmosphere (roughly 1025 mbar) and the autoclave pressure was roughly 2050 mbar. In Trials 6 and 7, vacuum pressure was maintained in the vacuum bag and the 2050 mbar autoclave pressure effectively doubled the compaction pressure applied to the honeycomb skin.

As the compaction pressure is increased on a fibre bed, the pore space is reduced, lowering fibre bed permeability to liquids [92]. A similar relationship is expected with air permeability. Equivalent compaction pressures can be applied by a combination of vacuum pressure and ambient pressure, as shown in Figure 6.4. Comparing the measured honeycomb core pressure and the model predictions in these experiments will identify whether the magnitude of the consolidation pressure is the driver when characterizing the material properties for process models, or whether both magnitude and application type (positive autoclave pressure or negative vacuum bag pressure) influence the air permeability behaviour of the skin, and therefore the honeycomb core pressure.

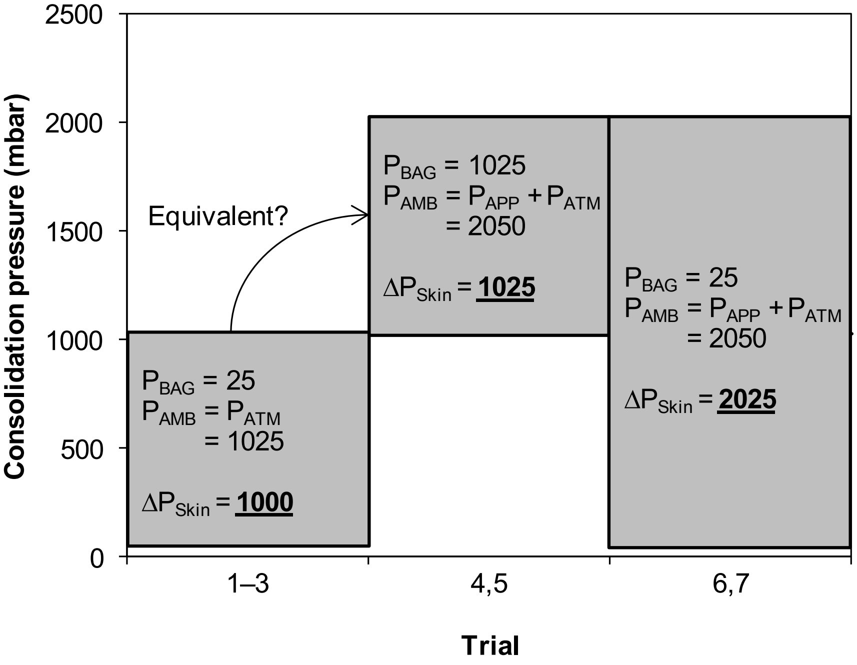

Figure 6.4. Consolidation pressure applied to the honeycomb skins during cure.

The cure cycle presented in Section 4.3.1 (Figure 4.11) was used for both oven and autoclave trials. The bag-side skin temperature of the panels was measured using a separate K–type thermocouple to the one described in section 6.1.1.

Two vacuum ports were used for each tool. One was connected to the vacuum pump, the other was connected to a pressure transducer (range: 0 to 3000 mbar) to record the vacuum bag pressure using the same data acquisition system as the embedded sensors. The autoclave vessel pressure was measured using a separate pressure transducer (range: 0 to 10,000 mbar) connected to the autoclave data acquisition system.

6.2 Results

The evolution of honeycomb core pressure during the vacuum hold prior to cure is plotted in Figure 6.5. The vacuum hold was performed at atmospheric pressure for all oven and autoclave trials. The lower vacuum bag pressure measured in the autoclave vacuum hold (Figure 6.5b) occurred because a portable vacuum pump was required overnight. Both vacuum holds were intended for 12 h, but the autoclave panels were held under vacuum for an additional 3.5 h because extra time was needed to pass the pressure sensor and thermocouple wires between the autoclave door and ring lock without damaging the wires.

The measured honeycomb core pressure is plotted alongside two model predictions from Eq. (3.12) in Figure 6.5. A constant air permeability value of 8.6 x 10^{-18} m^2 was used to generate the model predictions. This air permeability value was measured during the extended pre-cure vacuum hold in Figure 4.17. This value was an average of measurements exhibiting significant variability, including the delay in core pressure decrease. As a result, the model predicts faster core evacuation than measured. The core pressure model was re-plotted using the air permeability value after the pre-cure vacuum hold for comparison, and fits the experimentally data.

The honeycomb core pressure measured during the pre-cure vacuum hold shows significant variability. The same observation was made during the experimental characterization of bag-side skin air permeability (see Figure 4.4). The air permeability measurements at time t = 0 h in Figure 4.17 span an order of magnitude. The measured honeycomb core pressure decrease during the vacuum hold has the same shape as the model prediction, however variation exists in rate and initiation of the core pressure decrease. Even with the variability in the first half of the vacuum hold, the honeycomb core pressure at the end of the vacuum hold was within 80 mbar of the predicted pressure for all seven panels. This observation reinforces the air permeability variability that exists with out-of-autoclave prepregs and that an extended vacuum hold at room temperature is required to ensure evacuation of the air entrapped in the core.

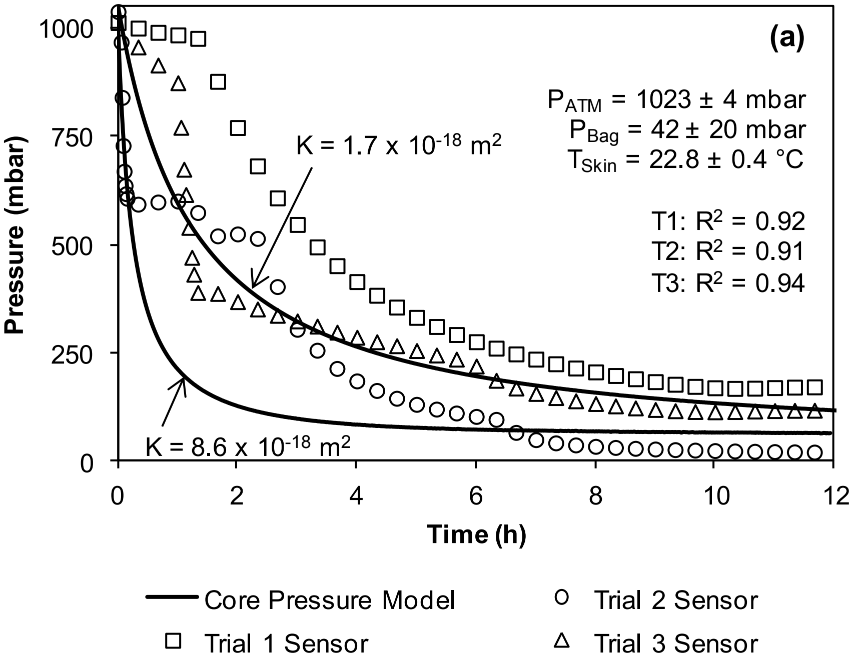

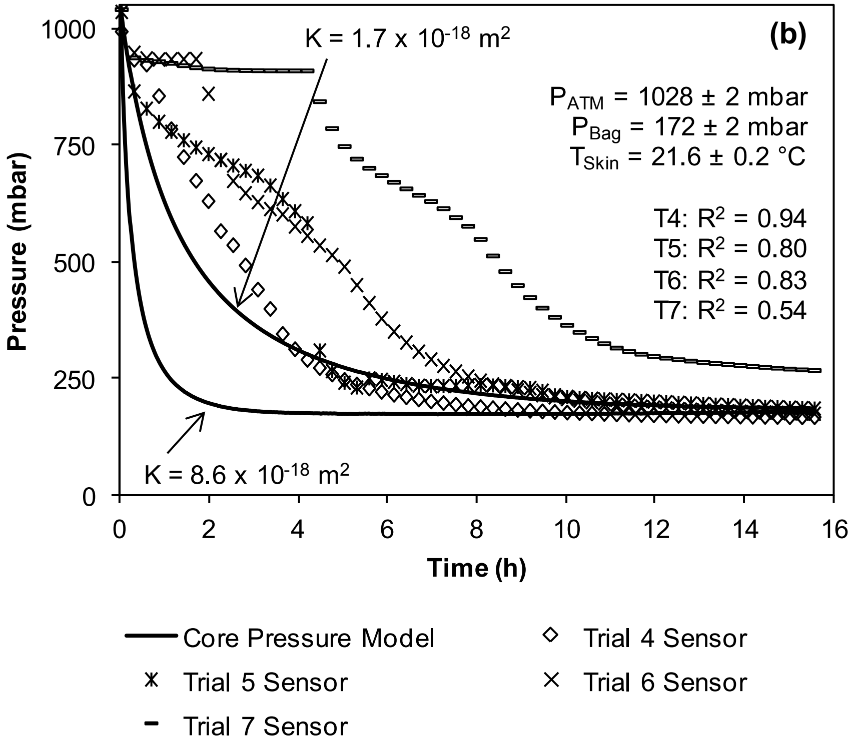

Figure 6.5. Predicted and measured honeycomb core pressure during the vacuum hold prior to cure for the embedded sensor panels: (a) VBO trials and (b) autoclave trials. The R2 value was calculated for K = 1.7 x 10^{-18} m^2.

The dynamics of the honeycomb core pressure change during the vacuum hold was noticeably different for all panels, and unlike the model predictions, demonstrated abrupt changes. Since fluid flow through a porous medium depends on the interconnectivity of the pore space [23], the measured pressure drop indicates that the pore space within the honeycomb skin continuously evolves throughout the vacuum hold. As pores become connected or isolated, the change in honeycomb core pressure is affected.

More erratic behaviour in the honeycomb core pressure signal was observed with the embedded sensor panels than the air permeability measurements from Figure 4.4. This was likely caused by the localized area where pressure was measured by the sensor. The embedded pressure sensor is located within a 12 mm diameter cell section, and was therefore more sensitive to the local changes in honeycomb skin air permeability. The honeycomb core pressure that was measured in the material characterization studies was measured in a 150 mm × 150 mm cell area, with interconnected cells. As a result, the material characterization was less sensitive to local changes in skin air permeability.

The elevated temperature processing results for the oven cured panels are presented in Figure 6.6. The embedded pressure sensor measurements are plotted alongside the vacuum bag pressure and the model predictions from Eq. (5.6). All panels show a similar trend during elevated temperature processing. As the temperature increased the honeycomb core pressure increased. This is caused by pressurization of entrapped volatiles (air and water vapour). Additional water vapour was desorbed from the honeycomb cell walls during processing, as predicted by the model. The majority of the pressure increase within the honeycomb core occurred during the temperature ramp because increasing temperature has the strongest influence on diffusion kinetics; a lower cure temperature could have lowered the honeycomb core pressure, but would also lengthen cure time.

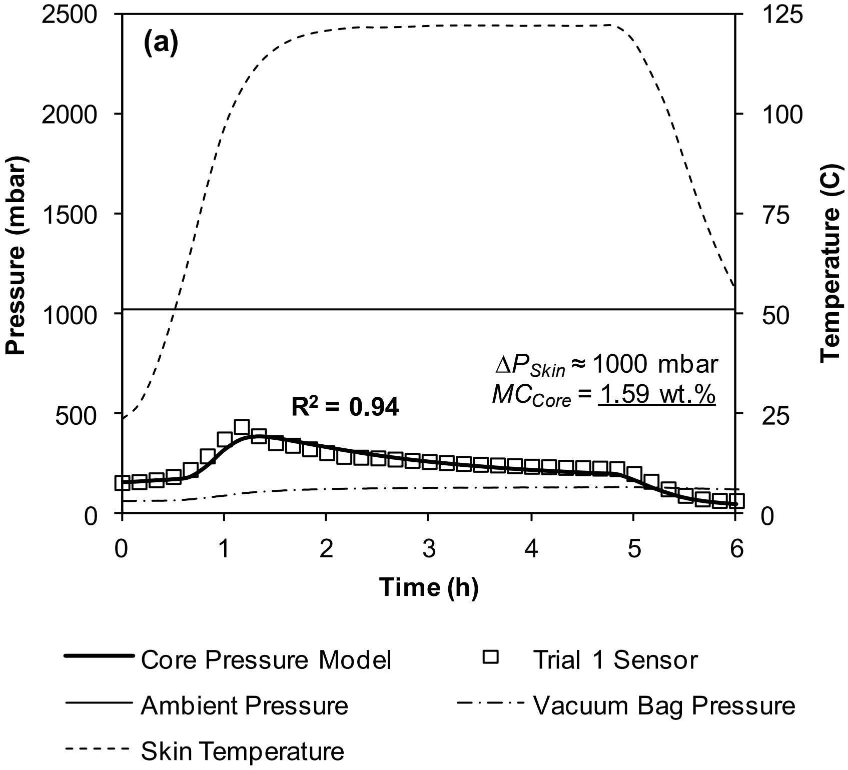
(a)
Pressure (mbar)
0
500
1000
1500
2000
2500
Temperature (C)
0
25
50
75
100
125
Time (h)
0
1
2
3
4
5
6
R^2 = 0.94
$\Delta P_{Skin} \approx$ 1000 mbar
MC_{Core} = 1.59 wt.%
Core Pressure Model
□ Trial 1 Sensor
Ambient Pressure
Vacuum Bag Pressure
Skin Temperature

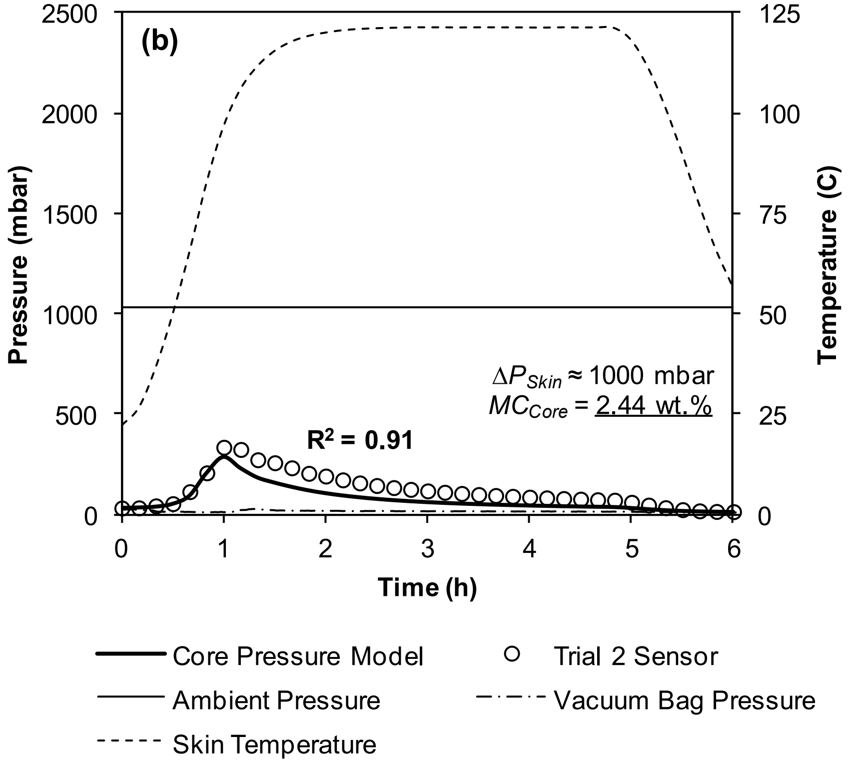
(b)
Pressure (mbar)
0
500
1000
1500
2000
2500
Temperature (C)
0
25
50
75
100
125
Time (h)
0
1
2
3
4
5
6
R^2 = 0.91
$\Delta P_{Skin} \approx$ 1000 mbar
MC_{Core} = 2.44 wt.%
Core Pressure Model
○ Trial 2 Sensor
Ambient Pressure
Vacuum Bag Pressure
Skin Temperature

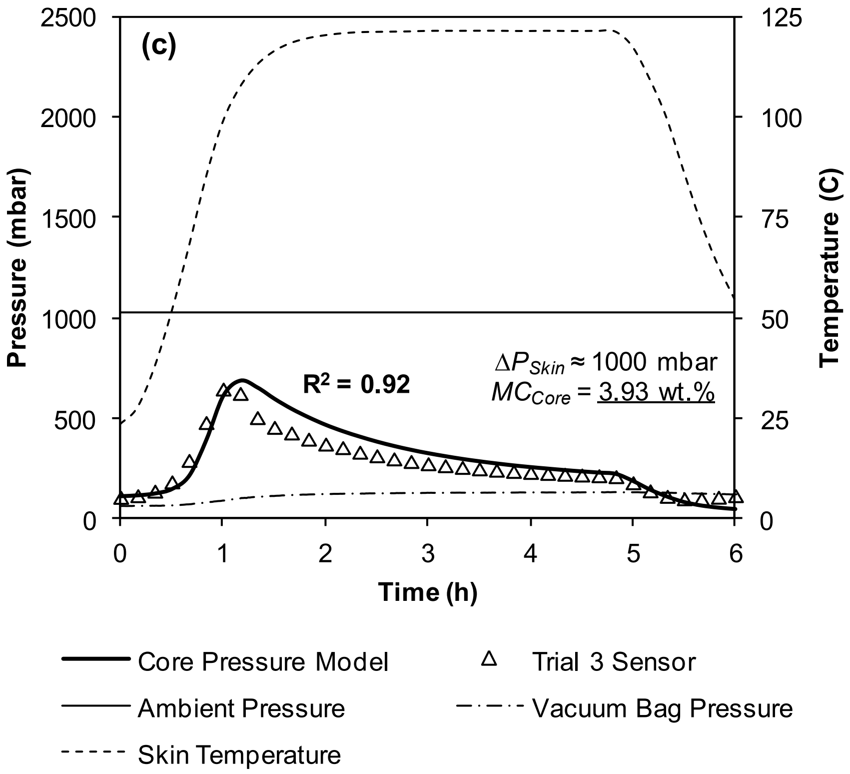

Figure 6.6. Predicted and measured honeycomb core pressure during oven co-curing of honeycomb panels. The model captures the overall pressure behaviour with increasing moisture absorbed by the honeycomb core: (a) 1.59 wt. %, (b) 2.44 wt. %, and (c) 3.93 wt. %. The core pressure model predictions are computed using the average air permeability data from Figure 4.17

Once the temperature reached the dwell temperature (roughly 1.25 h into the cycle), moisture diffusion slowed, and the air permeability of the honeycomb skin dominated. During the temperature dwell (from 1.25 to 5 h) the honeycomb core pressure decreased according to the model predictions. The variability in honeycomb core pressure was reduced during elevated temperature processing. The three VBO experiments were close to the model predictions. The measured honeycomb core pressure in Figure 6.6a was within the model bounds, Figure 6.6b was higher, and Figure 6.6c was lower. The model developed using material characterization of bag-side skins was able to reproduce the measured pressure in representative panels featuring moisture-absorbed honeycomb core.

An unexpected experimental factor was the sub-standard vacuum level in the vacuum bag for Trials 1 and 3. The vacuum bag required eight tucks for each part, used to create extra slack in the bag to avoid breaking or bridging the vacuum bag during cure. Trials 1 and 3 were cured simultaneously on the same tool, and Trial 2 on the same tool but a different oven run. The bag for Trial 1 and 3 required more tucks (possible leak points), which lead to a lower vacuum level than Trial 2. The vacuum level achieved during the material characterization was similar to the level in Trial 2 (16 ± 4 mbar), not that of Trial 1 and 3 (118 ± 23 mbar). Vacuum bag pressure is a model input, and an encouraging result was that the model was capable of predicting honeycomb core pressure with a 100 mbar reduction in vacuum level during cure.

The measured and predicted honeycomb core pressure results from the autoclave co-cured panels are presented in Figure 6.7. All panels were autoclave cured simultaneously, but Trials 4 and 5 were on separate tools from Trials 6 and 7. The autoclave pressure was ramped to the 2050 mbar set-point in 1 min, and the vacuum bag was vented 5 min after the pressure set-point was reached. The fluctuations observed in the autoclave pressure signal during cure are an artifact of the controller, which is tuned for normal autoclave operation between 4000 and 8000 mbar, not the target set-point of 2000 mbar used in this study.

In Figure 6.7a, the consolidation pressure applied to the skin through the differential between the inside and outside the vacuum bag is similar to the air permeability characterization, and the trials in Figure 6.6. Once the vacuum bag was vented, the measured honeycomb core pressure followed the model predictions towards the vacuum bag pressure. The measured honeycomb core pressure followed the upper bound of the model predictions until the dwell temperature was reached. During the dwell, the measured honeycomb core pressure in Trial 4 decreased, similarly to those of VBO Trials 1 through 3. The honeycomb core pressure in Trial 5 remained above the model predictions.

In Figure 6.7b, the vacuum bag pressure was maintained throughout the cure cycle, effectively doubling the consolidation pressure applied to the honeycomb skin, when compared to Figure 6.6 and Figure 6.7a. The measured honeycomb core pressure increased faster, and peaked 300 mbar above the model predictions. Doubling the consolidation pressure created higher honeycomb core pressures during the ramp than predicted by the model. This would imply that doubling the consolidation pressure decreased the air permeability of the skin. However, the model does capture the honeycomb core pressure decrease during the dwell. This could be an artifact of the volume of gas that flowed through the skin to lower the pressure in the honeycomb core. The gas flow could have created large pores within the skin, increasing skin air permeability. This however, would require further investigation.

The error in the peak pressure predictions and the embedded sensor trials is shown in Figure 6.8. The predicted pressures were within 15 % of the measured pressure for each of the embedded sensor trials with 1000 mbar of consolidation pressure (Trials 1 through 5). As the consolidation pressure was increased to 2000 mbar, the error in predicted pressure increased towards 30 to 35 %.

Comparing oven and autoclave experiments identified that the process models are accurate when the total consolidation pressure is equivalent. This correlation offers end-user the flexibility to characterize the honeycomb skin air permeability in an oven using a vacuum bag in order to find the necessary process model parameters for light positive pressure curing in a vented vacuum bag.

All panels cured in this study (Figure 6.6 and Figure 6.7) were submerged in a hot water bath (described in section 6.1.2) after co-curing to verify that the panels were sealed at the edge and where the wires exited the aluminum frame. No leaks were caused by the wires before or after curing. If leaks were present during cure, the measured pressure would be expected to fall below the predicted pressure, which was not the case in Figure 6.6 or Figure 6.7.

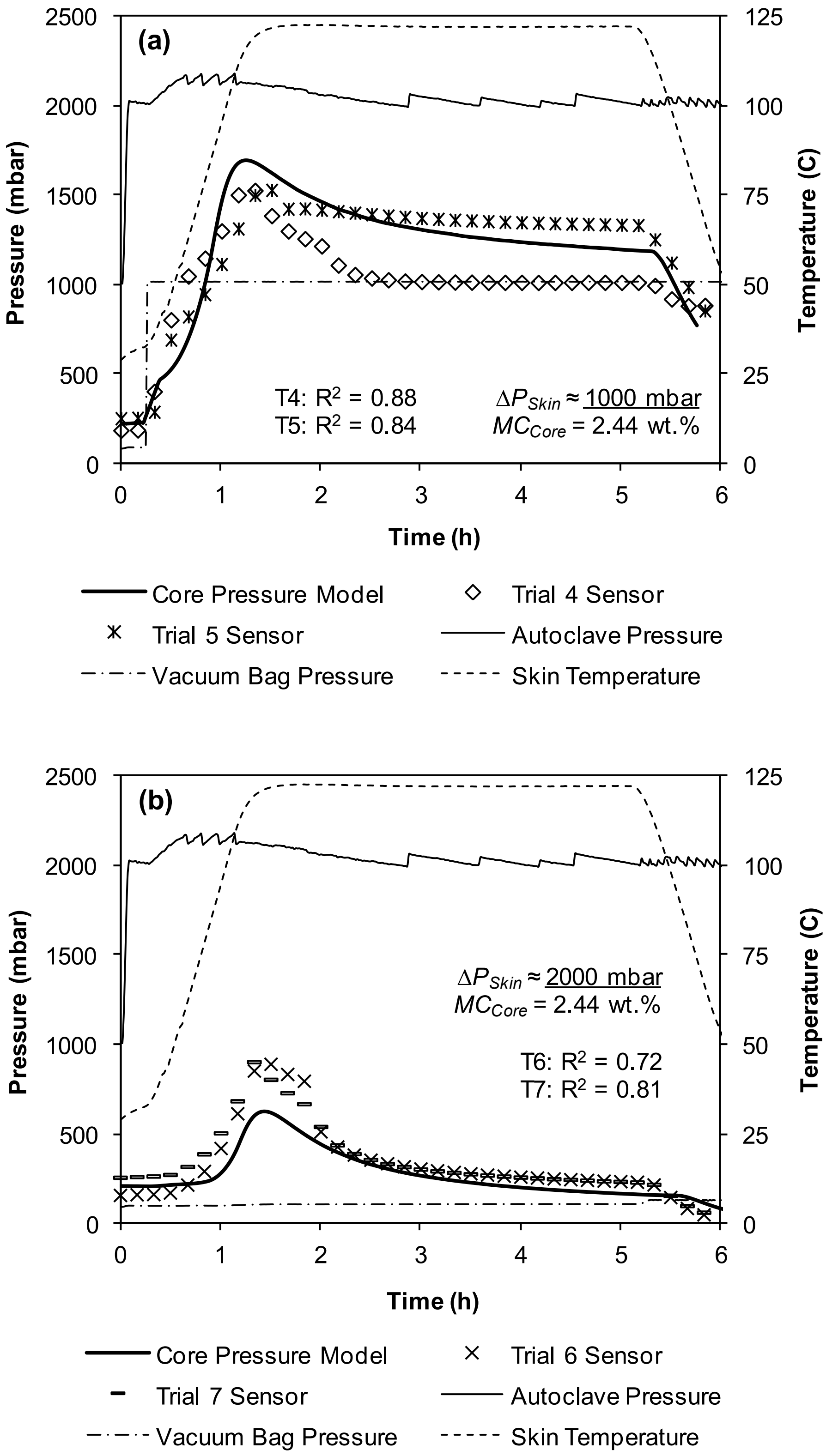

Figure 6.7. Predicted and measured honeycomb core pressure during autoclave co-curing: (a) vacuum bag vented to atmosphere and (b) vacuum maintained in bag.

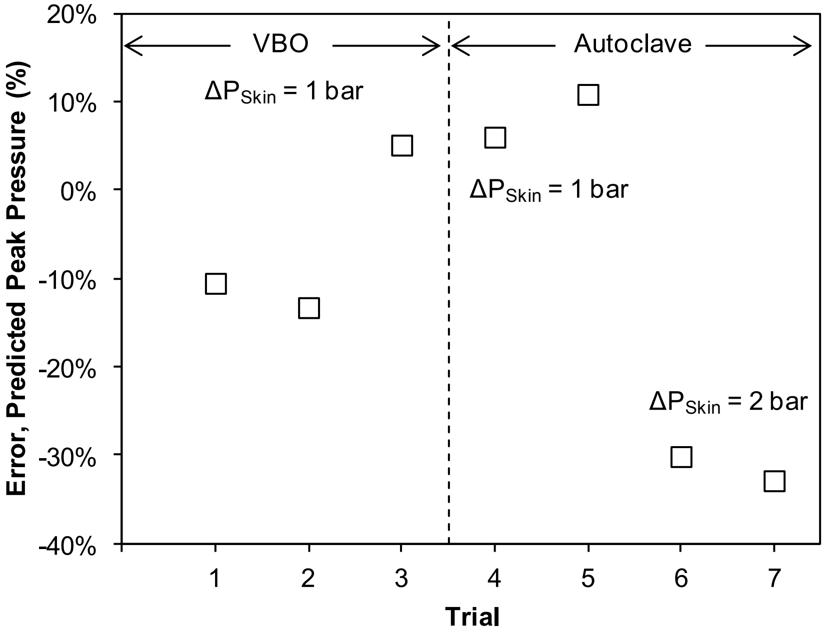

Figure 6.8. Error between honeycomb core peak pressure predictions and the embedded sensor trials.

6.3 Summary

Miniature pressure sensors were successfully embedded into honeycomb sandwich panels with minimal sensor interference, and leaks were prevented along the wiring. Although the sensor embedding technique was effective, a wireless pressure and temperature measurement solution that fits into a single honeycomb cell would be preferred in the future as an alternative to sandwiching wires between adhesive film and potting the wires in silicone at the edge of the panel.

The honeycomb panels were configured with impermeable boundary conditions at the panel edges to reproduce curing of large-scale honeycomb structures in a laboratory environment. The measured pressure response was compared to process models developed using characterization techniques where only the bag-side honeycomb skin was considered. The honeycomb core pressure evolution during processing agreed with the process model predictions. In the cases of moisture-absorbed by the honeycomb cores, temperature transitions, variable vacuum bag and external pressures, the measured pressure response was captured by the process models. These results reinforce that material characterization and process modelling can be used to predict holistic phenomenon if intelligent assumptions are used. Neglecting the tool-side skin during characterization and modelling was a convenient and accurate assumption for large parts because gas flow is predominantly in the transverse breathing direction.

In the case of traditional autoclave processing, the external bag pressure can be much higher than in an atmospheric pressure oven. However, the process models were accurate if the consolidation pressure applied to the honeycomb skin is effectively the same as VBO processing. This inspires confidence in the models chosen to analyze the honeycomb pressure behaviour. The models accurately predicted the honeycomb core pressure behaviour for any combination of vacuum and positive pressure that applies an equivalent consolidation pressure to the conditions used during material characterization.

Chapter 7

Conclusions, Contributions, and Future Outlook

The use of composite materials is growing, and the search for low-cost manufacturing alternatives to autoclave curing is underway. Vacuum-bag-only (VBO) manufacturing of out-of-autoclave (OOA) prepregs may produce autoclave quality honeycomb panels if the honeycomb core pressure prevents defects from forming within the sandwich assembly. The main objective of this work was to study the transport phenomena in VBO manufacturing process for honeycomb sandwich panels. To achieve this objective, the honeycomb core pressure was studied by coupling material characterization and process modelling of simplified, single-skin honeycomb panels to realistic, dual-skin honeycomb panels. The following conclusions and contributions can be drawn from this work:

1. **Honeycomb skins require out-of-autoclave prepregs that create a transverse interconnected pore space.**

   The in-plane (K_{xx}) and transverse (K_{zz}) air permeability was studied for three OOA prepregs featuring micro-pores created by partial impregnation of the fibre reinforcement. The plain weave prepreg formed connected macro-porosity networks after lay-up, offering the highest transverse air permeability (K_{zz}) during the pre-processing vacuum hold; the unidirectional and 5 harness satin prepregs were mostly impermeable in transverse direction ($K_{zz} \approx 0$) because these prepregs featured isolated macro-pores after lay-up. Transverse gas flow was identified as the predominate mechanism to evacuate entrapped air from honeycomb panels because of the low aspect ratio (*h/L*) of honeycomb skins.

Original contribution: Qualitative (micro-CT) and quantitative (air permeability measurements) approaches were coupled to identify that prepregs with connected macro-porosity networks after lay-up, compared to prepregs with isolated macro-pores, are required for air evacuation prior to VBO processing of honeycomb panels.

2. **The honeycomb core pressure can exceed the consolidation pressure during VBO manufacturing.**

   The honeycomb core pressure during elevated temperature processing can exceed the available consolidation pressure during VBO processing through a combination of low air permeability, high initial honeycomb core pressure, and absorbed high moisture content.

   Original contribution: A process model was developed to relate honeycomb core pressure to material transport phenomena during VBO honeycomb panel fabrication. The model was used to study the effect of process parameters and offer guidelines to resolve core pressure-induced defects in VBO manufacturing of honeycomb panels.

3. **Holistic honeycomb core pressure behaviour was governed by the bag-side skin.**

   The experimental fixture used to characterize the material properties and develop the honeycomb panel co-cure process model was successfully used to predict holistic pressure phenomena. Miniature pressure sensors were embedded in dual-skin honeycomb panels to measure the *in-situ* pressure response.

   Original contributions: 1) A technique was developed to embed miniature sensors into honeycomb panels and **2)** Single-skin (bag-side) laboratory experiments provide the required material properties for full scale (dual-skin) modelling of the pressure behaviour of honeycomb panels.

7.1 Future outlook

Additional aspects of VBO processing of honeycomb sandwich panels that could be studied in follow-on projects include:

1. **Develop OOA curable prepregs with higher transverse air permeability.**

   The OOA materials used in this work had a high in-plane to transverse air permeability ratio. Tailoring the fabric areal weight, resin content, or the initial degree-of-impregnation could be studied to improve the transverse air permeability. As a result, the pre-processing vacuum can be reduced to improve total cycle time.

2. **Model void growth in honeycomb skins during co-cure.**

   A non-uniform compaction pressure arises within honeycomb skins, and fibre bed properties (such as fibre bed stress, resin pressure, and void pressure) could be studied in conjunction with air permeability to further the scientific understanding of void growth in honeycomb panels.

3. **Develop a 3D transient model to predict honeycomb core pressure as a function of time and position for panels with in-plane breathing.**

   If a combination of in-plane and transverse breathing is used, the pressure profile within the honeycomb panel would be become 3D. Understanding this pressure profile can help define the duration of the pre-processing vacuum hold.

4. **Study the effect of batch-to-batch prepreg air permeability on part quality.**

   Significant variations in air permeability were observed with the single batch of prepreg used in this study. As OOA prepregs transition into from research and development into production, batch to batch variability may arise, leading to process deviation. The effect of prepregging process parameters could be studied to evaluate air permeability sensitivity to process tolerances. Furthermore, rapid incoming material inspection tools could be developed to identify if the prepreg air permeability meets process specifications.

Appendix A

Thermal Models

Cure kinetics and viscosity models were developed as part of this thesis work, and they are presented in this appendix. Models were developed for the Cycom 5320 out-of-autoclave epoxy resin and the AF 163-2K adhesive film.

A.1 Materials

A commercially available out-of-autoclave toughened epoxy resin system was used in this study: Cycom® 5320 by Cytec Engineered Materials Inc. The resin was supplied in neat resin film format for cure kinetics and viscosity characterization. A commercially available structural adhesive film was used to co-cure the skin to the honeycomb core: AF 163–2K by 3M. The adhesive film was supplied with a knit carrier. Adhesive supplied in an unsupported format would have been preferred for the cure kinetics and viscosity characterization, but was unavailable. To maintain similar out-time between samples, the materials were tested within 24 hours of being removed from storage in a freezer that was kept below –10°C.

A.2 Cure kinetics

The combination of a Dynamic Scanning Calorimeter (DSC) and phenomenological modelling were used to predict the cure behaviour of the thermosetting polymers [93]. In this study, a TA Instruments Q100 DSC was used to measure the heat flow of resin samples in dynamic and isothermal conditions. Four ramps were performed at 2 °C/min to obtain the total heat of reaction of the resins. Additionally, two isothermal dwells were performed over the processing window to obtain the experimental cure rate and degree-of-cure. The isothermal tests were held at constant temperature until the sample heat flow approached zero. Each isotherm was repeated twice, and a summary of all DSC tests is presented in Table A.1.

Table A.1. DSC and rheology test matrix for Cycom 5320 resin and AF 163-2K adhesive.

Test	Cycom 5320	AF163-2K
DSC ramp (°C/min)	2	2
DSC isotherm (°C)	80, 100, 120, 140, 160, 180	80, 100, 120
Rheometer ramp (°C/min)	0.56, 1.7, 2.8, 5.6	1, 2, 3
Rheometer isotherm (°C)	93, 107, 121, 149	80, 100, 120

To extract the cure rate from the DSC data, measured heat flows were converted into cure rates using the techniques presented by *Khoun et al.* [94]. The first step was to use the dynamic DSC data to calculate the total heat of reaction. The DSC heat flow signal was plotted as a function of time, and a linear integration of the area under the heat flow curve was used to calculate the total heat of reaction for each system. The second step was to compute the experimental cure rate for each isothermal dwell. By assuming the cure rate was proportional to the measured heat flow, the experimental cure rate for each time step in every isotherm was computed as follows:

$$\frac{d\alpha}{dt} = \frac{1}{Q_T}\frac{dQ}{dt} \qquad \text{(A.1)}$$

where $d\alpha/dt$ is the cure rate, Q_T is the total heat of reaction, and dQ/dt is the heat flow from the DSC. The experimental degree-of-cure, α, was obtained by integrating Eq. (A.1).

A cure kinetics model was fit to the experimental data using the process outlined in [94]. The initial degree-of-cure of the resin was assumed to be 0.01, and then the cure rate was predicted based on the current degree-of-cure and temperature. One model used to describe the curing behaviour of thermosetting resins was by developed by *Kamal and Sourour* [95]:

$$\frac{d\alpha}{dt} = K\alpha^m(1-\alpha)^n \tag{A.2}$$

where K is the Arrhenius temperature dependency

$$K = A\exp\left(\frac{-E_A}{RT}\right) \tag{A.3}$$

In Eq. (A.2) and (A.3), E_A is the activation energy of the resin, and A, m, and n are constants. The activation energy of each material was calculated by measuring the slope of $ln(d\alpha/dt)$ versus $1/T$ for low degrees-of-cure ($\alpha < 0.1$), and all other constants were determined using a weighted least squares curve fit with the experimental data. The shape of Eq. (A.2) is a bell curve, and did not adequately describe the experimental data.

Another model commonly used for thermosetting resins includes a diffusion factor developed by *Cole et al.* [96], to account for the shift from kinetics to a diffusion controlled reaction as the degree-of-cure increases above gelation. The model is

$$\frac{d\alpha}{dt} = \frac{K\alpha^m(1-\alpha)^n}{1+\exp\left(D(\alpha(\alpha_{C0}+\alpha_{CT}))\right)} \tag{A.4}$$

where, D is the diffusion constant, α_{C0} is the critical degree-of-cure at absolute zero, and α_{CT} accounts for the increase in critical degree-of-cure with temperature. The model described by Eq. (A.4) captured the overall trend of the Cycom 5320 reaction, particularly the diffusion at higher degrees-of-cure, but could be improved. A faster cure rate exists in the experimental data at low degrees-of-cure ($\alpha < 0.1$). To account for this additional reaction at low degrees-of-cure, Eq. (A.2) was added to Eq. (A.4), resulting in

$$\frac{d\alpha}{dt} = K_1\alpha^{m_1}(1-\alpha)^{n_1} + \frac{K\alpha^{m_2}(1-\alpha)^{n_2}}{1+\exp\left(D(\alpha(\alpha_{C0}+\alpha_{CT}))\right)}. \tag{A.5}$$

The additional reaction at low degrees-of-cure is apparent in the 120 °C isotherm for Cycom 5320. The high cure rate at low degrees-of-cure causes the cure rate to peak just above a degree-of-cure of 0.1, before following a more traditional autoclave epoxy system curing behaviour for the remainder of the reaction. To identify the contribution of Eq. (A.2) and (A.4) to capture the complex curing process summarized by Eq. (A.5), all three models are presented with the experimental cure behaviour in Figure A.1. For this OOA resin system, the principal reaction is described by Eq. (A.4), and the spike in cure rate at low degrees-of-cure is described by Eq. (A.2).

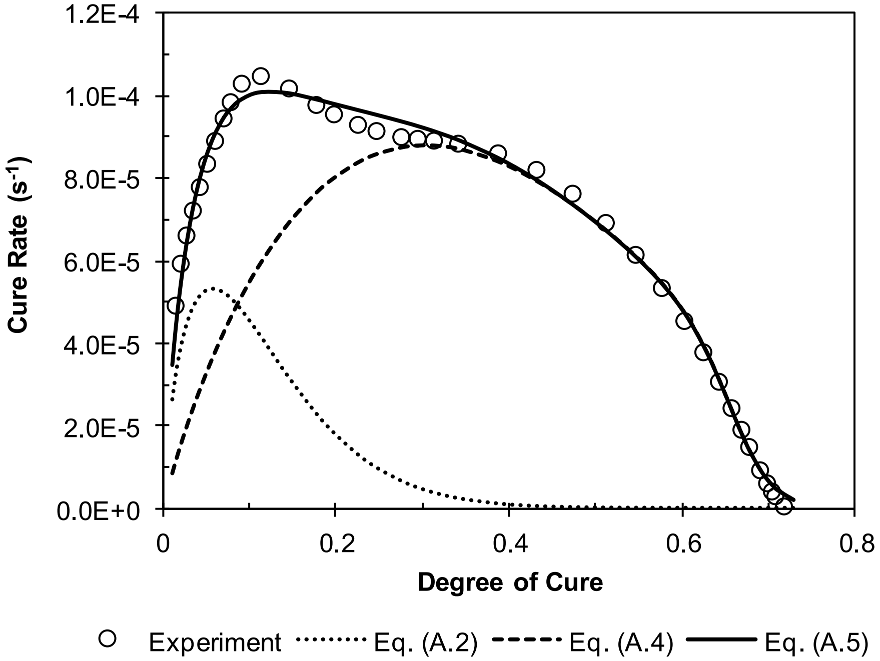

Figure A.1. Measured and predicted cure rate for Cycom 5320 at 120°C. The model, Eq. (A.5), is decomposed to show the contribution from Eq. (A.2) and (A.4).

To illustrate the effectiveness of the cure kinetics model developed with Eq. (A.5), the experimental and predicted cure rate for Cycom 5320 are shown in Figure A.2. For clarity of the low temperature cure rates, the cure rates are only shown for 80 to 140 °C cure range. The fit for 5320 is excellent at cure temperatures below 120 °C, but as the cure temperature increase towards 140 °C, the model prediction deviates slightly from the experimental data, but has a comparable shape. The adhesive film has a more traditional curing behaviour (see Figure A.3), which was adequately captured by Eq. (A.4). The cure kinetics parameters are summarized in Table A.2.

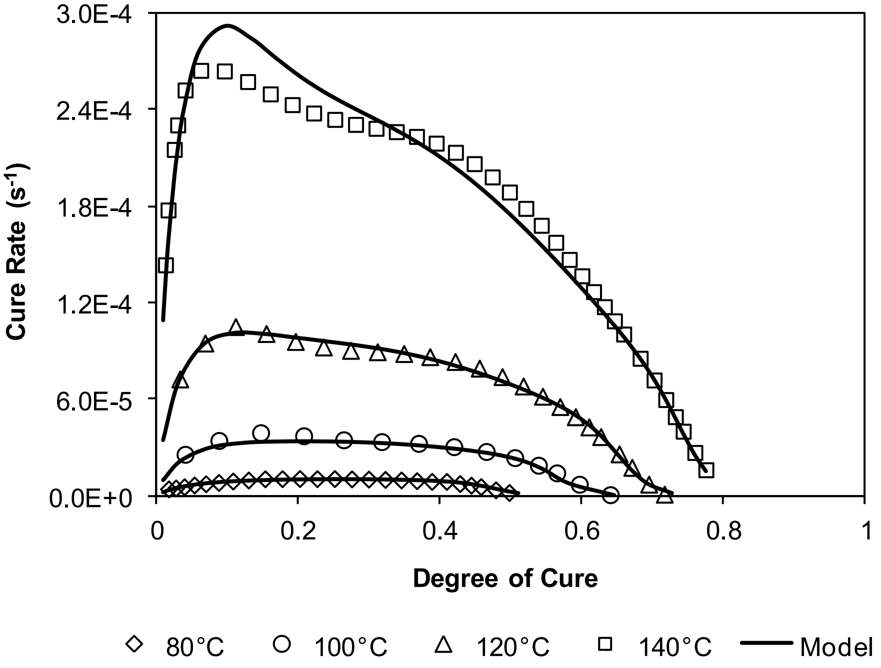

Figure A.2. Measured and predicted cure rate for Cycom 5320 resin.

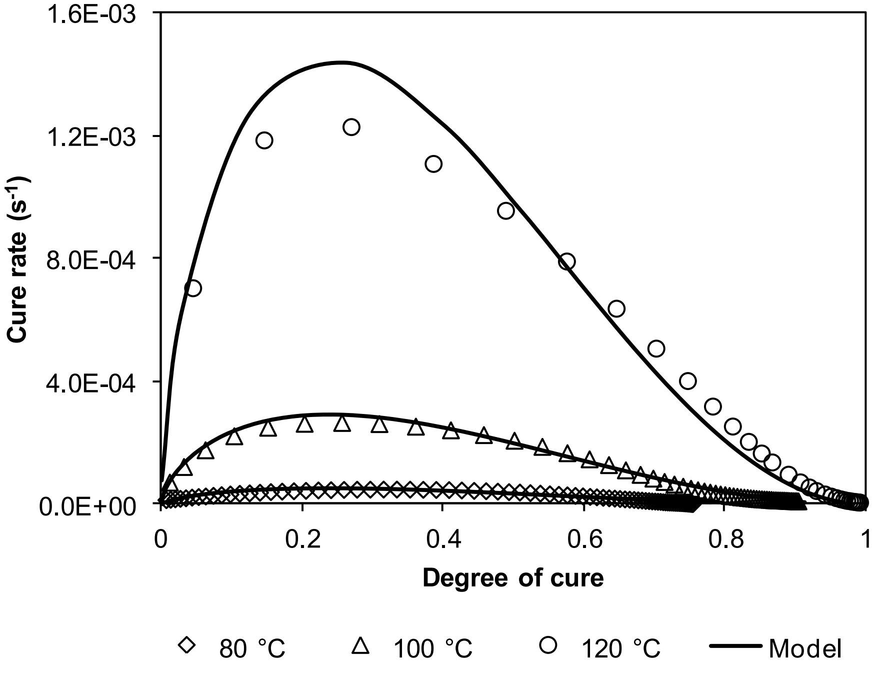

Figure A.3. Measured and predicted cure rate for AF 163-2K adhesive.

Table A.2. Cure kinetics model parameters for Cycom® 5320 and AF 163-2K.

Parameter	Cycom® 5320	AF 163-2K
A_1 (s^{-1})	8.23×10^7	0
E_{A1} (J/mol)	82375	-
m_1	0.75	-
n_1	12.46	-
A_2 (s^{-1})	1.04×10^5	5.3×10^{10}
E_{A2} (J/mol)	6.2×10^4	9.7×10^4
m_2	0.90	0.63
n_2	2.07	2.02
D	40.4	39.95
α_{C0}	-1.12	-0.90
α_{CT} (K^{-1})	4.53×10^{-3}	5.86×10^{-3}
Q_T (J/g)	529.9	185.1

A.3 Rheology

A similar approach to cure kinetics was used to create a semi-empirical model for the rheologial behaviour of the resin and adhesive materials. A viscosity model was created by performing experiments with a rheometer, and fitting a semi-empirical model to the data [97]. An AR 2000 Rheometer by TA Instruments, equipped with an Environmental Test Chamber (ETC), was used to measure the change in complex viscosity in dynamic and isothermal conditions. Each test was repeated twice, and the rheology test matrix is presented alongside the DSC tests in Table A.1. The tests were performed in oscillatory mode by inducing a small amplitude oscillatory strain at 1 Hz into a 0.5 to 1 mm thick sample, mounted between two 25 mm diameter parallel plates. The rheology tests were conducted in the linear viscoelastic region using a controlled strain of 0.25% for Cycom 5320 and 1 % strain for AF 163–2K.

A model to describe the resin viscosities was created according to the techniques presented by *Khoun et al.* [94]. They modified a viscosity model incorporating gel effects, originally developed by *Castro and Macosko* [98]. Their model includes an additional Arrhenius temperature dependency and an additional polynomial term to better describe the viscosity at gelation. The viscosity model is:

$$\eta = \eta_1 + \eta_2 \left(\frac{\alpha_{gel}}{\alpha_{gel} - \alpha} \right)^{A + B\alpha + C\alpha^2} \tag{A.6}$$

where α is the instantaneous degree-of-cure predicted using Eq. (A.5), α_{gel} is the degree-of-cure at gelation, A, B and C are constants, and η_i is the Arrhenius temperature dependency:

$$\eta_i = A_{\eta i} \exp\left(\frac{E_{\eta i}}{RT} \right) \quad , \quad i = 1, 2 \tag{A.7}$$

where $E_{\eta i}$ is the viscosity activation energy, $A_{\eta i}$ is a constant, R is the universal gas constant, and T is the absolute temperature. $E_{\eta 1}$ was taken as the slope of the linear line of best fit through a plot of $ln(\eta)$ versus $1/T$, from room temperature until the viscosity began increasing. The degree-of-cure at gelation, was determined by averaging the degree-of-cure when $tan(\delta) = 1$ in each of the dynamic and isothermal tests. All other constants were calculated using a weighted least squares curve fit with the experimental data. The model constants are summarized in Table A.3.

Table A.3. Viscosity model parameters for Cycom® 5320 and AF 163-2K.

Constant	Cycom 5320	AF 163-2K
$A_{\eta 1}$ (Pa·s)	8.0×10^{-13}	0
$E_{\eta 1}$ (J/mol)	93931	-
$A_{\eta 2}$ (Pa·s)	2.9×10^{-11}	1.0×10^{-8}
$E_{\eta 2}$ (J/mol)	8.3×10^{4}	7.4×10^{4}
α_{gel}	0.48	0.64
A	3.2	2.5
B	12.7	-0.5
C	-29.6	0

The measured dynamic viscosity and the model prediction for Cycom 5320 are shown in see Figure A.4. There is good agreement between the model and experiments until 130 °C, where the model had difficulty capturing the minimum viscosity and gel of temperature ramps greater than 3 °C/min. An improvement in fit was possible, but at the expense of the isothermal viscosity fit. The agreement between the model and isothermal experiments for Cycom 5320 is shown in Figure A.5. The model successfully captures the increase in viscosity over the wide processing temperature range of the material. Since OOA materials are intended for an initial cure below 130 °C, the model will capture the change in viscosity during the ramp and constant temperature hold of the cure cycle. The 5320 gel time is slightly overestimated for the lower temperature isotherms, and underestimated at the highest. If the materials are initially cured between 80 and 130 °C, the viscosity model provides an accurate description of the evolution of the viscosity from room temperature up to gelation.

The dynamic viscosity behaviour of the AF 163–2K adhesive film is shown in Figure A.6. The model captures the measured viscosity profile quite well up to gelation. A similar agreement is observed in the isothermal measurements and predictions in Figure A.7. The viscosity of AF 163–2K is much higher than the Cycom 5320 resin. Adhesives typically have higher viscosities than resins, however the knit carrier film inserted to improve handling during lay-up operations increased the measured AF 163–2K viscosity. As a result, these measurements provide insight into the timing of adhesive minimum viscosity and gelation during processing, but not the flow behaviour. The flow behaviour of the adhesive was not crucial in this work because modelling fillet formation during cure was not considered. If adhesive flow modelling were considered in the future, these experiments and models should be repeated with unsupported adhesive film.

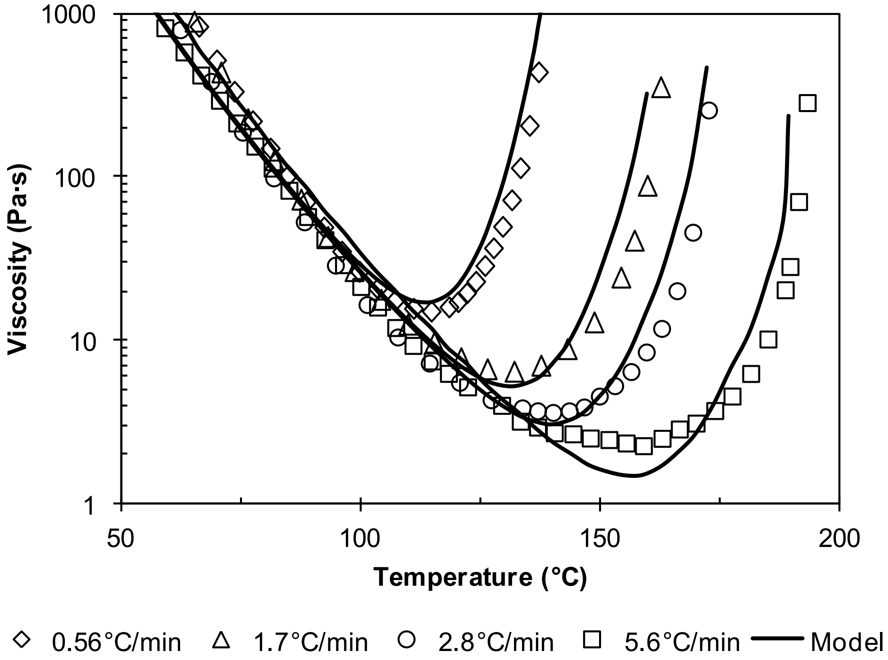

Figure A.4. Measured and predicted dynamic viscosity for Cycom 5320 resin.

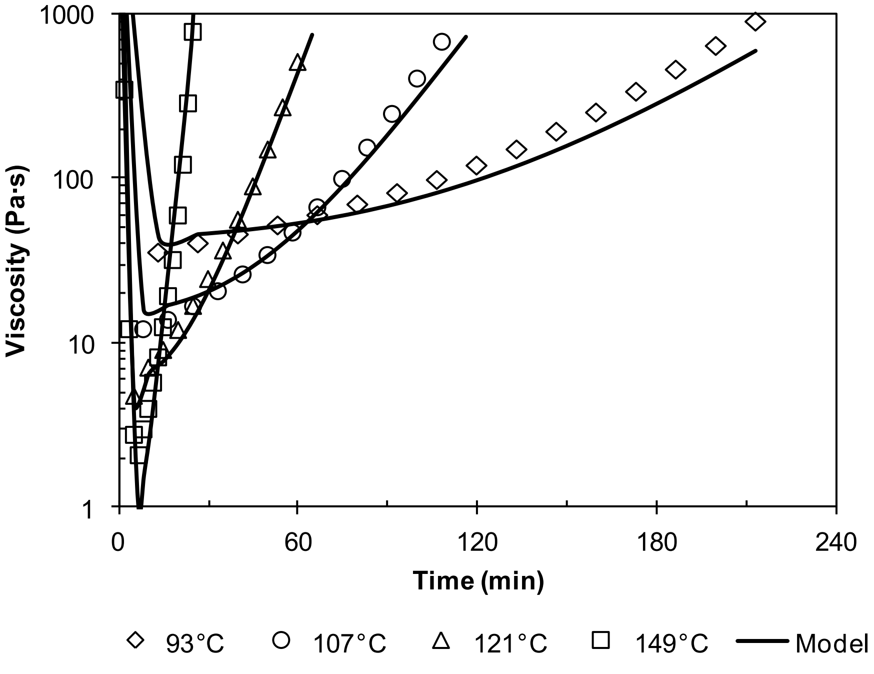

Figure A.5. Measured and predicted isothermal viscosity for Cycom 5320 resin.

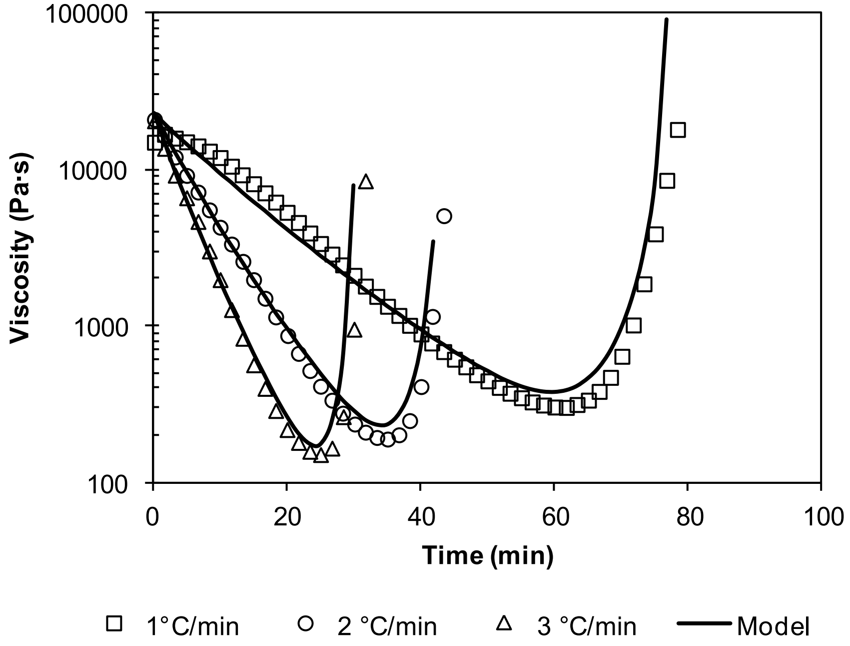

Figure A.6. Measured and predicted dynamic viscosity for AF 163–2K adhesive.

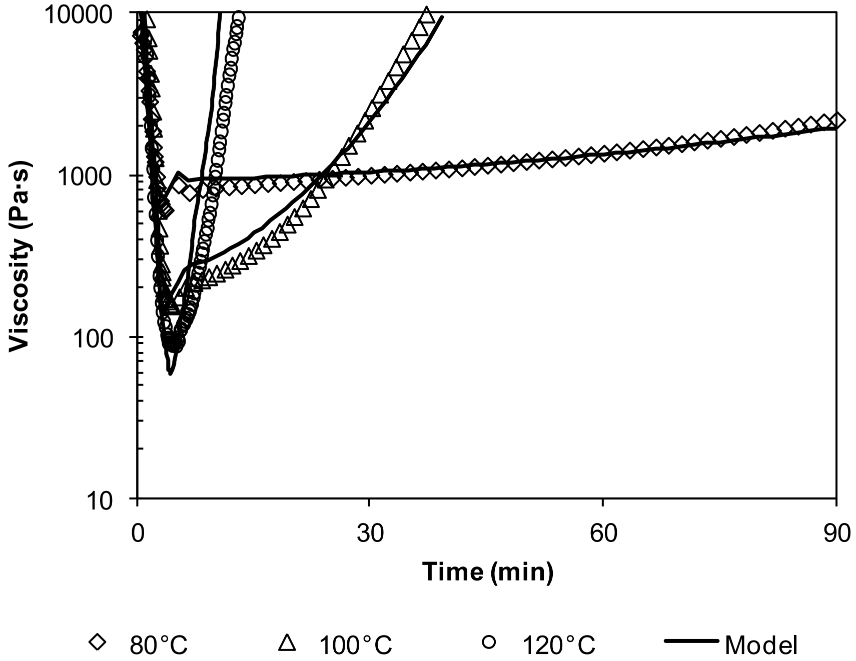

Figure A.7. Measured and predicted isothermal viscosity for AF 163–2K adhesive.

A.3.1 Comparison with manufacturer's viscosity data

To validate the experimental data presented in this study, the measured data was compared with available thermal data from the manufacturers. The only published data available was two viscosity temperature ramps for Cycom® 5320 [58]. The available manufacturers' viscosity data is plotted with the experimentally measured viscosity in Figure A.8. The evolution of the measured viscosity follows the manufacturers' data quite well up to 100 °C. Above 100°C, the measured viscosity is between 3 to 5 Pa·s higher, and gelation occurs between 4 to 5 °C before the manufacturers' viscosity profiles.

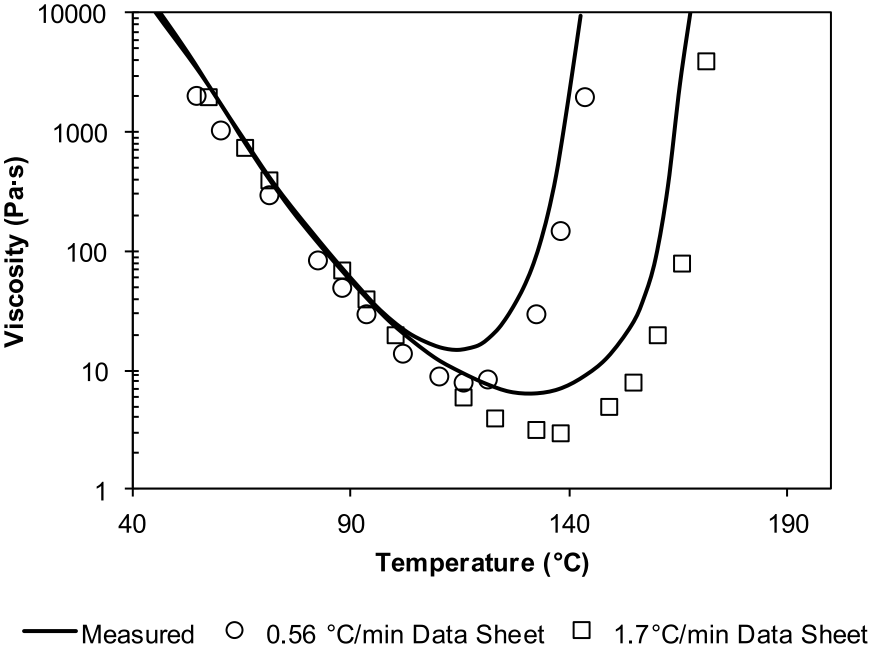

Figure A.8. Measured viscosity and manufacturer's viscosity (extracted from Ref. [58]).

Some of the deviation may be associated with inaccuracies extracting the manufacturers' viscosity values from the data sheet [58], but the most likely cause of the discrepancy is the variation in material out-time between the material tested by the manufacturer, and the material tested in this study. The materials were tested before their expiration date, but they do have a thermal history – manufacturing, transportation, freeze-thaw cycles, and room temperature handling. Given that these resins would likely encounter similar thermal histories in a composites production environment, the viscosity behaviour of the resins is similar to the profiles reported by the manufacture, within the shelf-life of the materials.

A.4 Summary

Together, cure kinetics and viscosity are an important first step towards defining a suitable cure cycle for out-of-autoclave prepreg processing. To aid in this, models describing theses properties were developed for Cycom® 5320 out-of-autoclave prepreg resin and AF 163–2K structural adhesive film. Existing models developed for thermoset resins were fit to dynamic and isothermal differential scanning calorimetric (DSC) and rheological measurements. The low temperature curing capabilities of the out-of-autoclave resin required an additional cure rate term to accurately model the cure reaction over the wide processing range.

References

1. Campbell FC. Manufacturing technology for aerospace structural materials. New York: Elsevier; 2006.
2. Thorfinnson B, Biermann TF. Production of Void Free Composite Parts Without Debulking. 31st International SAMPE Symposium and Exhibition. Las Vegas, NV, 1986. p. 480-90.
3. Thorfinnson B, Biermann TF. Degree of Impregnation of Prepregs - Effects on Porosity. 32nd International SAMPE Symposium and Exhibition. Anaheim, CA, 1987. p. 1500-9.
4. Ridgard C. Advances in low temperature curing prepregs for aerospace structures. 45th International SAMPE Symposium and Exhibition. Long Beach, CA, 2000. p. 1353-67.
5. Repecka L, Boyd J. Vacuum-bag-only-curable prepregs that produce void-free parts. 47th International SAMPE Symposium and Exhibition. Long Beach, CA, 2002. p. 1862-74.
6. Ridgard C. Out of autoclave composite technology for aerospace, defense and space structures. SAMPE '09 Spring Symposium Conference Proceedings. Baltimore, MD, 2009.
7. Grunenfelder LK, Nutt SR. Void formation in composite prepregs - Effect of dissolved moisture. Composites Science and Technology. 2010;70(16):2304-9.
8. Chiou P-L, Oldroyd PK. Out of autoclave material and process for sandwich structures. 52nd International SAMPE Symposium. Long Beach, CA, 2008.
9. Ridgard C. Out of autoclave processed lightweight composite structures for aerospace vehicles. SAMPE 2010 Conference and Exhibition. Seattle, WA, 2010.
10. Bernetich KR. Evaluation of detail part fabrication using out-of-autoclave prepreg. SAMPE 2010 Conference and Exhibition. Seattle, WA, 2010.
11. Armstrong KB, Bevan LG, Cole WF. Care and Repair of Advanced Composites. 2 ed. Warrendale, PA: Society of Automotive Engineers; 2005.

12. Kratz J, Hubert P. Processing out-of-autoclave honeycomb structures: Internal core pressure measurements. Composites Part A: Applied Science and Manufacturing. 2011;42(8):1060-5.
13. Tavares SS, Caillet-Bois N, Michaud V, Manson JAE. Vacuum-bag processing of sandwich structures: Role of honeycomb pressure level on skin-core adhesion and skin quality. Composites Science and Technology. 2010;70(5):797-803.
14. Fragoulis M, Tolan FC, Pearce PJ, Morris CEM. Moisture Uptake by Some Uncured Adhesive Films. The Journal of Adhesion. 1987;20(4):275 – 82.
15. Tavares SS, Caillet-Bois N, Michaud V, Manson JAE. Non-autoclave processing of honeycomb sandwich structures: Skin through thickness air permeability during cure. Composites Part A: Applied Science and Manufacturing. 2010;41(5):646-52.
16. Loos AC, Tuncol G, Long K, Cano RJ, Jensen BJ, Weiser ES. Flow visualization and modeling of the resin infusion process during manufacture of fibre metal laminates by VARTM. 17th International Conference on Composite Materials. Edinburgh, UK, 2009.
17. E.I. du Pont de Nemours and Company. Moisture effects and processing information for Nomex paper. Technical bulletin H-52744; 2002.
18. Bond GG, Hahn GL, Jost KM, Storage T. Prepreg non-autoclave manufacturing technology: program overview and co-cure enablers for disruptive, pervasive use. SAMPE Journal. 2012;48(5):8-15.
19. Tavares SS, Michaud V, Månson JAE. Through thickness air permeability of prepregs during cure. Composites Part A: Applied Science and Manufacturing. 2009;40(10):1587-96.
20. Tavares SS, Michaud V, Månson JAE. Assessment of semi-impregnated fabrics in honeycomb sandwich structures. Composites Part A: Applied Science and Manufacturing. 2010;41(1):8-15.
21. Sequeira Tavares S, Roulin Y, Michaud V, Månson JAE. Hybrid processing of thick skins for honeycomb sandwich structures. Composites Science and Technology. 2011;71(2):183-9.

22. Bear J. Dynamics of fluids in porous media. New York: American Elsevier Pub. Co.; 1972.
23. Dullien FAL. Porous media : fluid transport and pore structure. New York: Academic Press; 1979.
24. Sharma S, Siginer DA. Permeability measurement methods in porous media of fibre reinforced composites. Applied Mechanics Reviews. 2010;63(2):1-19.
25. Advani SG, Sozer EM. Process modeling in composites manufacturing. Boca Raton, FL: CRC Press; 2011.
26. Luo Y, Verpoest I, Hoes K, Vanheule M, Sol H, Cardon A. Permeability measurement of textile reinforcements with several test fluids. Composites - Part A: Applied Science and Manufacturing. 2001;32(10):1497-504.
27. Kuentzer N, Simacek P, Advani SG, Walsh S. Permeability characterization of dual scale fibrous porous media. Composites Part A: Applied Science and Manufacturing. 2006;37(11):2057-68.
28. Wu YS, Pruess K, Persoff P. Gas Flow in Porous Media with Klinkenberg Effects. Transport in Porous Media. 1998;32(1):117-37.
29. Miguel AF, Serrenho A. On the experimental evaluation of permeability in porous media using a gas flow method. Journal of Physics D: Applied Physics. 2007;40(21):6824-8.
30. Scholz S, Gillespie Jr JW, Heider D. Measurement of transverse permeability using gaseous and liquid flow. Composites Part A: Applied Science and Manufacturing. 2007;38(9):2034-40
31. Ding L, Shih C, Liang Z, Zhang C, Wang B. In situ measurement and monitoring of whole-field permeability profile of fibre preform for liquid composite molding processes. Composites Part A: Applied Science and Manufacturing. 2003;34(8):779-89.
32. Um MK, Daniel IM, Childs BW. A gas flow method for determination of in-plane permeability of fibre preforms. Polymer Composites. 2001;22(1):47-56.
33. Pomeroy R, Grove S, Summerscales J, Wang Y, Harper A. Measurement of permeability of continuous filament mat glass–fibre reinforcements by

saturated radial airflow. Composites Part A: Applied Science and Manufacturing. 2007;38(5):1439-43.

34. Feser JP, Prasad AK, Advani SG. Experimental characterization of in-plane permeability of gas diffusion layers. Journal of Power Sources. 2006;162(2 SPEC. ISS.):1226-31.
35. Ahn KJ, Seferis JC, Price JO, Berg AJ. Permeation measurements through prepreg laminates. SAMPE Journal. 1991;27(6):19-26.
36. Nam JD, Seferis JC. Gas permeation and viscoelastic deformation of prepregs in composite manufacturing processes. Polymer Composites. 1995;16(5):370-7.
37. Arafath ARA, Fernlund G, Poursartip A. Gas transport in prepregs: model and permeability experiments. 17th International Conference on Composite Materials. Edinburgh, UK, 2009.
38. Xin C, Li M, Gu Y, Li Y, Zhang Z. Measurement and analysis on in-plane and through-thickness air permeation of fibre/resin prepreg. Journal of Reinforced Plastics and Composites. 2011;30(17):1467-79.
39. Louis BM, Hsiao K, Fernlund G. Gas permeability measurements of out of autoclave prepreg MTM45-1/CF2426A. SAMPE 2010 Conference and Exhibition, Seattle, WA, 2010.
40. Shim SB, Seferis JC. Thermal and air permeation properties of a carbon fibre/toughened epoxy based prepreg system. Journal of Applied Polymer Science. 1997;65(1):5-16.
41. Centea T, Hubert P. Modelling the effect of material properties and process parameters on tow impregnation in out-of-autoclave prepregs. Composites Part A: Applied Science and Manufacturing. 2012;43(9):1505-13.
42. Kratz J, Hsiao K, Fernlund G, Hubert P. Thermal models for MTM45-1 and Cycom 5320 out-of-autoclave prepreg resins. Journal of Composite Materials. 2013;47(3):341-52.
43. Centea T, Hubert P. Measuring the impregnation of an out-of-autoclave prepreg by micro-CT. Composites Science and Technology. 2011;71(5):593-9.

44. Bickerton S, Sozer EM, Graham PJ, Advani SG. Fabric structure and mold curvature effects on preform permeability and mold filling in the RTM process. Part I. Experiments. Composites Part A: Applied Science and Manufacturing. 2000;31(5):423-38.
45. Brace WF, Walsh JB, Frangos WT. Permeability of granite under high pressure. Journal of Geophysical Research. 1968;73(6):2225-36.
46. Odeh A, McMillen J. Pulse testing: Mathematical analysis and experimental verification. Old SPE Journal. 1972;12(5):403-9.
47. Bourbie T, Walls J. Pulse decay permeability: Analytical solution and experimental test. Old SPE Journal. 1982;22(5):719-21.
48. Freeman D, Bush D. Low-permeability laboratory measurements by nonsteady-state and conventional methods. Old SPE Journal. 1983;23(6):928-36.
49. Chen T, Stagg P. Semilog analysis of the pulse-decay technique of permeability measurement. Old SPE Journal. 1984;24(6):639-42.
50. Jones S. A technique for faster pulse-decay permeability measurements in tight rocks. SPE Formation Evaluation. 1997;12(1):19-26.
51. Haskett SE, Narahara GM, Holditch SA. Method for simultaneous determination of permeability and porosity in low-permeability cores. SPE Formation Evaluation. 1988;3(3):651-8.
52. Li H, Jiao JJ, Luk M. A falling-pressure method for measuring air permeability of asphalt in laboratory. Journal of Hydrology. 2004;286(1-4):69-77.
53. Putnam JW, Seferis JC. Prepreg gas permeation as a function of fibre orientation and aging time. Journal of Advanced Materials. 1995;26(3):35-41.
54. Kardos J, Duduković M, Dave R. Void growth and resin transport during processing of thermosetting — matrix composites. In: Dušek K, editor. Epoxy Resins and Composites IV. Berlin: Springer; 1980. p. 101-23.
55. Wang CH, Tsai CL. Theoretical study for moisture diffusion in a carbon/epoxy composite laminate accompanied by thermal conduction. Journal of Composite Materials. 2010;44(18):2233-43.

56. VanLandingham MR, Eduljee RF, Gillespie Jr JW. Moisture Diffusion in Epoxy Systems. Journal of Applied Polymer Science. 1999;71(5):787-98.
57. Wood JR, Bader MG. Modelling the behaviour of gas bubbles in an epoxy resin: Evaluating the input parameters for a diffusion model using a free-volume approach. Journal of Materials Science. 1995;30(4):916-22.
58. Cytec Engineered Materials. CYCOM 5320 Toughened Epoxy for Structural Applications, Out-of-Autoclave Manufacturing. Information Sheet Revision 1.3 – 03.18.09.
59. Zigrang DJ, Bergmann HW. Response of graphite/epoxy sandwich panels to moisture and temperature transients. Journal of Spacecraft and Rockets. 1980;17:219-25.
60. Garrett RA, Bohlmann RE, Derby EA. Analysis and test of graphite/epoxy sandwich panels subjected to internal pressures resulting from absorbed moisture. In: Vinson JR, editor. Advanced Composite Materials - Environmental Effects. Philadelphia, Pa: American Society for Testing Materials; 1978. p. 234-53.
61. Choi HS, Jang YH. Bondline strength evaluation of cocure/precured honeycomb sandwich structures under aircraft hygro and repair environments. Composites Part A: Applied Science and Manufacturing. 2010;41(9):1138-47.
62. Hayes BS, Seferis JC, Edwards RR. Self-adhesive honeycomb prepreg systems for secondary structural applications. Polymer Composites. 1998;19(1):55-64.
63. Cauberghs J, Hubert P. Effect of tight corners and ply terminations on quality in out-of-autoclave parts. Paper presented at the 2011 SAMPE Spring Technical Conference and Exhibition. Long Beach, CA; 2011.
64. Brillant M, Hubert P. Out-of-autoclave processing of complex shape laminates. Paper presented at SAMPE 2010 Conference and Exhibition. Seattle, WA; 2010.
65. Alteneder AW, Renn DJ, Seferis JC, Curran RN. Processing and Characterization Studies of Honeycomb Composite Structures. Paper

presented at the Proceedings of the 38th International SAMPE Symposium and Exhibition, Anaheim, CA, USA, 1993.

66. Okada R, Kortschot MT. The role of the resin fillet in the delamination of honeycomb sandwich structures. Composites Science and Technology. 2002;62(14):1811-9.
67. Butukuri RR, Bheemreddy VP, Chandrashekhara K, Berkel TR, Rupel K. Evaluation of skin-core adhesion bond of out-of-autoclave honeycomb sandwich structures. Journal of Reinforced Plastics and Composites. 2012;31(5):331-9.
68. Khan S, Loken HY. Bonding of sandwich structures the facesheet/honeycomb interface a phenomenological study. Paper presented at the SAMPE 2007 Conference and Exhibition. Baltimore, MD; 2007.
69. Centea T, Hughes S-M, Payette S, Kratz J, Hubert P. Scaling Challenges Encountered with Out-of-Autoclave Prepregs. Paper presented at the 53rd AIAA/ASME/ASCE/AHS/ASC Structures, Structural Dynamics and Materials Conference. Honolulu, HI: American Institute of Aeronautics and Astronautics; 2012.
70. Olivier P, Cottu JP, Ferret B. Effects of cure cycle pressure and voids on some mechanical properties of carbon/epoxy laminates. Composites. 1995;26(7):509-15.
71. Grove SM, Popham E, Miles ME. An investigation of the skin/core bond in honeycomb sandwich structures using statistical experimentation techniques. Composites Part A: Applied Science and Manufacturing. 2006;37(5):804-12.
72. Brayden TH, Darrow DC. Systems approach for improvement of the manufacturing process for composite honeycomb sandwich panels. 28th International SAMPE Technical Conference. Seattle, WA1996. p. 1300-8.
73. Jouin P, Pollock D, Rudisill E. Effects of processing variables on the quality of co-cured sandwich panels. In: Composite Materials: Testing and Design, Grimes GC, editor. San Francisco, CA: American Society of Testing and Materials; 1992. p. 283-307.

74. Renn DJ, Tulleau T, Seferis JC, Curran RN, Ahn KJ. Composite honeycomb core crush in relation to internal pressure measurement. Journal of Advanced Materials. 1995;27(1):31-40.
75. Zahlan N, Emmerson GT. Using optical sensors to understand core crush in composite panels during processing. In: SPIE Proceedings of the 3rd International Conference on Intelligent Materials and 3rd European Conference on Smart Structures and Materials; 1996. p. 235-9.
76. Brayden TH, Darrow DC. Effect of cure cycle parameters on 350F cocured epoxy honeycomb core panels. 34th International SAMPE Symposium and Exhibition. Reno, NV; 1989. p. 861-74.
77. Stankunas TP, Mazenko DM, Jensen GA. Cocure investigation of a honeycomb reinforced spacecraft structure. 21st International SAMPE Technical Conference. Atlantic City, NJ; 1989. p. 176-88.
78. Bocherens E, Bourasseau S, Dewynter-Marty V, Py S, Dupont M, Ferdinand P, et al. Damage detection in a radome sandwich material with embedded fibre optic sensors. Smart Materials and Structures. 2000;9(3):310-5.
79. Dawood TA, Shenoi RA, Sahin M. A procedure to embed fibre Bragg grating strain sensors into GFRP sandwich structures. Composites Part A: Applied Science and Manufacturing. 2007;38(1):217-26.
80. Minakuchi S, Okabe Y, Takeda N. Real-time detection of debonding between honeycomb core and facesheet using a small-diameter FBG sensor embedded in adhesive layer. Journal of Sandwich Structures and Materials. 2007;9(1):9-33.
81. Lane M, Poursartip A, Fernlund G, Willden K, Nelson K. Robust Processing of Composite Structures. Paper presented at the SAMPE 2010 Conference and Exhibition Seattle, WA, 2010.
82. Kadoya K, Matsunaga N, Nagashima A. Viscosity and Thermal Conductivity of Dry Air in the Gaseous Phase. J Phys Chem Ref Data. 1985;14(4):947-70.
83. ANSYS FLUENT User's Guide, Release 13.0, November 2010.

84. Hsiao K, Fernlund G. In-plane and through-thickness permeability of Cycom 5320 plain weave prepreg. Internal project report. The University of British Columbia, Vancouver, Canada. October 26th, 2010.
85. Advani SG, Sozer EM. Process modeling in composites manufacturing. Boca Raton, FL: CRC Press; 2011.
86. Wilke CR. A Viscosity Equation for Gas Mixtures. The Journal of Chemical Physics. 1950;18(4):517-9.
87. Recktenwald G. Numerical methods with Matlab. Upper Saddle River, NJ: Prentice Hall; 2000.
88. Shen C-H, Springer GS. Moisture Absorption and Desorption of Composite Materials. Journal of Composite Materials. 1976;10(1):2-20.
89. Tuttle ME. Moisture diffusion in honeycomb core sandwich composites. 17th International Conference on Composite Materials. Edinburgh, UK; 2009.
90. Fick A. V. On liquid diffusion. Philosophical Magazine Series 4. 1855;10(63):30-9.
91. ASTM Standard C297, 04 (2010), "Standard Test Method for Flatwise Tensile Strength of Sandwich Constructions," ASTM International, West Conshohocken, PA, 2012, DOI: 10.1520/C0297_C0297M-04R10, www.astm.org.
92. Yenilmez B, Senan M, Murat Sozer E. Variation of part thickness and compaction pressure in vacuum infusion process. Composites Science and Technology. 2009;69(11–12):1710-9.
93. Yousefi A, Lafleur PG, Gauvin R. Kinetic studies of thermoset cure reactions: A review. Polymer Composites. 1997;18(2):157-68.
94. Khoun L, Centea T, Hubert P. Characterization methodology of thermoset resins for the processing of composite materials - Case study. Journal of Composite Materials. 2010;44:1397-415.
95. Kamal MR, Sourour S. Kinetics and thermal characterization of thermoset cure. Polymer Engineering & Science. 1973;13(1):59-64.
96. Cole KC, Hechler JJ, Noel D. A new approach to modeling the cure kinetics of epoxy/amine thermosetting resins. 2. Application to a typical system based

on bis[4-(diglycidylamino)phenyl]methane and bis(4-aminophenyl) sulfone. Macromolecules. 1991;24(11):3098-110.

97. Halley PJ, Mackay ME. Chemorheology of thermosets - an overview. Polymer Engineering & Science. 1996;36(5):593-609.
98. Castro JM, Macosko CW. Kinetics and rheology of typical polyurethane reaction injection molding systems. Society of Plastics Engineers (Technical Papers). 1980:434-8.